Spectrally Efficient Transmitter Diversity Scheme for Optical Satellite Feeder Links

Von der Fakultät 5 - Informatik, Elektrotechnik und Informationstechnik
der Universität Stuttgart zur Erlangung der Würde eines
Doktor-Ingenieurs (Dr.-Ing.) genehmigte Abhandlung

Vorgelegt von
Ahmad Mustafa
aus Abu Dhabi, V.A.E

Hauptberichter:	Prof. Dr.-Ing. Stephan ten Brink
Mitberichter:	Prof. Dr.-Ing. Andreas Kirstädter
Tag der mündlichen Prüfung:	20.03.2024

Institut für Nachrichtenübertragung der Universität Stuttgart
2024

Acknowledgements

The work presented in thesis was carried out at the Optical Communications Group of the Institute of Communications & Navigation at the German Aerospace Center (DLR) in Oberpfaffenhofen. I am indebted to the institute for providing access to the labs equipped with state-of-the-art hardware that was used to perform all the experiments presented in this thesis.

In particular, I am grateful to my PhD supervisor at DLR, Dr. Dirk Giggenbach whose continuous support and guidance helped me in making progress in my thesis work. He was always available for the fruitful discussions and regular meetings that were instrumental in achieving the desired results. He actively supported me in publishing my work and presenting it in the conferences that I enjoyed alot as part of gaining experience and expanding my professional network. After I left DLR in 2019, he kept supporting me in my thesis writing.

I am also thankful to Dr. Juraj Poliak from DLR whose valuable comments contributed to the publications that were the outcome of my research work.

My special gratitude goes to my doctor father, Prof. Stephan ten Brink from the Institute of Telecommunications at the University of Stuttgart. He played a key role in getting me admitted to the PhD program at the university. His valuable feedback and comments throughout thesis writing phase and defense made it possible to finish the PhD in “style”.

Finally, I extend my gratitude to the DLR-DAAD Doctoral Fellowship that supported me financially during my time at DLR.

Kurzfassung

Es besteht ein ständig wachsender Bedarf an einer Erhöhung des Datenverkehrs im Bereich von Tb/s geostationären (GEO) Satelliten. Dies wird dazu beitragen, zahlreiche Benutzer am Boden zu vernetzen, die keinen Zugang zum Internet haben. Dieser hohe Datendurchsatz kann durch die Verwendung von mehreren Laserstrahlen im Uplink und deren Kombination mit der dichten Wellenlängenmultiplex-Technik erreicht werden. Allerdings leiden optische Signale, die sich durch die turbulente Atmosphäre zu GEO-Satelliten ausbreiten, unter Intensitäts- und Phasenschwankungen. Zusätzlich führt die durch die Atmosphäre bedingte Strahlwanderung zu Ausrichtungsfehlern am Satelliten, was zu starken Schwächungen und damit zu Verlusten von Signalstärke führt, welche wiederum unter den Empfängerschwellenwert fallen kann und die Kommunikation unmöglich macht. Das Problem des Photonenmangels kann durch den Einsatz fortschrittlicher energieeffizienter, kohärenter Modulationsformate angegangen werden, die sehr empfindlich sind, aber mit einer erhöhten Systemkomplexität einhergehen. Daher wird in dieser Arbeit nur ein Intensitätsmodulations- und das direkte Detektions-Schema namens „Non-Return-to-Zero On-Off-Keying“ berücksichtigt, das im optischen Richtfunk einfacher zu implementieren ist. Um die atmosphärischen Einbrüche abzumildern, wird eine Senderdiversitätstechnik namens multiple-input single-output (MISO) für GEO-Feeder-Links zur zuverlässigen Signalübertragung am Satelliten in Betracht gezogen. Es erfordert mehrere Laserstrahlen, die sich über unkorrelierte Kanäle ausbreiten, was durch eine physische Trennung zwischen den Übertragungsteleskopen, die größer als die atmosphärische Kohärenzlänge ist, erreicht werden kann. Die Arbeit gliedert sich in zwei Hauptteile: Der erste Teil umfasst die quantitative Analyse des MISO-Schemas ohne spektrale Überlappung zwischen den benachbarten Signalen. Hier besteht das Fading aus log-normal Szintillation und Reststrahl-Jitter. Die Bitfehlerrate (BER) für die Single-Input-Single-Output- und MISO-Systeme wird mithilfe der Fading-Statistiken der Atmosphäre und unter Berücksichtigung des Empfängermodells eines handelsüblichen 10Gb/s-Fotoempfängers mit einer Avalanche-Photodiode ermittelt. Für die gegebenen atmosphärischen Bedingungen und Reststrahlrichtungsjitter wird die Sendeleistung jedes Strahls optimiert, um den Gesamtszintillationseffekt zu minimieren und den BER-Gewinn zu maximieren. Der zweite Teil der Arbeit zielt darauf ab, die spektrale Effizienz des Übertragungssystems zu erhöhen, wobei Einseitenbandsignalen mithilfe optischer Filter erzeugt werden, um die gewünschte BER-Leistung zu erreichen. Ein Laborversuch mit einem 32-Gbit/s-System wird in einem Back-to-Back Setup durchgeführt, um die single-sideband (SSB)-Signale mithilfe einer passiven Filtertechnik zu optimieren. Hier werden die Filterbandbreite und die Mittenfrequenz vom Träger optimiert, um eine fehlerfreie Übertragung zu erzielen. Abschließend werden Simulationen durchgeführt, wobei das optimierte obere Seitenband und das untere Seitenband aus den jeweiligen Zweiseitenband-Signalen erhalten und dann über den atmosphärischen Kanal ausgebreitet werden, welches aus Log-Normal-Szintillationseffekten und Phasenkolben besteht. Der Trägerabstand zwischen den beiden Signalen wird so ausgewählt, dass eine konstruktive und destruktive Interferenz aufgrund des langsam veränderlichen Phasenkolbens simuliert wird. Es wird eine Diversitäts-Gewinn von 2,3 dB erreicht, was die Wirksamkeit der Nutzung der Senderdiversität in einem GEO-Uplink-Kanal zeigt.

Abstract

There is an ever-growing demand for increasing the data traffic in the order of Tb/s to the geostationary (GEO) satellites. It will help connect numerous users on the ground who do not have access to internet service. This high throughput can be achieved using multiple laser beams in the uplink and combining them with the dense wavelength division multiplexing technique. However, optical signals propagating through the turbulent atmosphere to GEO satellites suffer from the intensity and phase fluctuations. Additionally, atmospherically induced beam wander leads to pointing errors at the satellite resulting in deep fades, hence loss of signal power which can fall below the receiver sensitivity making the communication impossible. The problem of photon scarcity can be tackled by using advanced power-efficient coherent modulation formats which are highly sensitive, but they come at the expense of increased system complexity. Therefore, in this thesis, only an intensity modulation and direct detection scheme called non-return-to-zero on-off keying is considered, which is relatively easier to implement in free-space optical communications. To mitigate the atmospheric fades, a transmitter diversity technique called MISO is considered for GEO feeder links for reliable signal reception at the satellite. It requires multiple laser beams to propagate through uncorrelated channels, which can be achieved by having a physical separation between the transmitting telescopes greater than the atmospheric coherence length. This thesis is divided into two main parts: The first part includes the quantitative analysis of the MISO scheme with no spectral overlapping between the neighboring signals. Here, the fading consists of log-normal scintillation and residual beam pointing jitter. The bit error rate (BER) for the single-input single-output and MISO systems is obtained using the fading statistics of the atmosphere and considering the receiver model of a commercially available 10Gb/s photoreceiver with an avalanche photodiode. For the given atmospheric conditions and residual beam pointing jitter, the transmit power of each beam is optimized to minimize the overall power scintillation index and maximize the BER gain. The second part of the thesis aims at increasing the spectral efficiency of the transmission system where SSB signals are generated using optical filters to achieve the desired BER performance. A laboratory experiment with a 32Gb/s system is performed in a back-to-backup setup to optimize the SSB signals using a passive filtering technique. Here, the filter bandwidth and the center frequency from the carrier are optimized to get the error-free performance. Finally, simulations are performed where the optimized upper sideband and lower sideband from the respective double-sideband signals are obtained, and then they are propagated through the atmospheric channel, which consists of log-normal scintillation effects and phase piston. The carrier separation between the two signals is selected such to emulate constructive and destructive interference due to the slowly varying phase piston. A diversity gain of 2.3 dB is achieved, which shows the efficacy of using transmitter diversity in a GEO uplink channel.

Contents

Acronyms

ADC	analog-to-digital converter
APD	avalanche photodiode
ARTEMIS	advanced relay technology mission satellite
ASK	amplitude-shift keying
AWGN	additive white Gaussian noise
BER	bit error rate
BPG	bits pattern generator
CW	continuous wave
DFB	distributed feedback
DFT	discrete fourier transform
DSP	digital signal processing
DWDM	dense wavelength division multiplexing
EDFA	erbium-doped fiber amplifier
ESA	eurpopean space agency
FEC	forward error correction
FSO	Free-space optical
FTB	fading testbed
GEO	geostationary
IM/DD	intensity modulation and direct detection
IPA	isoplanatic anglel
IRT	index of refraction turbulence
LCoS	liquid crystal on silicon
LCT	laser communications terminal
LEO	low earth orbit
LFE	linear feedforward equalizer
LFSR	linear feedback shift register
LMS	least mean square

LSB lower sideband
MISO multiple-input single-output
MZM Mach-Zehnder modulator
MZI Mach-Zehnder interferometer
MUX multiplexer
NEP noise equivalent power
NICT national institute of information and communications technology
NRZ non-return-to-zero
NRZ-OOK non-return-to-zero on-off keying
OA optical axis
OGEOFL optical geostationary feeder links
OGS optical ground station
OICETS optical inter-orbit communication engineering test satellite
OOK on-off keying
OSA optical sub-assembly
OSNR optical signal-to-noise ratio
OSSB optical single sideband
PAA point ahead angle
PDF probability density function
PDF probability density function
PRBS pseudo-random binary sequence
PDF probability density function
PSI power scintillation index
RF radio frequency
RFE receiver front-end
SCPI standard commands for programmable instruments
SE spectral efficiency
SILEX semiconductor inter-satellite experiment
SISO single-input single-output
SISO single input single output
SMF single-mode fiber
SNR signal-to-noise ratio
SE spectral efficiency

SSB single-sideband
TIA transimpedance amplifier
TEM transverse electromagnetic
USB upper sideband
VSB vestigial sideband
WA wave analyzer

Nomenclature

α_{e}	Total extinction coefficient per unit length
α_{rain}	Specific attenuation due to rain
α_{snow}	Specific attenuation due to snow
ε	Elevation angle between the ground station and the satellite
ε	Elevation angle
η	Quantum efficiency
η_{F}	Bandwidth efficiency
κ	Scalar spatial frequency
κ_0	Spatial frequency corresponding to the outer scale
κ_m	Spatial frequency corresponding to the inner scale
λ	Wavelength of light
$\langle r_c^2 \rangle$	Beam wander variance
$\mathrm{erfc}(x)$	Complementary error function
$\mathrm{erf}(.)$	Error function
ω_0	$1/e^2$ beam divergence half angle
ω_{sr}	Slew rate of a satellite
ρ	Separation distance between two points of the index of refraction
σ_0^2	Variance of received zeros
σ_{I}^2	Variance of received ones
σ_{Bu}^2	Rytov index
σ_{b}^2	Background noise
σ_{D}^2	Dark current

σ_{I}^2 Scintillation index

σ_{s}^2 Shot noise

σ_{T}^2 Thermal noise

θ_0 Isoplanatic angle

θ_{BW} Angular beam wander displacement

θ_{PAA} Point-ahead angle

$\Phi_n(\kappa)$ Power spectrum of the refractive index

ζ Zenith angle

B_{e} Bandwidth over which the noise is measured

B_{F} Bandwidth required for a single feeder link

B_{ref} Reference bandwidth

c Speed of light

C_{Sat} Capacity of the user link

c_k Taps

C_n^2 Refractive index structure parameter

D Diameter of the aperture

$D_n(\rho)$ Structure function of the refractive index fluctuations

E Electrical field of the optical wave

f Modulus of the spatial frequency vector

F_0 Radius of curvature

F_{A} Excess noise factor

F_c Net centripetal force

F_g Gravitational force

G Gravitational constant

$g_R(t)$ Impulse response of the lowpass filter

h Planck's constant

H_{sat} Altitude of the satellite from the ground

H_{T} Height of tropopause

H_{OGS} Altitude of the optical ground station

I_{L} Intensity received at a distance L

I_{s} DC current produced during photodetection process

k Wavenumber

k_{B} Boltzmann's constant

k_{c} Carrier ionization ratio

L Distance from ground to the satellite

L Number of symbols

L_0 Outer scale of turbulence

l_0 Inner scale of turbulence

L_{j} Power penalty due to pointing errors

L_{sci} Scintillation loss

L_{T} thickness of tropopause layer

l_f Characteristic size of the fluid

M Multiplication factor

M_{sat} Mass of the satellite

M_e Mass of the earth

N Number of samples per symbol

$n(r,t)$ Index of refraction

n_0 Average value of the index of refraction

$n_1(r,t)$ Random index of refraction value from the mean

N_{GW} Number of gateways

N_{p} Number of photons per bit

n_{sp} Inversion factor of the amplifier

n_s	Number of bits in a symbol
N_s	Number of taps
p	Coefficient dependent on the size distribution of the scattering particles
$p(0\mathrm{r})$	Probability of received zeros
$p(1\mathrm{r})$	Probability of received ones
$P(r)$	Atmospheric pressure
p_thr	Fraction of signal loss duration
Q	Quality factor
q	Elementary charge of an electron
R	Responsivity
R_f	Rain fall rate in mm/h
R_L	Resistor value of the photoreceiver's circuit
R_o	Orbit of the satellite
R_e	Radius of the earth
R_n	Reynold number
S	Snow fall rate in mm/h
T	Transmittance
$T(r)$	Atmospheric temperature
T_LS	Contribution in long-term spot size due to large scales
T_SS	Contribution in long-term spot size due to small scales
T_e	Effective noise temperature
V	Visibility
v	rms wind speed in m/s
$V(h)$	Wind velocity according to the Bufton model
V_0	Mean value of received zeros
V_1	Mean value of received ones

V_{sat} Satellite velocity

V_{t} Threshold to detect ones and zeros

v_{T} Wind velocity at tropopause

V_{π} Bias voltage

V_{c} Characteristic velocity of the flow

v_{g} Ground wind velocity

v_{k} Kinematic viscosity of the fluid

W_{0} Beam radius at the transmitter plane

W_{SS} Short-term beam spread

W_{LT} Long-term spot size

List of Figures

List of Tables

1. Introduction

1.1. Overview

Free-space optical (FSO) communications is an attractive alternative to microwave technology in GEO satellite communications feeder link applications due to the possibility of transmitting information with high data rate due to shorter optical wavelengths, lower requirements on terminal size, weight, and power (SWaP), secure communication, and no need of spectrum licensing as compared to its classical radio frequency (RF) communications counterpart [9, 3, 10, 11, 12, 13]. In addition, there is an increasing demand for data and multimedia services and accessing remote areas on Earth where terrestrial cable networks cannot be established due to rugged terrain or lack of available infrastructure. Satellite communications from GEO satellites can effectively cover such gaps in the internet connectivity since it is not obstructed by any topological issues on the ground [14, 15, 16]. However, the existing communication satellite transmission technology cannot provide the required high throughput (which will quickly go beyond 1Tb/s per satellite) to serve a large number of users which will communicate with the satellite with RF spot beams as shown in Fig. 1.1.

Optical feeder links to the GEO satellite can provide very high throughput by the combination of high modulation bandwidth and dense wavelength division multiplexing (DWDM) technology [17, 1, 18, 19, 20, 21]. Currently deployed RF satellites operate in the Ka-band, which according to Eq. (1.1) require over 70 ground stations to reach Tb/s throughput as shown in Fig. 1.2. The required bandwidth B_{F} for a single feeder link is determined by the number of parallel RF-gateways N_{GW} and bandwidth efficiency η_{F} which is taken as 2.32 $\mathrm{b/s/Hz}$ as given in [1, 22]

$$B_{\mathrm{F}} = \frac{C_{\mathrm{Sat}}}{2N_{\mathrm{GW}} \cdot \eta_{\mathrm{F}}} \tag{1.1}$$

where $\mathrm{C_{Sat}}$ is the user link capacity in $\mathrm{b/s}$. The number of required ground stations can be reduced to just over 40 if the unused spectrum in the Q/V band is used. However, if optical technologies are used in combination with the DWDM scheme, then Tb/s speeds can be reached by just one ground station. This is possible because around a bandwidth of 11THz of the optical spectrum is available in the C- and L-band, which is also supported by the standard erbium-doped fiber amplifier (EDFA) technology that is widely used in optical fiber communications. It is to be noted that FSO communications depend heavily on local weather conditions, e.g., clouds and fog can cause complete link blockage because of high attenuation. As an example, a 1550nm wavelength can experience around 7dB/km of attenuation due to

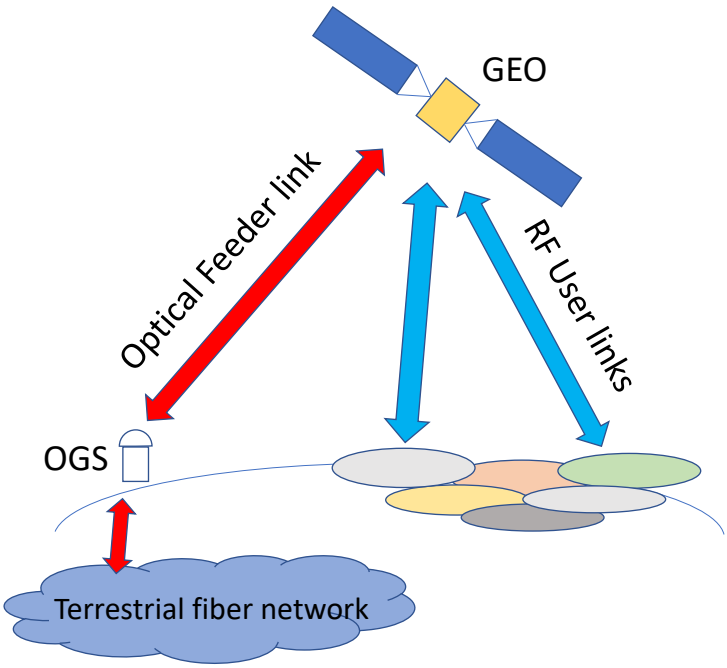

Figure 1.1.: Concept of optical GEO feeder link network [1]

fog at a visibility of 0.5km [23]. Therefore, it is vital to strategically place optical ground stations where the weather is mostly cloud-free. In this way, it is made sure that at least one of the ground stations is available for communications due to clear-sky conditions. This distribution of ground stations is also called site diversity, due to which the German, European and international network can provide an availability of 84.7%, 99.9%, and 100%, respectively [24, 25]. The required number of optical ground station (OGS) to achieve this high availability is only around 10 [26, 27, 28].

1.2. Topic of this thesis

This thesis deals with a spectrally efficient transmitter diversity scheme in combination with DWDM system to achieve Tb/s throughput in a GEO feeder link. The DWDM system is essential in achieving high throughput that is achieved by multiplexing several individual optical carriers into one beam. To meet the link budget requirements, the transmitted optical power is increased by using an EDFA booster. Currently, the technology of optical amplifiers has reached a maturity level to give a stable output power in the order of tens of Watts. A drawback is the low wall-plug efficiency of around 10%, which is the ratio of the optical output power to the input electrical power consumption [29]. Using only C-band (1529nm - 1565nm), 40 channels with 100 GHz grid spacing can be utilized. By modulating each channel with 40Gb/s unique signals, a total throughput of 1.6Tb/s can be achieved. A 40Gb/s signal can be produced by using an electro-optic modulator which is a phase modulator in a

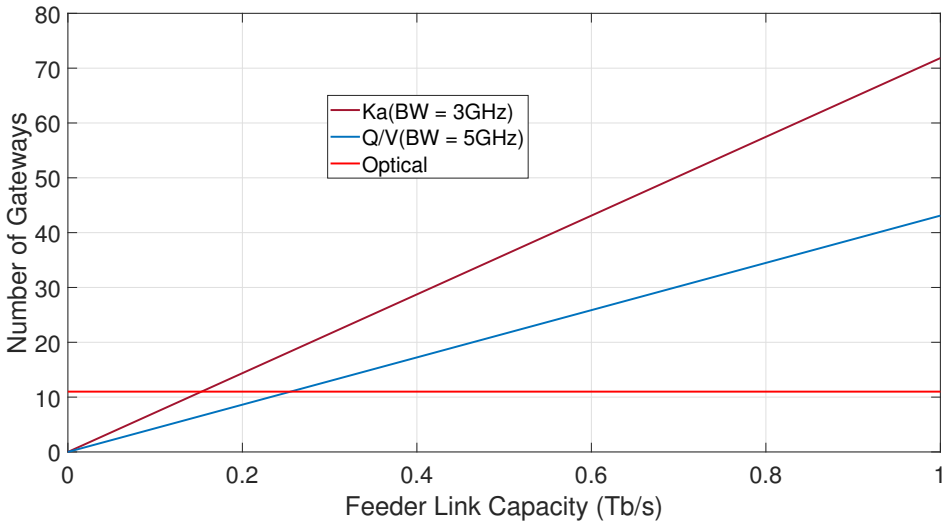

Figure 1.2.: A comparison of the number of required ground stations for the RF and optical feeder links. However, for the optical links, site diversity is required to mitigate cloud blockage [1]

MZI configuration. The phase modulator works on the principle of Pockels effect, which is the change of the refractive index of a non-linear medium, usually $LiNbO_3$, w.r.t the applied voltage. The intensity modulation is achieved by constructive and destructive interference at the output of the MZI.

The individual data-carrying optical carriers are multiplexed using a high power multiplexer (MUX) which combines all the carriers separated by 100 GHz (0.8 nm) channel spacing. The amplified signal after the booster is sent to the transmitter optical sub-assembly (OSA) which consists of lenses, mirrors, guiding optical elements, and a transmitting telescope to transmit the light from the single-mode fiber (SMF) of the booster towards the GEO satellite. To mitigate the atmospherically induced fades as seen by the satellite receiver, copies of the individual data are sent from another OSA which can be at the same site or even integrated into the same OGS since the required physical separation between the two transmitting telescopes can be less than just 1 m. This concept of a diversity order of two is shown in Fig. 1.3a. The diversity order can be increased to mitigate the strength of the fades even further at the cost of requiring much greater spectrum hence decreasing the overall user data rate. Not to mention it requires more hardware on the ground, which increases the system complexity, maintenance, and cost. At the satellite receiver as shown in Fig. 1.3b, the beams sent from the two ground telescopes are received by the receiving OSA which couples the light in the SMF of the EDFA preamplifier which provides sufficient gain to increase the power of the weak received signal to the level which the following photodiodes can detect. Before that, the signal is de-multiplexed into individual optical carriers, which are fed to the respective receiver front-end (RFE)s which consists of a PIN photodiode and a transimpedance amplifier (TIA) to convert the current into voltage for further processing of the data during the demodulation process.

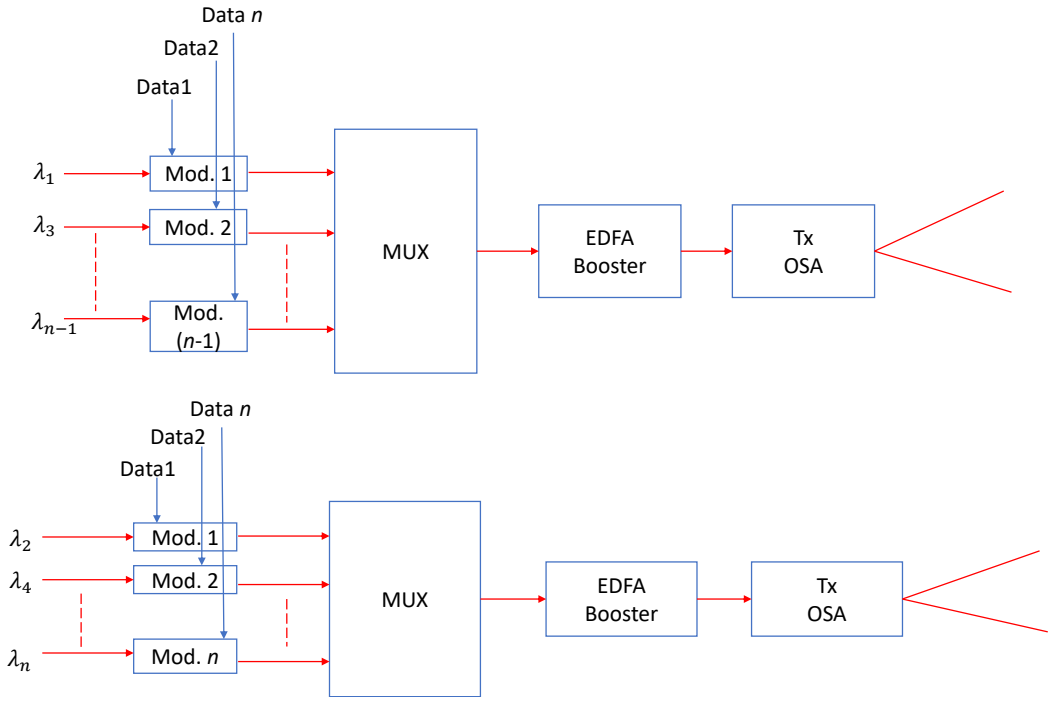

(a) Block diagram of a 2×1 diversity scheme at the ground station deploying n optical carriers per telescope to achieve Tb/s throughput

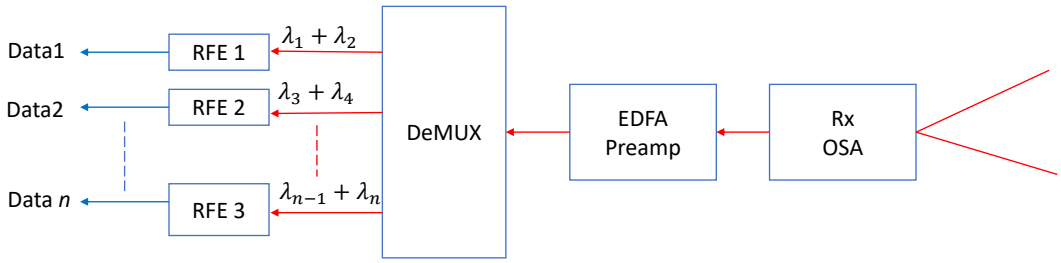

(b) Block diagram of the receiver at the GEO satellite to de-multiplex the n carriers and recover the individual data streams

Figure 1.3.: Transmitter diversity concept using DWDM technology to achieve Tb/s throughput in an OGEOFL scenario

Even in cloud-free locations, optical links through the atmosphere suffer from scintillation and atmospherically induced wandering of the propagating beam giving rise to intensity fluctuations of the received signal at the satellite [30, 31, 3, 32, 33]. To overcome pointing errors that occur due to beam wander, the beam divergence can be increased, so the receiver at the satellite is always illuminated. It relaxes the requirement on the pointing and tracking system accuracy but at the expense of lower mean received power at the satellite, which requires highly sensitive preamplified receiver to close the link. An EDFA based receiver requires SMF coupling, but it is possible in uplink due to the point receiver. To deliver more power to the receiver, a narrow beam can be used, but this puts tighter requirements on the pointing and tracking system. In the uplink, beam wander is a severe issue that increases the misalignment between the transmitter and the receiver giving rise to deep and long fades. For high-speed data transmission in the order of Gb/s per channel, a fade duration of a few milliseconds can lead to the loss of millions of bits. Transmitter diversity technique can be employed beneficially in the optical geostationary feeder links (OGEOFL) as it provides atmospheric fading mitigation, which is required for the reliable signal reception.

This thesis investigates the feasibility of passive optical filtering in generating SSB signals to increase spectral efficiency (SE) of the communication system. The atmospheric effects considered in this thesis include fading due to index of refraction turbulence (IRT) of atmosphere and pointing errors that cause deep and long fades. The turbulent cells in the order of beam size contribute to the scintillation of the beam intensity and have diffractive effects. The eddies larger than the beam size have refractive effects on the beam propagation, which eventually causes the pointing errors meaning the beam occasionally misses the receiver at the satellite. The quantitative analysis includes studying the combined irradiation statistics of the sum of four beams with log-normal and residual pointing jitter effects. The BER curves and diversity gain under such turbulence conditions are numerically obtained using the irradiation statistics and a receiver model [34]. In this analysis, it is assumed that there is no spectral overlapping between the neighboring signals.

Due to the requirement of simplicity and cost-effectiveness, intensity modulation at the ground station transmitters and direct detection at the satellite receiver are deployed for the data communication part. To increase the spectral efficiency of the communications system, a SSB scheme is used where commercially available steep and narrow passband optical filters are used to suppress the redundant sideband of the non-return-to-zero (NRZ) signal [35]. Moreover, the effect of slow phase variations of the atmosphere [36, 37] are also considered, which is critical for the interference between neighboring data signals when the carrier separation is such that the cross-talk cannot be neglected. A MATLAB-based passband simulation tool is developed to perform simulations for the communication system, including the GEO uplink atmospheric channel. The SSB scheme is shown as an effective spectral efficient method that is achievable with commercially available optical filters. This scheme is optimized to find the maximum SE for a given data rate and filter parameters in a two-fold MISO setup. A lab experiment is performed to verify the generation of the SSB signals to increase the spectral efficiency by removing the redundant part of the spectrum. Finally, the diversity gain is obtained for a 32 Gb/s system by simulating an uplink atmospheric channel with weak turbulence and phase piston.

1.3. Key points of this thesis

1. Investigation of a transmitter diversity scheme for a non-reciprocal channel in an OGEOFL scenario with wavelength division scheme for multiplexing and OSSB scheme to increase spectral efficiency.
2. Analysis of the transmitter diversity scheme with residual pointing errors only.
3. Optimization of the transmit optical power of the individual beams for an M-fold transmitter diversity scheme considering beam wander and scintillation effects.
4. Establishment of an optical communications system simulation platform including the OSSB scheme and turbulent atmospheric channel including scintillation and phase piston effects.
5. Demonstration of the feasibility of the optimization of the OSSB scheme with a lab experiment.

A list of research work published during this thesis is given in Appendix A.

1.4. Structure of this thesis

Chapter 2 describes fundamentals of free-space optical communications, including characteristics of optical turbulence and its influence on the propagating beam towards the GEO satellite. Moreover, it explains the fading mitigation scheme used in this thesis and describes the optical communications system in detail.

Chapter 3 details the lab experiment performed to verify the benefits of the optical transmitter diversity scheme using 10Gb/s signal per channel.

Chapter 4 presents the analysis of the transmitter diversity scheme considering pointing errors only. It also includes a method to optimize an M-fold transmitter diversity scheme with beam wander and scintillation. Here, weak turbulence conditions are assumed, and the analysis is done using numerical simulations. It is assumed that there is no spectral overlap between the transmitted signals.

Chapter 5 describes the lab experiment to optimize the optical single-sideband scheme using commercially off-the-shelf narrow and steep optical filters. The quantitative assessment in increasing the spectral efficiency utilizing this scheme is also given.

Chapter 6 presents the simulation procedure to find the diversity gain in the presence of log-normal scintillation and phase piston. Here, the optical single-sideband scheme is also used to increase the spectral efficiency of the two-fold diversity system.

Finally, Chapter 7 summarizes of the thesis and presents the findings of the investigations done to show transmitter diversity as an effective fading mitigation technique in the GEO uplink scenario.

2. Fundamentals of free-space optical communications

2.1. Atmospheric extinction

As the optical beam propagates through the turbulent atmosphere, it is affected by the extinction and power loss due to scattering and absorption by the molecules and aerosols present in the air. The transmittance T is quantified by Beer's law [38] as given in Eq. (2.1)

$$T = \frac{I_L}{I_0} = \exp\left[-\alpha_e L\right] \tag{2.1}$$

where I_L is the intensity received at a distance L and I_0 is the intensity at the transmitter. The total extinction coefficient per unit length α_e given in dB/km, is a sum of molecular α_{mol} and aerosol scattering α_{aer} , and molecular β_{mol} and aerosol absorption β_{aer} as shown in Eq. (2.2)

$$\alpha_e = \alpha_{\text{aer}} + \alpha_{\text{mol}} + \beta_{\text{aer}} + \beta_{\text{mol}}. \tag{2.2}$$

The atmosphere consists of water, oxygen, and nitrogen molecules, which contribute to the absorption and scattering of photons even in clear-sky conditions [39]. The attenuation is wavelength-dependent due to which few atmospheric transmission windows exist, as shown in Fig. 2.1.

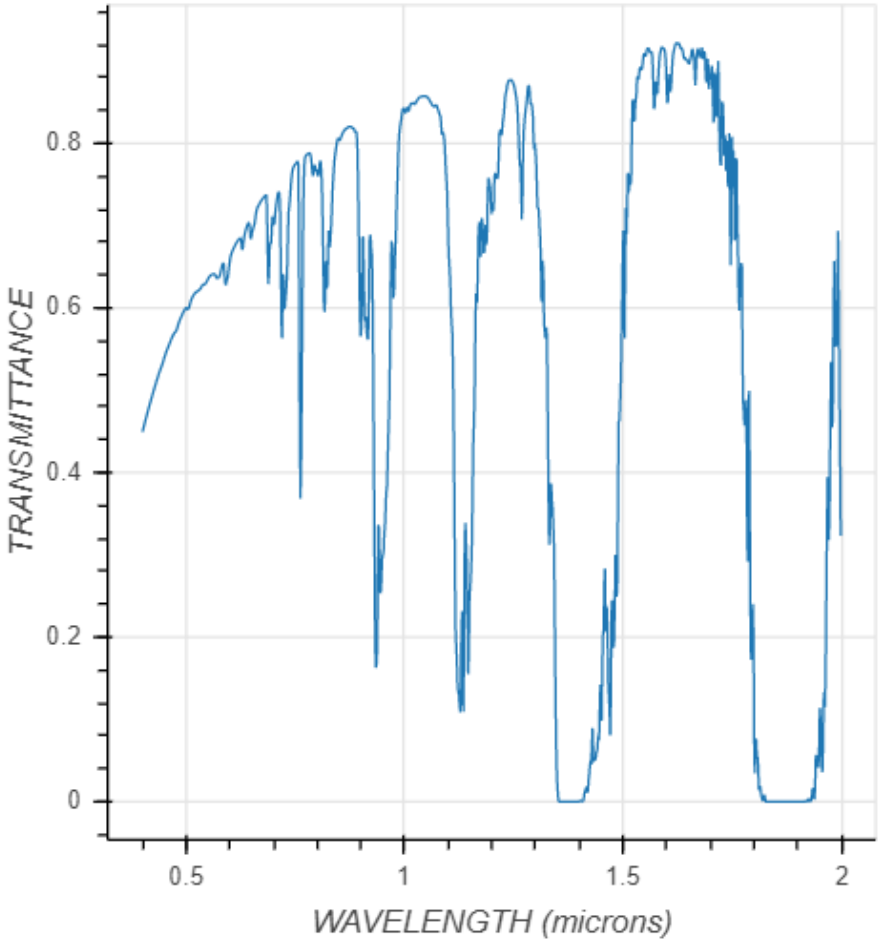

Figure 2.1.: Atmospheric spectral transmittance based on absorption analysis using MODTRAN showing transmission windows located in the regions of maximum transmittance. The atmospheric model is taken as Mid-Latitude Summer and aerosol model is Urban with a visibility of 23 km [2]

The usable region for optical communications is around 830 nm, 1064 nm, and 1550 nm where the spectral transmittance is maximum. These wavelengths are also favorable for communications due to the availability of technologies that are sensitive to these wavelengths, e.g., Silicon (Si) detectors for 830 nm, Nd-YAG lasers for 1064 nm, and InGaAs detectors, and EDFA for 1550 nm are widely available as commercial off-the-shelf components. Moreover, within these transmission windows, the molecular and aerosol absorption and molecular scattering are minimal in the near-infrared region due to the dependence on λ^{-4}. Therefore, the main contribution in the extinction α_e is due to the aerosol scattering [40] which reduces Eq. (2.2) to

$$\alpha_e = \beta_{\text{aer}} = \frac{3.91}{V}\left(\frac{\lambda}{550\,\text{nm}}\right)^{-p}$$

where V is the visibility in kilometers, λ is the wavelength of light in nanometers, and the exponent p is the coefficient dependent on the size distribution of the scattering particles. According to Kruse model [41], the typical values of p for high, moderate, and low visibility conditions are given in Table 2.1.

Visibility	p
V>50km	1.6
6km<V<50km	1.3
V<6km	$0.585 \cdot V^{1/3}$

Table 2.1.: Values of the coefficient dependent on the size distribution of the scattering particles p for different visibility conditions.

Further loss occurs due to attenuation and scattering of the photons propagating through raindrops and snow. According to the recommendation ITU-R P.1817, the specific attenuations α_{rain} and α_{snow} (both in dB/km) due to rain and snow are expressed as

$$\alpha_{\text{rain}} = 1.076 \cdot R_f^{0.67}$$

where R_f is the rainfall rate in mm/h

$$\alpha_{\text{snow}} = a \cdot S^b$$

where S is the snowfall rate in mm/h, a and b are the parameters which are functions of the wavelength in nm, and are given in Table 2.2.

Conditions	a	b
Wet snow	$0.0001023\frac{\lambda}{1\text{nm}} + 3.785546$	0.72
Dry snow	$0.0000542\frac{\lambda}{1\text{nm}} + 5.498776$	1.38

Table 2.2.: Parameters a and b for wet and dry snow

In the past, demonstration missions have used wavelengths in the range of 830 nm, e.g., in 2001, eurpopean space agency (ESA) performed the world-first Semiconductor-laser Inter-satellite Link EXperiment (SILEX) between its data-relay GEO satellite called advanced relay technology mission satellite (ARTEMIS) and the French Earth observation satellite SPOT-4 in low earth orbit (LEO) [10]. In 2006, Ground-to-satellite laser communication experiments between the OGS located in Tokyo and a LEO satellite, the Optical Inter-orbit Communications Engineering Test Satellite (OICETS) called "Kirari", were successfully performed by the Japan Aerospace Exploration Agency (JAXA) and the National Institute of Information and Communications Technology (NICT) [42]. Since 2017, the European Data Relay System (EDRS) has been using 1064 nm as the communication wavelength to communicate between the Sentinel satellites orbiting in LEO and the GEO satellites, at least in the first two nodes, i.e., EDRS-A and EDRS-C [43][44]. The third node, EDRS-D will have dual-wavelength

options (1064 nm and 1550 nm) to serve more commercial customers simultaneously [45]. Most of the currently deployed and upcoming satellite communications systems, including the mega-constellations, favor using 1550 nm because of eye safety reasons and, most importantly, the possibility of using commercially available technology from terrestrial fiber optical communications to cut the cost and reduce delivery times.

2.2. Atmospheric layers

The atmosphere consists of gaseous layers surrounding the earth extending around a hundred kilometers above the ground. As the altitude increases, both the pressure and temperature decrease, as shown in Fig. 2.2. The atmosphere is more dense and turbulent close to the surface, which is more relevant for FSO communications since it distorts the transmitted laser beam as it propagates through it. Generally, the strength of the turbulence is significant till the stratopause layer, which extends to around 20km from the ground. The laser beam gets distorted within this region, and beyond that, it spreads due to diffraction until it reaches the satellite.

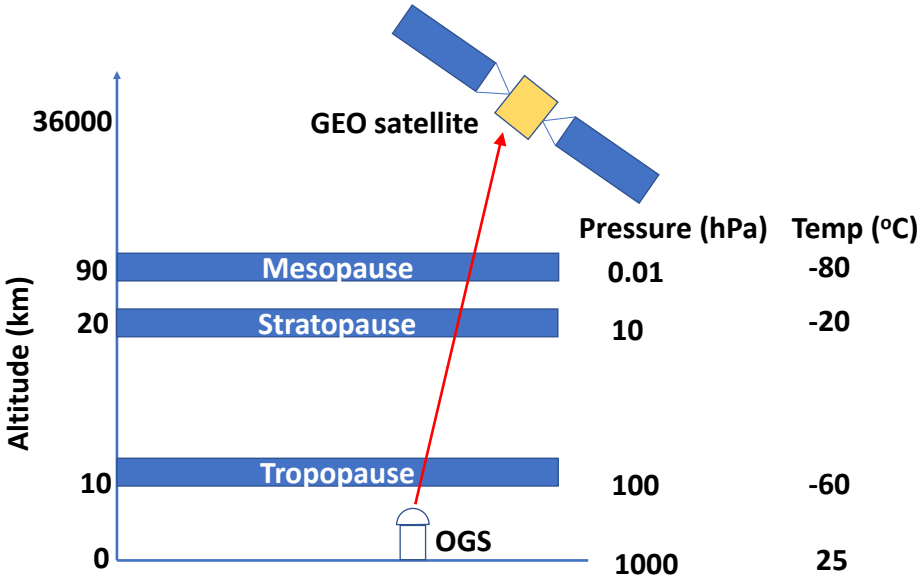

Figure 2.2.: A depiction of various atmospheric layers with corresponding air pressure and temperature [3]

2.3. Characteristics of optical turbulence

Turbulence is caused due to the mixing of hot and cold layers of air. The atmosphere can be understood as a viscous fluid where turbulent eddies of various sizes are generated due to the

dynamic mixing of the velocity flow. The reynold number R_n is used to differentiate between a laminar and turbulent flow. It is defined as $R_n = {}^{V_c \cdot l_f}/_{v_k}$, where V_c is the characteristic velocity of the flow, l_f is the characteristic size of the fluid, and v_k is the kinematic viscosity. When the fluid flow is greater than the critical R_n value, the flow turns into a random, haphazard state called turbulence. This turbulent flow causes temperature-dependent random fluctuations of refractive index, which is called optical turbulence. Kolmogorov developed the theory of turbulence [46], which is described in the following section.

2.3.1. Kolmogorov theory of turbulence

According to the Kolmogorov theory, the structure of atmospheric turbulence and the energy flow between different layers can be visualized as shown in Fig. 2.3. Energy from the solar heat is added to the large turbulence eddies on the outer scale L_0 , and it is dissipated through the small eddies on the inner scale l_0 . The eddy sizes between these two ends are called inertial subrange. The eddies smaller than l_0 belong to the viscous dissipation range. In this region, the turbulent eddies vanish, and the remaining energy in the fluid motion is dissipated as heat.

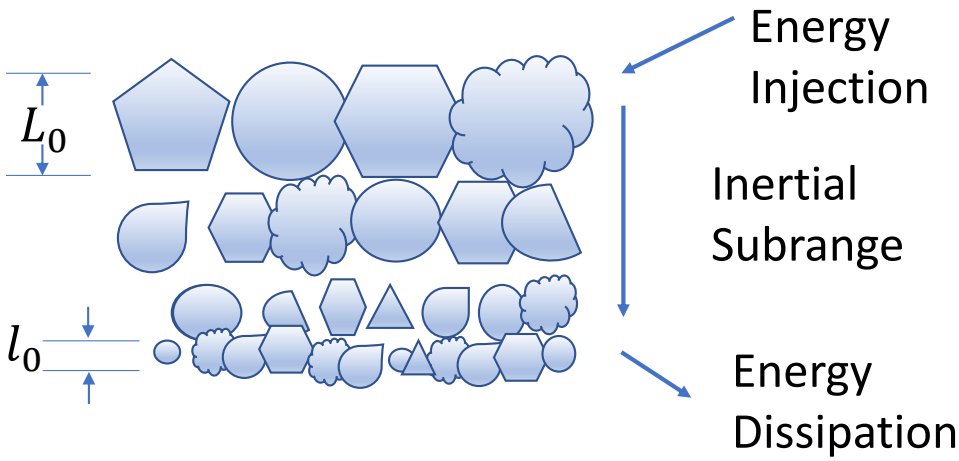

Figure 2.3.: Depiction of optical turbulence based on the Kolmogorov model described in [3]

2.3.2. Wind velocity fluctuations and satellite motion

The mean wind speed affects the strength and temporal frequency of the wavefront fluctuations. The strength of the turbulence depends on the energy of the process, which means strong winds inject energy in the turbulent fluid, which increases the turbulence with the square of the wind velocity as shown in Eq. (2.8). The coherence time of the phase perturbations decreases linearly with wind speed which is related to the Taylor frozen-turbulence hypothesis. It states that temporal changes of statistical quantities at a given point occur due to the advection of

these quantities caused by the mean wind speed flow and not due to the changes in the quantities themselves. These quantities can be considered constant during this time. The rms mean wind speed v in m/s is calculated from

$$v = \left[\frac{1}{15 \cdot 10^3} \int_{5 \cdot 10^3}^{20 \cdot 10^3} V^2(h) dh \right]^{1/2} \tag{2.3}$$

where $V(h)$ is described by the Bufton model for wind velocity, which follows the Gaussian shape given by [47]

$$V(h) = \omega_{\mathrm{sr}} + v_{\mathrm{g}} + v_{\mathrm{T}} \cdot \exp\left[\left(\frac{h - H_{\mathrm{T}}}{L_{\mathrm{T}}} \right)^2 \right]$$

where ω_{sr} is the slew rate for a satellite pass going through the zenith as seen from the ground station, v_{g} is the wind velocity at low altitudes, v_{T} , H_{T} , and L_{T} are wind velocity, height, and thickness of tropopause, respectively. As an example, the wind profile for the Bufton wind model is shown in Fig. 2.4, which is obtained using Greenwood parameters given in Table 2.3. It can be seen that the wind blows with maximum speed at around 9 km which is the altitude of the tropopause layer.

Parameters	v_{g} [m/s]	v_{T} [m/s]	H_{T} [m]	L_{T} [m]
Values	8	30	$9.4 \cdot 10^3$	$4.8 \cdot 10^3$

Table 2.3.: Greenwood parameters for the Bufton wind model

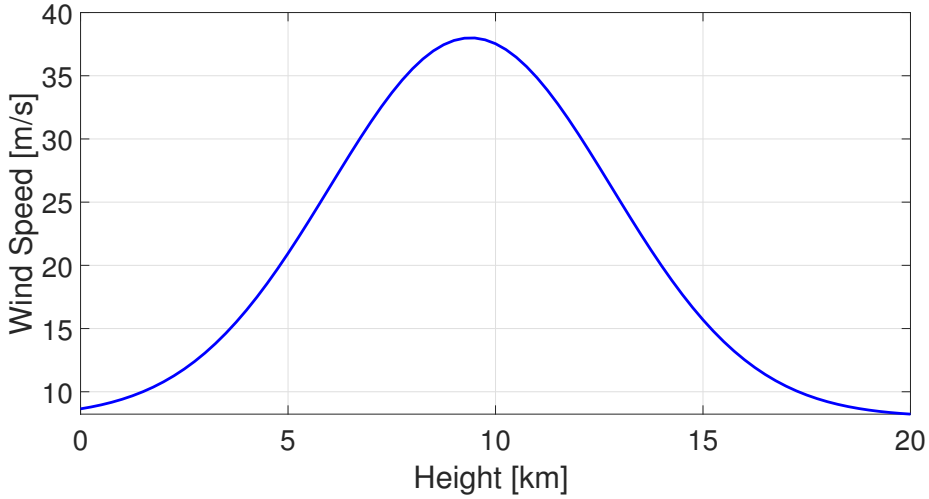

Figure 2.4.: Wind speed profile for the Bufton wind model using Greenwood parameters

The slew rate ω_{sr} in deg/s is given by

$$\omega_{\mathrm{sr}} = \frac{V_{\mathrm{sat}}}{L} \frac{L^2 + H_{\mathrm{sat}}^2 + 2R_{\mathrm{e}}H_{\mathrm{sat}}}{2L\left(H_{\mathrm{sat}} + R_{\mathrm{e}}\right)} \tag{2.4}$$

where V_{sat} is the satellite velocity in m/s, H_{sat} is the altitude of the satellite from the ground in meters, R_{e} is the radius of the earth in meters, and L is the distance from the ground to the satellite in meters and is given by

$$L = \sqrt{\left(H_{\mathrm{sat}} + R_{\mathrm{e}}\right)^2 - R_{\mathrm{e}}^2 \cos^2\left(\varepsilon\right)} - R_{\mathrm{e}} \sin\left(\varepsilon\right)$$

where ε is the elevation angle between the ground station and the satellite. The slew rate contributes to the wind velocity for LEO satellite links as cross wind due to the relative motion between the fast-moving satellite and ground station. The slew rate for the LEO satellites orbiting at 510 km at a speed of 28000km/h is calculated using Eq. (2.4) and is shown in Fig. 2.5 where it can be seen that the largest slew rate occurs at zenith. In comparison, the slew rate of GEO satellites is around two orders of magnitude less compared to LEO satellites, i.e., around 0.0042 deg/s [48] since the former satellites remain virtually fixed w.r.t their ground stations. Due to this reason, the effects related to ω_{sr} are ignored in this thesis.

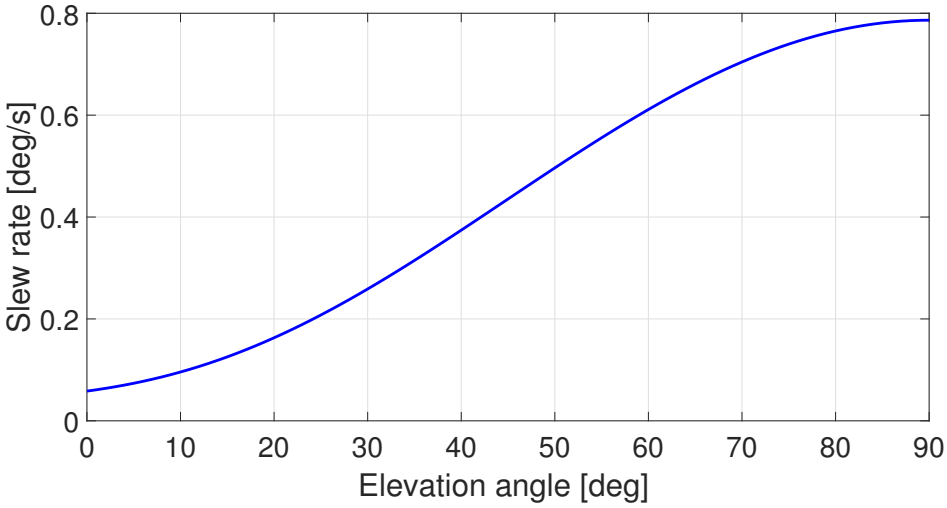

Figure 2.5.: Slew rate of the satellite beam as a function of the elevation angle

2.3.3. Refractive index variations

Optical phase fronts are distorted by the index of refraction changes in the turbulent medium. The index of refraction varies with temperature fluctuations which are even more vital when the turbulent mixing is great, i.e., during mid-day. It causes phase delays to the rays of light resulting in perturbation of the beam. The index of refraction $n\left(r,t\right)$, at a location r and at a specific time t, is defined as

$$n(r,t) = n_0 + n_1(r,t) \tag{2.5}$$

where n_0 is the average value of the index of refraction and $n_1(r,t)$ expresses the random fluctuation of $n(r,t)$ from its mean value. Moreover, variations in the index of refraction turbulence depend on the variations in temperature and pressure. The time-independent form of Eq. (2.5) can be mathematically expressed as

$$n(r) \approx 1 + 79 \cdot 10^{-6} \frac{P(r)}{T(r)} \cdot \frac{\mathrm{K}}{\mathrm{mbar}} \tag{2.6}$$

where $P(r)$ is the atmospheric pressure in mbar and $T(r)$ is the atmospheric temperature in Kelvin. Kolmogorov results provide the behavior of the structure function $D_n(\rho)$, which is represented in terms of refractive-index fluctuations. The structure function of the refractive-index between two points which are separated by a distance ρ along the coordinate r is defined by

$$D_n(\rho) = \left\langle [n(r) - n(r+\rho)]^2 \right\rangle. \tag{2.7}$$

The angle brackets represent the ensemble average. As the separation ρ between the two observed points increases, the two refractive index points become more and more uncorrelated, and $D_n(\rho)$ increases. Here, the assumption of homogeneity and isotropy for the turbulence field allows using the structure function's dependence on only one parameter, i.e., the separation distance ρ. The two asymptotic behaviors of the Kolmogorov structure function from Eq. (2.7) are

$$D_n(\rho) = \begin{cases} C_n^2 \rho^{2/3}, & l_0 \ll \rho \ll L_0 \\ C_n^2 l_0^{-4/3} \rho^2, & 0 \leq \rho \ll l_0 \end{cases}$$

where C_n^2 is the refractive index structure parameter given in the units of $\mathrm{m}^{-2/3}$. It represents the strength of the refractive index fluctuations and mainly depends on the height of the optical ground station from ground and local weather conditions. The commonly used C_n^2 profile is obtained from Hufnagel-Valley model, also written as $\mathrm{HV}_{5/7}$

$$C_n^2(h) = 0.00594 \cdot (v/27)^2 \cdot \left(10^{-5} h\right)^{10} \cdot e^{-h/1000} + 2.7 \cdot 10^{-16} e^{-h/1500} + A_0 \cdot e^{-h/100}. \tag{2.8}$$

where h is the height in meters, v is the rms wind speed in m/s as given in Eq. (2.3), and A_0 is the nominal value of C_n^2 at the ground. The $\mathrm{HV}_{5/7}$ model is derived for the case when $\lambda = 500\,\mathrm{nm}$, $r_0 = 5\,\mathrm{cm}$, $\theta_0 = 7\mu\mathrm{rad}$, $A_0 = 1.7 \cdot 10^{-14}\mathrm{m}^{-2/3}$, and $v = 21\,\mathrm{m/s}$. The parameters r_0 and θ_0 are explained in Section 2.3.7 and Section 2.3.9, respectively. It is to be noted that this model is not accurate when the optical ground station is located at an altitude H_{OGS} from the ground. The modified HV model taking into account H_{OGS} is given by [49]

$$C_n^2(h) = 0.00594\,(v/27)^2 \cdot \left(10^{-5}h\right)^{10} e^{-h/1000} + 2.7\cdot 10^{-16} e^{-h/1500} + A_0 \cdot e^{-H_{\mathrm{OGS}}/700} e^{-(h-H_{\mathrm{OGS}})/100}. \tag{2.9}$$

The unit of the constants in each term of Eq. (2.8) and Eq. (2.9) is $\mathrm{m}^{-2/3}$. The units of the denominator in the parenthesis of the first term and the denominators of the exponentials are $\mathrm{m}^{-2/3}$ and m, respectively. The comparison between the two C_n^2 is shown in Fig. 2.6 where H_{OGS} in Eq. (2.9) is taken as 2370 m which is the height of the ground station at Tenerife in Spain. Comparing the two curves, one can notice that appropriate C_n^2 has to be taken into account for reliable modeling of turbulence strength. As mentioned before that the statistical models of the C_n^2 profile are location-dependent, e.g., a C_n^2 model for the ESA OGS at Tenerife is developed for the night time conditions and is given as [50]

$$C_n^2 = \begin{cases} C_{n0}^2 \left(\frac{h}{h_s}\right)^{-2/3} & h \le h_s \\ C_{n0}^2 & h_s < h < h_i \\ C_{n0}^2 \exp\left(\frac{h_i}{h_r}\right) \exp\left(-\frac{h}{h_r}\right) + C_{nl}^2 \exp\left(\frac{h}{h_l}\right) + C_{nl}^2 3 V_w^2 \left(\frac{h}{h_t}\right)^{10} \exp\left(-\frac{10h}{h_t}\right) & h > h_i \end{cases} \tag{2.10}$$

where the set of parameters considered for this model are given in Table 2.4.

Parameter	Description	Value	Unit
h_s	Surface layer height	4	m
h_i	Inversion layer height	30	m
h_0	Reference height in the $h^{-4/3}$ – dependence region	$\geq h_s$	m
h_r	Space constant for the transition between the inversion layer (night) or the $h^{-4/3}$- dependence region (day) and the free atmosphere	100	m
h_l	Space constant of the exponential decrease of C_n^2 in the free-atmosphere	1500	m
h_t	Height of the tropopause C_n^2 peak	13000	m
C_{n0}^2	C_n^2 value throughout the inversion layer	$9.5\cdot 10^{-15}$	$\mathrm{m}^{-2/3}$
C_{nl}^2	Structure-constant characteristic value for the free atmosphere	$4.5\cdot 10^{-17}$	$\mathrm{m}^{-2/3}$
V_w	Root mean square value of the wind velocity between 5 km and 20 km heights	30	m/s

Table 2.4.: Values of the parameters considered for the C_n^2 turbulence model in Eq. (2.10)

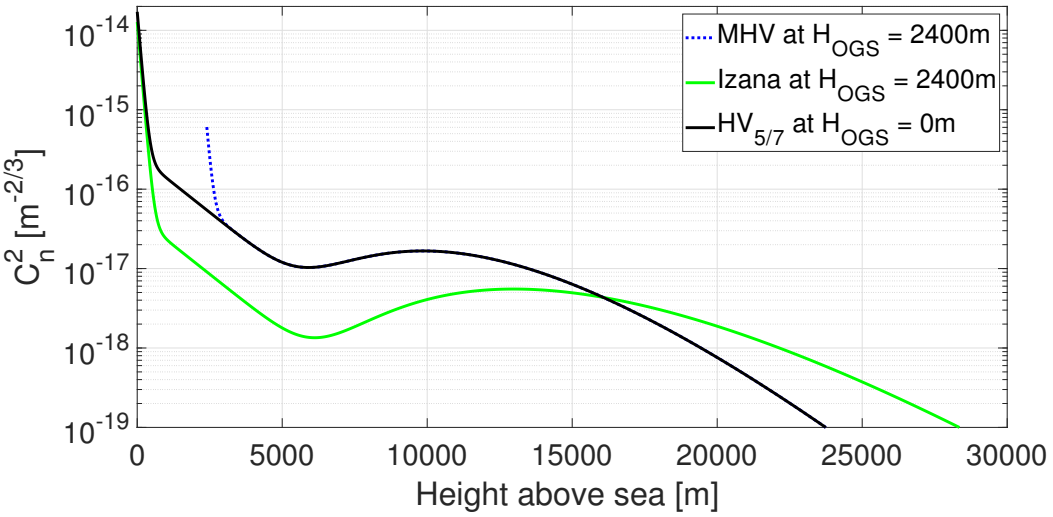

Figure 2.6.: Refractive-index structure parameter C_n^2 profiles using various models. Night time conditions are considered in all the models. To better visualize the effect of an OGS located at a certain altitude, a linear height scale is used

The structure function is related to the power spectrum $\Phi_n(\kappa)$ of the refractive index by

$$D_n(\rho) = 8\pi \int_0^\infty \kappa^2 \Phi_n(\kappa) \left(1 - \frac{\sin(\kappa\rho)}{\kappa\rho}\right) d\kappa$$

where κ is the scalar spatial frequency in rad/m. Kolmogorov derived an expression for the 3-dimensional power spectrum given by

$$\Phi_n(\kappa) = 0.033 C_n^2 \kappa^{-11/3}, \qquad 1/L_0 \ll \kappa \ll 1/l_0. \tag{2.11}$$

This model is valid only for the inertial subrange $1/L_0 \ll \kappa \ll 1/l_0$. Often it is assumed that the outer scale is infinite ($L \to \infty$) and the inner scale is negligible small ($l_0 \to 0$). However, in reality, making this assumption can lead to wrong results when using the Kolmogorov spectrum for κ values out of the inertial subrange. When inner and outer scales cannot be ignored, other models are proposed. These models include the von Karman spectrum given by

$$\Phi_n(\kappa) = \frac{0.033 C_n^2}{\left(\kappa^2 + \kappa_0^2\right)^{11/6}}, \qquad 0 \leq \kappa \ll 1/l_0 \tag{2.12}$$

and modified von Karman spectrum given by

$$\Phi_n(\kappa) = 0.033 C_n^2 \frac{\exp\left(-\kappa^2/\kappa_m^2\right)}{\left(\kappa^2 + \kappa_0^2\right)^{11/6}}, \qquad 0 \leq \kappa < \infty. \tag{2.13}$$

where $\kappa_0 = {}^{2\pi}/_{L_0}$ and $\kappa_m = {}^{5.92}/_{l_0}$ are the spatial frequencies corresponding to the outer scale L_0 and inner scale l_0, respectively. It can be seen in Fig. 2.7 that in the Kolmogorov regime, ${}^{-11}/_{3}$ power law is observed on all spatial scales. The von Karman breaks down at low spatial frequencies, i.e., at outer scale. The modified von Karman spectrum takes into account the spatial frequencies from outer scales to inner scales. Another model is the modified atmospheric spectrum given by [51]

$$\Phi_n(\kappa) = 0.033C_n^2\left[1 + 1.802\left(\frac{\kappa}{\kappa_l}\right) - 0.254\left(\frac{\kappa}{\kappa_l}\right)^2\right]\frac{\exp\left(-\kappa^2/\kappa_l^2\right)}{\left(\kappa^2+\kappa_0^2\right)^{11/6}}, \qquad 0 \le \kappa < \infty. \tag{2.14}$$

where $\kappa_l = {}^{3.3}/_{l_0}$ and $\kappa_0 = {}^{1}/_{L_0}$

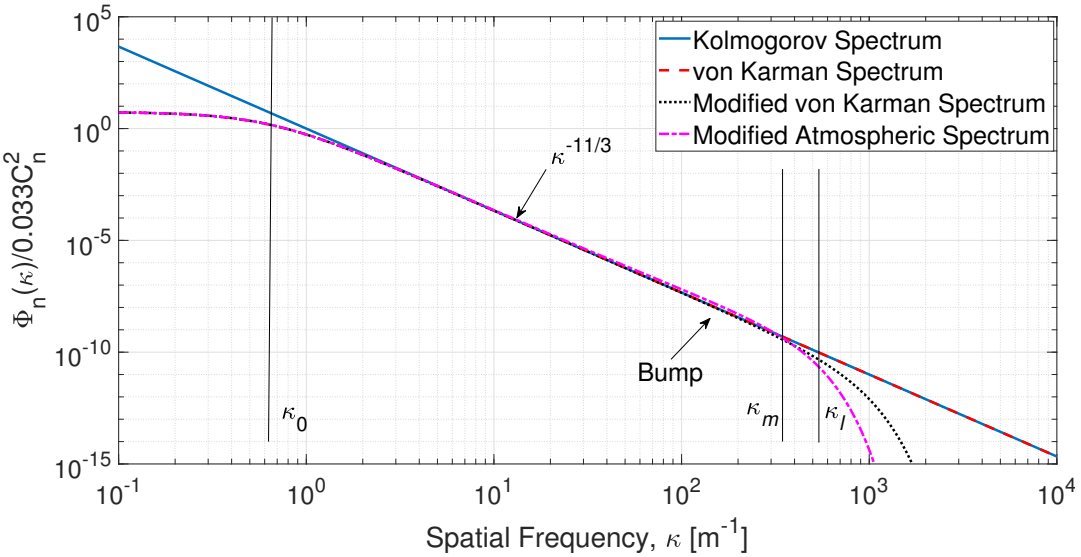

Figure 2.7.: Spatial power spectra of refractive-index fluctuations of Kolmogorov, von Karman, modified von Karman, and modified atmospheric models as given by Eq. (2.11), (2.12), (2.13), and (2.14), respectively

The two main effects of turbulence on the laser beam which are relevant for this thesis are:

1. Redistribution of the energy within the beam area: As the plane wave propagates through the turbulence with varying refractive indices among different layers, the wavefront gets distorted, leading to constructive and destructive interference within the beam itself. The result of this interference is the variation in the satellite receiver's optical intensity, also called scintillation.
2. Beam wander: When the beam with a size smaller than the turbulent cells propagates through different layers of atmospheric turbulence, the laser beam loses its direct line of sight to the satellite. Instead, the beam centroid wanders around the optical axis. This leads to miss pointing errors which are seen as a sharp drop in the received intensity at the satellite.

These two effects are the significant showstoppers in closing the link in the GEO feeder link applications [48].

2.3.4. Gaussian beam

In this thesis, the lowest-order transverse electromagnetic (TEM) Gaussian-beam wave, TEM_{00} is considered for free-space propagation. The transmitting aperture is assumed to be located in the plane $z = 0$, and the intensity distribution follows a Gaussian bell shape with the spot size W_0 which represents the radius at which the beam intensity drops to $1/e^2$ of the maximum value on the beam axis, also called the beam waist. Additionally, a parabolic phase front is assumed with a radius of curvature F_0 . This results in the intensity distribution, which is given at the transmitting aperture as

$$I(r,0) = I_0 \cdot \exp\left(\frac{-2r^2}{W_0^2}\right) \cdot \exp\left(\frac{-ikr^2}{F_0}\right)$$

where k is the wavenumber and is equal to $2\pi/\lambda$ and $r = \sqrt{x^2 + y^2}$ is the radial distance from the on-axis. For the collimated beam, F_0 is taken as infinity resulting in the normalized intensity profile as shown in Fig. 2.8.

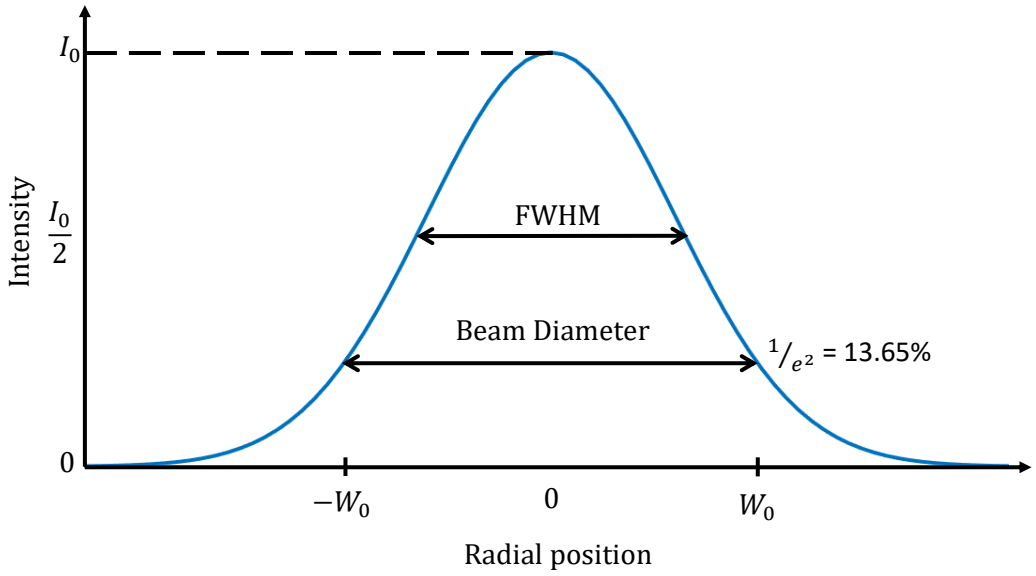

Figure 2.8.: Intensity profile of a Gaussian TEM_{00} beam

The beam parameters which can analyze the Gaussian beam waves in free-space at the input plane are given as

$$\Theta_0 = 1 - \frac{L}{F_0}$$

$$\Lambda_0 = \frac{2L}{kW_0^2}$$

and the parameters at the output plane for a beam that has propagated a distance L are given as

$$\Theta = 1 + \frac{L}{F} = \frac{\Theta_0}{\Lambda_0^2 + \Theta_0^2}$$

$$\Lambda = \frac{2L}{kW^2} = \frac{\Lambda_0^2}{\Lambda_0^2 + \Theta_0^2}.$$

2.3.5. Power vector for optical GEO feeder link

Due to the wavefront distortions of the optical wave caused by the turbulent atmosphere, variations in the power at the satellite receiver are seen. It is also known as scintillation, which is quantified by scintillation index σ_{I}^2 defined as the normalized variance of the received intensity. The relation is given by [3]

$$\sigma_I^2 = \frac{\langle I^2 \rangle - \langle I \rangle^2}{\langle I \rangle^2} = \frac{\langle I^2 \rangle}{\langle I \rangle^2} - 1.$$

The on-axis scintillation index for the tracked beam is given as

$$\sigma_I^2 = \exp\left[\frac{0.49\sigma_{\mathrm{Bu}}^2}{(1+0.56(1+\Theta)\sigma_{\mathrm{Bu}}^{12/5})^{7/6}} + \frac{0.51\sigma_{\mathrm{Bu}}^2}{(1+0.69\sigma_{\mathrm{Bu}}^{12/5})^{5/6}}\right] - 1. \tag{2.15}$$

This is valid for weak, moderate, and strong fluctuations. The Rytov index σ_{Bu}^2 is given by

$$\sigma_{\mathrm{Bu}}^2 = 8.70\mu_{3u}k^{7/6}\sec^{11/6}(\zeta)(L - H_{\mathrm{OGS}})^{5/6} \qquad 0 \leq \sigma_{\mathrm{Bu}}^2 < \infty \tag{2.16}$$

where L is the path length that depends on the zenith angle and orbit height, and

$$\mu_{3u} = \mathrm{Re}\int_{H_{\mathrm{OGS}}}^{L} C_n^2(h)\left\{\xi^{5/6}\left[\Lambda\xi + i\left(1 - \overline{\Theta}\xi\right)\right]^{5/6} - \Lambda^{5/6}\xi^{5/3}\right\}dh$$

where $\xi = 1 - \frac{(h-h_0)}{(H-h_0)}$, $\overline{\Theta} = 1 - \Theta$, and expressions related to Λ are given in Section 2.3.4. Assuming the ground station at sea level, the value of $C_n^2(h)$ can be numerically calculated using Eq. (2.8). The results from Eq. (2.15) and Eq. (2.16) are plotted in Fig. 2.9 where it can be seen that for weak turbulence, $\sigma_{\mathrm{I}}^2 \approx \sigma_{\mathrm{Bu}}^2$.

The elevation angle ε for the case of OGEOFL is taken as 60 degrees which corresponds to $\sigma_{\mathrm{I}}^2 \approx 0.05$ as shown in Fig. 2.9. It can also be seen that the scintillation index σ_{I}^2 decreases

as the elevation angle increases. This is because the laser beam has to propagate through less volume of turbulence as compared to zenith, i.e., when the ground station directly looks up at the satellite.

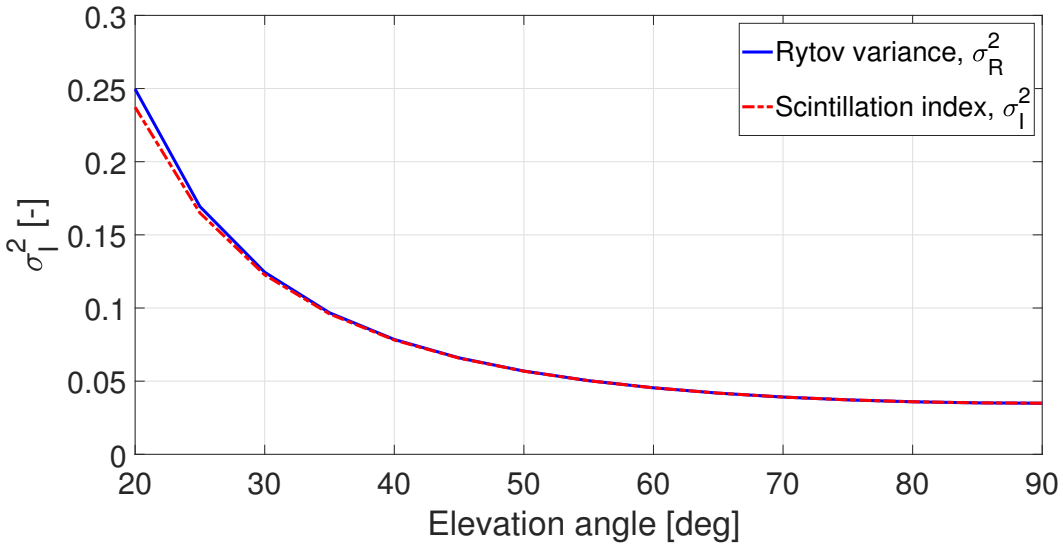

Figure 2.9.: Comparison of between the scintillation index and Rytov variance for a tracked beam in a satellite uplink

Fig. 2.10 is an example of a 500 ms long power vector measured at the GEO satellite ARTEMIS [4]. The σ_I^2 for this vector is 0.30 which represents weak scintillation. This power vector is used in the simulations described in Chapter 6

2.3.6. Scintillation loss

The fading loss L_{sci} due to scintillation for an on-off keying (OOK) system with direct detection can be calculated as [52]

$$L_{sci} = -4.343\left[\text{erf}^{-1}\left(2p_{thr}-1\right)\sqrt{2\ln\left(\sigma_P^2+1\right)}-\frac{1}{2}\ln\left(\sigma_P^2+1\right)\right] \tag{2.17}$$

where erf(.) is the error function, p_{thr} is the fraction of signal loss duration where the received power drops below the set threshold from the mean power. This threshold is also called the receiver sensitivity, which is the minimum received power to achieve a specific BER in a digital receiver. Eq. (2.17) is graphically represented in Fig. 2.11 where it can be seen that the scintillation loss increases for a lower p_{thr} value. It is also worth noticing that L_{sci} decreases with the elevation angle because of its inverse relationship with the σ_P^2 as can be seen in Fig. 2.9.

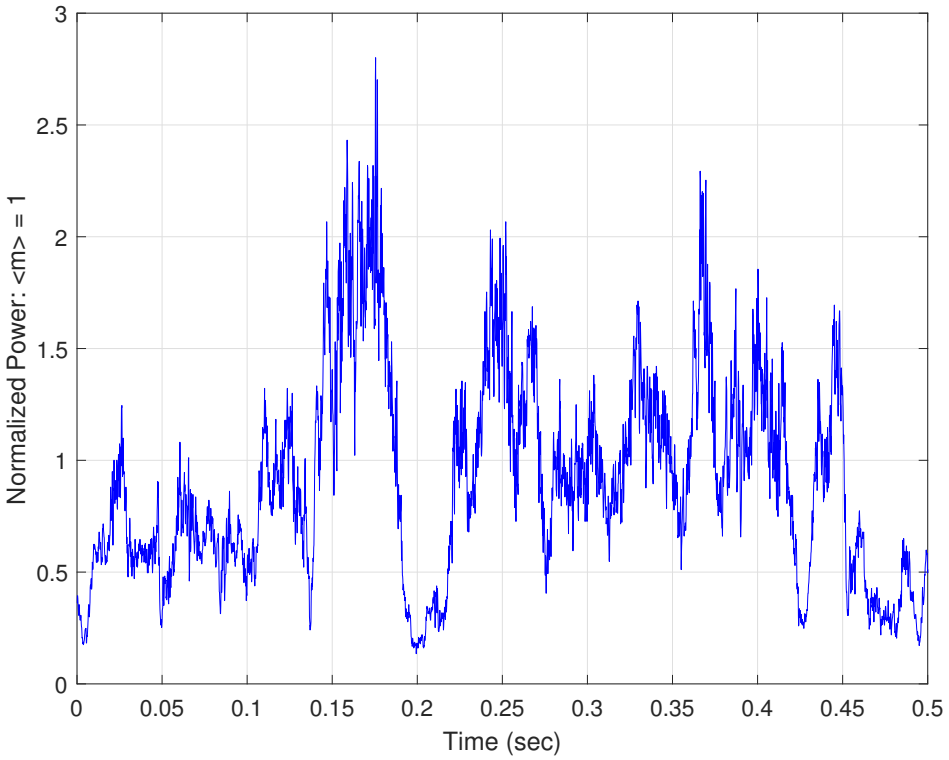

Figure 2.10.: Measured received power at the GEO satellite with 8 kHz sampling frequency. The data is taken from the ARTEMIS measurement campaign [4]

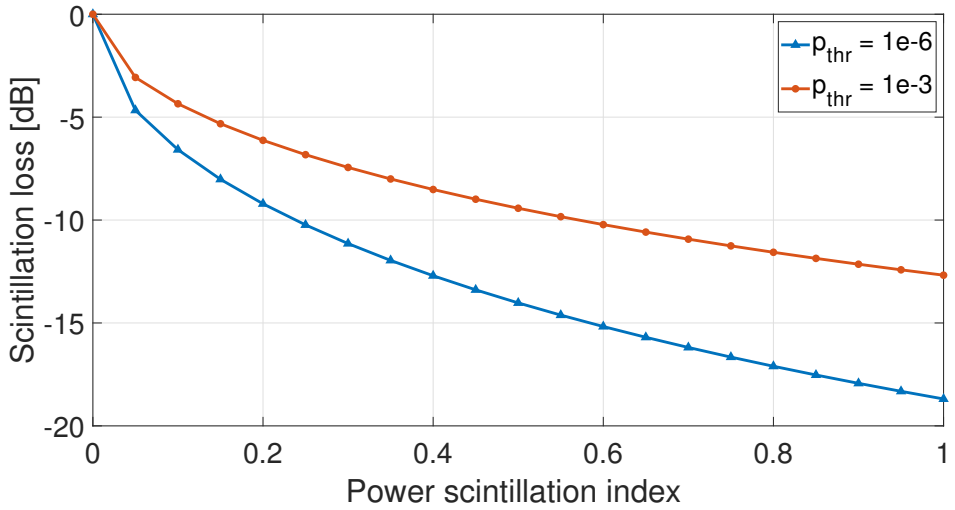

Figure 2.11.: Scintillation loss L_{sci} as a function of power scintillation index σ_{P}^2 for two different threshold values p_{thr}

2.3.7. Fried parameter - The atmospheric coherence width

As the wave propagates through the turbulent atmosphere, its degree of transverse spatial coherence decreases. This loss of coherence is quantified by the spatial coherence radius ρ_0. Transverse spatial coherence radius for the plane wave is given by Eq. (2.18)

$$\rho_0 = \left[1.46k^2 \sec(\zeta) \int_{H_{\mathrm{OGS}}}^{L} C_n^2(h)\, dh\right]^{-3/5}. \tag{2.18}$$

The coherence radius increases with the wavelength as $\lambda^{6/5}$. This is why longer wavelengths like radio waves are less affected by the turbulent atmosphere. Also, as shown in Fig. 2.12, the coherence loss is less for higher elevation angles ε because the beam has to propagate less volume of turbulent atmosphere. It is related to the commonly known Fried parameter, which is given by Eq. (2.19)

$$r_0 = 2.1\rho_0. \tag{2.19}$$

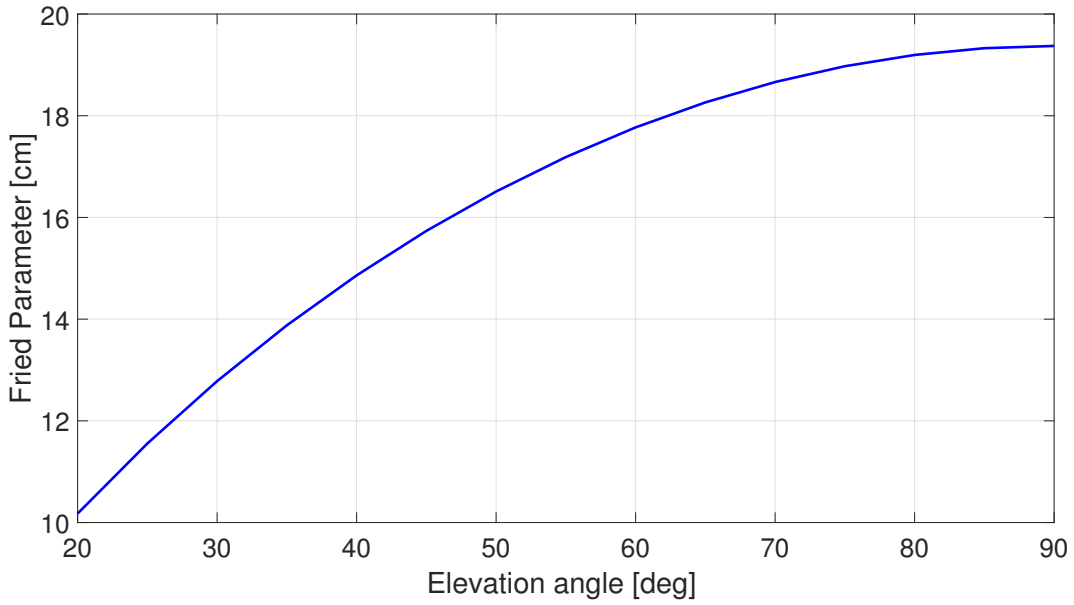

Figure 2.12.: Fried Parameter dependence on the elevation angle

For the case of an uplink, the optical beam propagates through the first 20km of turbulent atmosphere, where all the phase distortions occur. After that, practically no atmosphere exists, and the beam propagates in a vacuum without any further distortion. The beam expands only due to pure diffraction in this region of the vacuum of space. When it reaches GEO satellite positioned at around 38,000km from the surface of the earth, the size of the beam and r_0 is large compared to the receiver whose size is around 13.5cm as is the case with the TESAT laser communications terminal (LCT) on board the AlphaSat satellite [53]. In this case, the receiver is considered as a point receiver. Therefore, SMF coupling is possible for the uplink,

and DWDM technology in combination with single-mode EDFA can be used to achieve Tb/s throughput.

2.3.8. Beam wander

Beam wander at the receiver plane is the deviation of the beam centroid from its on-axis when the turbulent size is larger than the beam size. The movement of the short-term beam, as shown by the solid circles in Fig. 2.13 gives rise to a large spot when integrated over a long time which is known as long-term spot size W_{LT} . The mathematical expression is given by [3]

$$W_{\mathrm{LT}}^2 = W^2(1+T) \tag{2.20}$$

where $T = T_{\mathrm{SS}} + T_{\mathrm{LS}}$ represents the contribution from small-scales(SS) and large-scales(LS) expanding Eq. (2.20) to

$$W_{\mathrm{LT}}^2 = W^2 + W^2 T_{\mathrm{SS}} + W^2 T_{\mathrm{LS}}$$

where $W = W_0\sqrt{\Theta_0^2 + \Lambda_0^2}$. Writing short-term beam spread as $W_{\mathrm{ST}} = W\sqrt{1+T_{\mathrm{SS}}}$ gives the relation between long-term beam spread and beam wander variance $\langle r_c^2 \rangle$ as [54]

$$W_{\mathrm{LT}}^2 = W_{\mathrm{ST}}^2 + \langle r_c^2 \rangle .$$

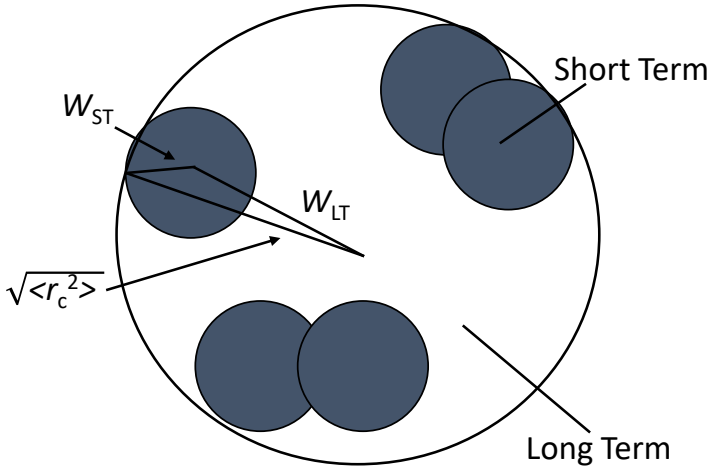

Figure 2.13.: Long-term spot size in the receiver plane formed by short-term beam spread and beam wander [3]

The beam wander displacement under the weak irradiance fluctuation conditions for an uplink beam is represented as

$$\sqrt{\langle r_c^2 \rangle} = 0.73\,(H - H_{\mathrm{OGS}})\sec(\zeta)\left(\frac{\lambda}{2W_0}\right)\left(\frac{2W_0}{r_0}\right)^{5/6}\left[1-\left(\frac{\kappa_0^2 W_0^2}{1+\kappa_0^2 W_0^2}\right)^{1/6}\right]^{1/2} \tag{2.21}$$

where ζ is the zenith angle. Considering Kolmogorov spectrum where $\kappa_0 = 0$ due to the infinite size of outer scale L_0, Eq. (2.21) reduces to

$$\sqrt{\langle r_c^2 \rangle} = 0.73\,(H - H_{\mathrm{OGS}})\sec(\zeta)\left(\frac{\lambda}{2W_0}\right)\left(\frac{2W_0}{r_0}\right)^{5/6}. \tag{2.22}$$

Usually, angular beam wander $\theta_{\mathrm{BW}} = \frac{\sqrt{\langle r_c^2 \rangle}}{L}$ in rad is used to represent the angular tilt at the transmitter side. Assuming $\lambda = 1550$nm as the transmission wavelength, $H = 38.5 \cdot 10^3$km as the altitude of the GEO satellite, $W_0 = 2.8$cm and using r_0 from Eq. (2.19), the graphical representation of Eq. (2.22) can be shown in Fig. 2.14 where it can be seen that the beam wander reduces as elevation angle increases because it propagates through less volume of turbulent atmosphere.

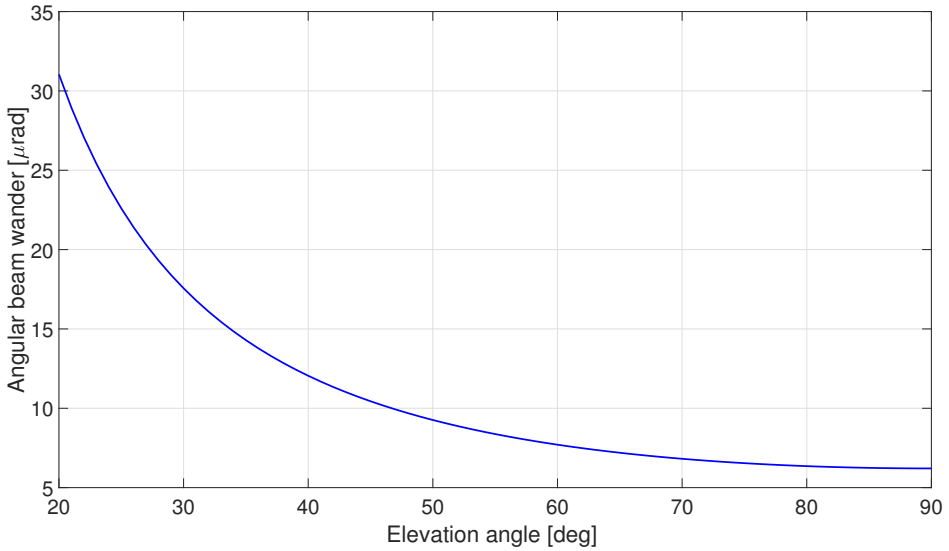

Figure 2.14.: Angular beam wander in relation to the elevation angle in the case of an uplink to the GEO satellite

It can be seen in Eq. (2.21) that the beam wander is significant for small r_0. If the beam wander is greater than the beam divergence, it leads to strong fades at the satellite receiver. One solution to compensate for beam wander is to increase the beam divergence but doing so reduces the mean received power at the satellite, adversely affecting the receiver sensitivity and the link budget. An example of fading that includes a contribution from both scintillation and pointing errors due to the atmospherically induced beam wander is shown in Fig. 2.15 where

the fades as high as 10dB and 20dB can be seen at multiple instances. This becomes crucial for high-speed data transmission in the order of Gb/s per channel to achieve Tb/s throughput when utilizing DWDM systems. The length of these fades can be in milliseconds [55] which means the loss of millions of bits. It is to be noted that the measurement shown in Fig. 2.15 is done with the 820nm wavelength of light because the Artemis satellite supported this wavelength. The power vector shown in Fig. 2.10 is used to simulate transmitter diversity in Section 6.1.9. However, most of the current and future missions will use 1550nm wavelength because of the already available technology developed for optical fiber communications. Therefore, the rest of the analysis and experiments given in this thesis are done with 1550nm wavelength. The use of 1550nm brings an added advantage of experiencing less scintillation and beam wander as compared to using shorter wavelengths.

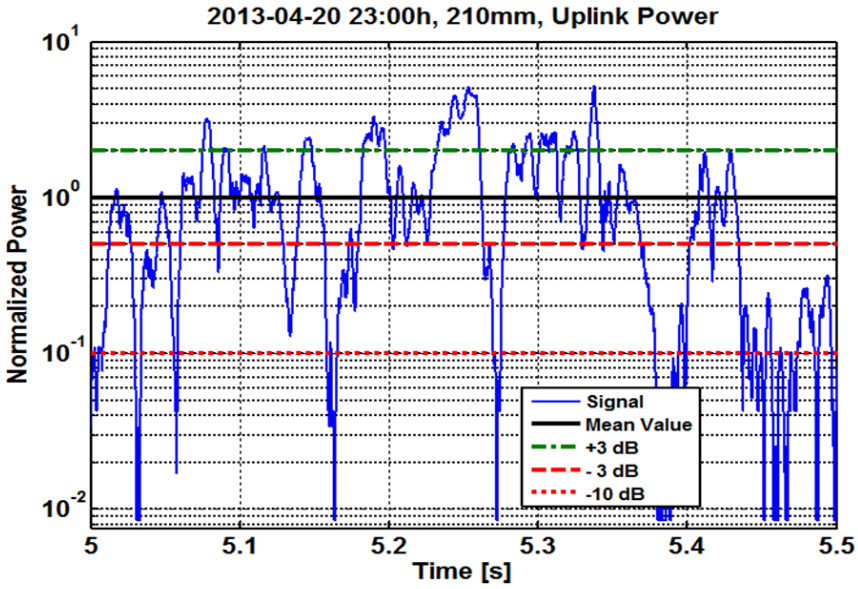

Figure 2.15.: Example of a measured optical received power in the uplink channel from the ESA's OGS at Tenerife to the GEO satellite ARTEMIS. This power vector is taken from a measurement carried out as part of the ArtemEx test campaign by DLR researchers [4]

2.3.9. Isoplanatic angle

Isoplanatic angle θ_0 is the angular distance w.r.t the reference beam over which the atmospheric turbulence remains unchanged. For an upward-propagating Gaussian-beam wave, the isoplanatic angle is defined by [3]

$$\theta_0 = \frac{\cos^{8/5}(\zeta)}{(H - H_{\mathrm{OGS}})\left[2.91k^2\left(\mu_{1\mathrm{u}} + 0.62\mu_{2\mathrm{u}}\Lambda^{11/6}\right)\right]^{3/5}} \tag{2.23}$$

where

$$\mu_{1\mathrm{u}} = \int_{H_{\mathrm{OGS}}}^{L} C_n^2(h)\left[\Theta + \overline{\Theta}\frac{(h-h_0)}{(H-h_0)}\right]^{5/3} dh$$

$$\mu_{2\mathrm{u}} = \int_{H_{\mathrm{OGS}}}^{L} C_n^2(h)\left(\frac{h-h_0}{H-h_0}\right)^{5/3} dh.$$

For a 2cm beam and $\lambda = 1550$nm, the Isoplanatic angle θ_0 from Eq. (2.23) is plotted in Fig. 2.16 where θ_0 can be seen to rise with the elevation angle.

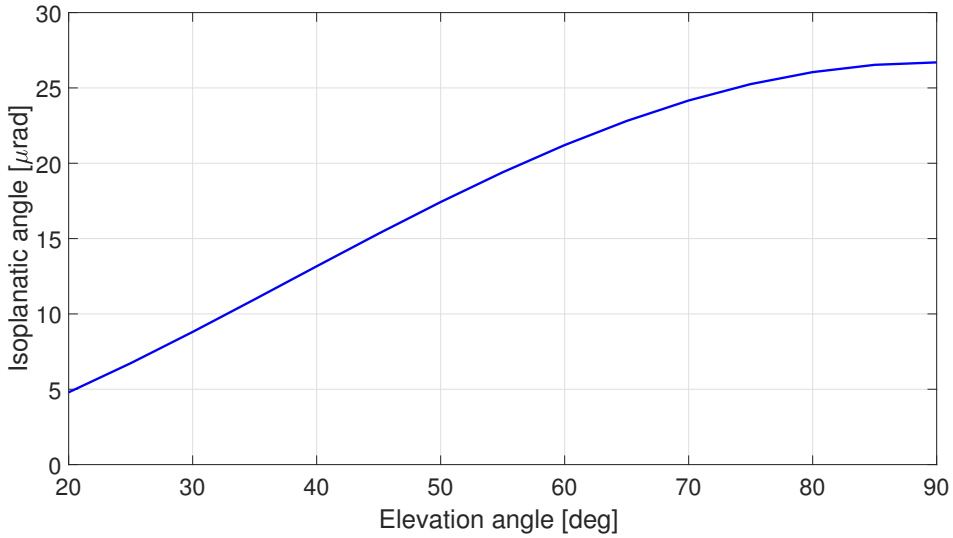

Figure 2.16.: Isoplanatic angle vs. elevation angle through the turbulent atmosphere

2.3.10. Point-ahead angle

Due to the orbital motion of the satellite with velocity V_{sat}, the downlink and uplink paths differ by an angle called the point-ahead angle θ_{PAA} which is given by

$$\theta_{\mathrm{PAA}} \cong \frac{2V_{\mathrm{sat}}}{c} \tag{2.24}$$

where c is the speed of light. As Fig. 2.17 shows that it takes a certain time to receive a beam from the satellite and then direct an uplink beam back to the satellite, which results in the point-ahead angle θ_{PAA}.

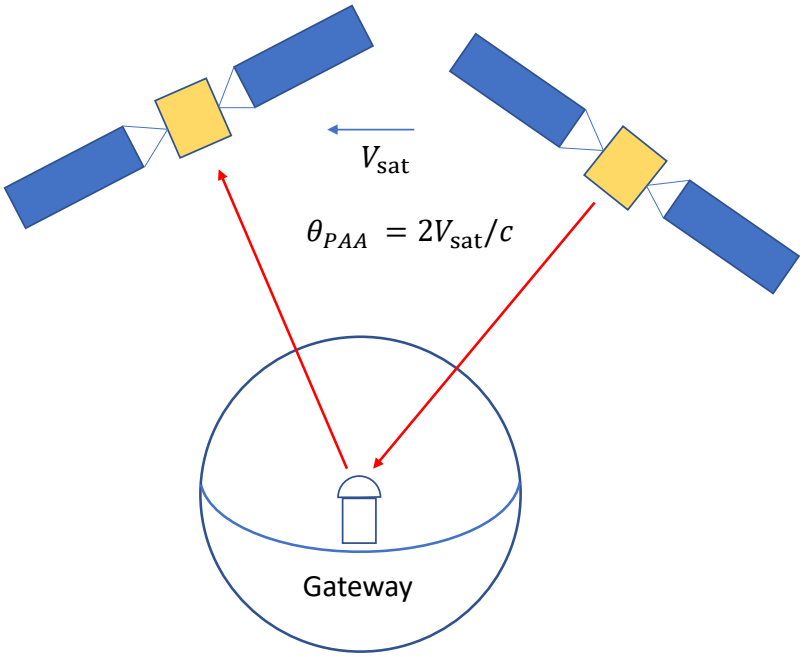

Figure 2.17.: A moving satellite resulting in a point-ahead angle due to the time difference between the downlink and the uplink beam [3]

The net centripetal force F_c acting upon the orbiting satellite with mass M_{sat} moving in a circular motion around the earth is given by

$$F_c = \frac{M_{sat} V_{sat}^2}{R_o} \tag{2.25}$$

where R_o is the orbit of the satellite. The net centripetal force results from the gravitational force F_g that pulls the satellite toward earth with mass M_e and is given by

$$F_g = \frac{G M_{sat} M_e}{R_o^2} \tag{2.26}$$

where G is the gravitational constant. For the satellite to stay in orbit, F_c has to be equal to F_g which, according to Eq. (2.25) and Eq. (2.26), results in

$$V_{sat} = \sqrt{\frac{G M_e}{R_o}}. \tag{2.27}$$

Using $G = 6.673 \cdot 10^{-11} \mathrm{N{\cdot}m^2/kg^2}$, $M_e = 6 \cdot 10^{24} \mathrm{kg}$, and $R_o = (6371 + 38500)\,\mathrm{km}$ in Eq. (2.27) gives V_{sat} of a GEO satellite as around 11000km/h. Plugging the value of V_{sat} in Eq. (2.24) gives $\theta_{PAA} = 19.9 \mu\mathrm{rad}$ which is large compared to the isoplanatic angle value till elevation

angle of 50 degrees as shown in Fig. 2.16. It will be explained in the later section the problem in pre-compensating the uplink beam when θ_{PAA} is greater than θ_0.

2.3.11. Phase piston

In addition to the phase wavefront distortions due to turbulence, signal phase variations exist along the propagation link path. These phase changes directly affect the phase of the signal. This slowly varying phase is called phase piston. The phase piston is crucial for coherent communications as the information is encoded into the optical carrier phase. The phase variations do not matter as far as incoherent communication is concerned. However, the phase piston becomes critical when the frequency separation between the neighboring signals is minimized to increase the spectral efficiency, as shown later in Chapter 6. The phase variations between the signals in the neighboring DWDM channels can lead to constructive and destructive interference. The one-dimensional temporal power spectrum for a single turbulence layer as given in Eq. (2.28), approximates the power spectral density given in [37].

$$L_{piston}(f) \approx \frac{0.055 \cdot (2\pi)^{-2/3} \cdot k^2 \cdot C_n^2 \cdot \Delta h \cdot V^{5/3} \cdot f^{-8/3}}{1 + 37.5 \cdot D^3 \cdot \left(\frac{f}{V}\right)^3} \tag{2.28}$$

where Δh is the thickness of the according turbulence layer and f is the modulus of the spatial frequency vector f, and D is the aperture diameter which is considered as a point receiver for the receiver at GEO satellite as explained in Section 2.3.7.

Eq. (2.28) yields a –8/3 power law for low frequencies and a –17/3 power law for high frequencies. The cut-off is found to be around $0.3^{V}/_{D}$ which is in agreement with [36]. It is helpful to convert this temporal spectral density in Eq. (2.28) into time series so it can be used in the simulations in Chapter **6.** Fig. 2.18 shows the time series where the variation of phase piston can be seen to fluctuate between -2π to 2π.

The normalized power spectral density obtained from Eq. (2.28) and the time series in Fig. 2.18 are plotted in Fig. 2.19 where the two approaches are shown to give the same results.

2.4. Fading mitigation technique

As described in the previous sections, deep fades are seen at the satellite receiver due to the scintillation and the beam wander, hence loss of signal availability. The OGS establishes bidirectional links with the GEO satellite by tracking the angle-of-arrival of the reference signal from the satellite, and use it to point the outgoing uplink beam which is offset by the point-ahead angle θ_{PAA}, the so-called pointing-by-tracking [4]. If both downlink and uplink beams travel through the same atmospheric region confined by the isoplanatic angle θ_0 then by tracking the wave-front distortions of the downlink signal, the effects of the atmosphere can be completely compensated by applying the inverse of these distortions to the uplink beam. But in

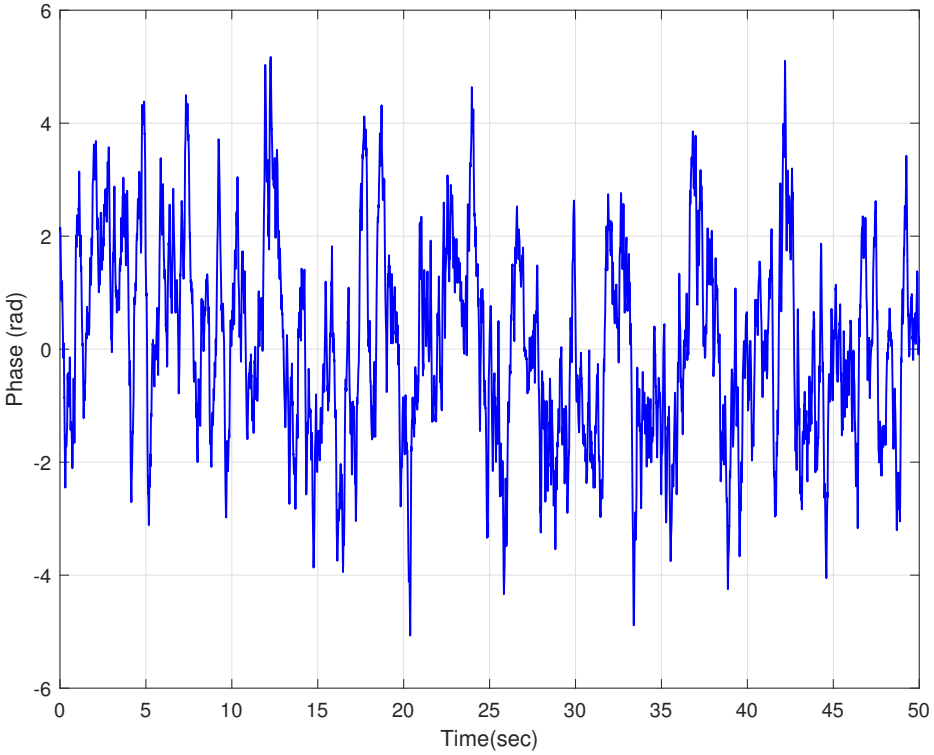

Figure 2.18.: Time series of the phase piston as obtained from Eq. (2.28)

reality, beam wander cannot be perfectly compensated because of the point ahead angle (PAA) being larger than the isoplanatic anglel (IPA) especially at lower elevation angles as shown in Fig. 2.16. Due to this reason, the uplink and downlink beams do not propagate through the same atmosphere restricting the ability to perform pre-compensation of the transmit beam at the OGS. Therefore, the residual pointing error is always present, which causes the fades at the satellite. Due to these realistic scenarios in the uplink, an untracked beam is considered for analysis in this thesis.

To achieve a stable signal over a long period of time, an effective and practical fading mitigation scheme in the uplink scenario has to be used. In this thesis, the application of OGEOFL is considered where the data-carrying optical signal propagates towards the GEO satellite in the uplink direction. Since a GEO satellite is located at around 38000km above earth and turbulence is significant in the first 20km, the size of the speckle with intensity and phase distortions is much larger than the receiver telescope, which is considered as a point receiver in comparison to the phase coherence diameter of a single speckle. In this situation, the receiver is not affected by phase distortions rather, it greatly suffers from intensity fluctuations. In this case, the favorable fading mitigation technique uses spatial diversity at the transmitter, which is the focus of this work.

The benefits of the transmitter diversity scheme are well studied [56, 57, 58] and experimentally proven in the optical satellite uplink, e.g., in semiconductor inter-satellite experi-

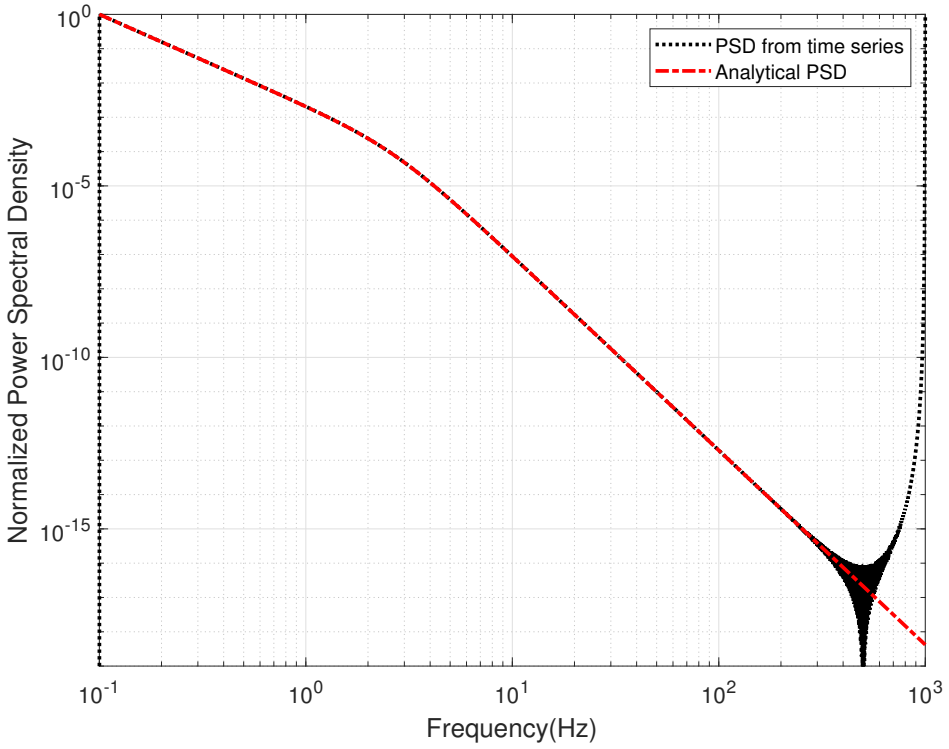

Figure 2.19.: Temporal power spectral density of the piston with V/D =9 Hz and cut-off frequency at $0.3V/D$

ment (SILEX) in which up to four uplink beams were transmitted from ESA's OGS to the GEO satellite ARTEMIS [59]. In another experiment in Japan, four uplink beams from the OGS of national institute of information and communications technology (NICT) were transmitted to optical inter-orbit communication engineering test satellite (OICETS) to reduce the optical signal's intensity fluctuation due to atmospheric turbulence[60]. The working principle of this scheme is that the multiple transmitters, which are spatially separated on the ground by more than the coherence length of the atmosphere, transmit the same copy of the data through uncorrelated atmospheric paths. The physical separation of the transmitters to less than 100 cm is sufficient to meet the requirement for the uncorrelated channels. The optical signals are then combined in one receiver at the satellite, where the duration and depth of the fades are reduced due to the favorable probability density function (PDF) obtained from the combination of all the transmitted beams. Fig. 2.20 shows a picture of this scenario where a diversity order of two is presented due to the use of two transmitters. It is also worth mentioning that the carrier separation Δf between the two transmitters should be sufficient to avoid interference between the neighboring signals. This requirement makes this scheme spectrally inefficient, though. A scheme using optical single side-band filtering to increase spectral efficiency is proposed in Chapter 6 of this thesis.

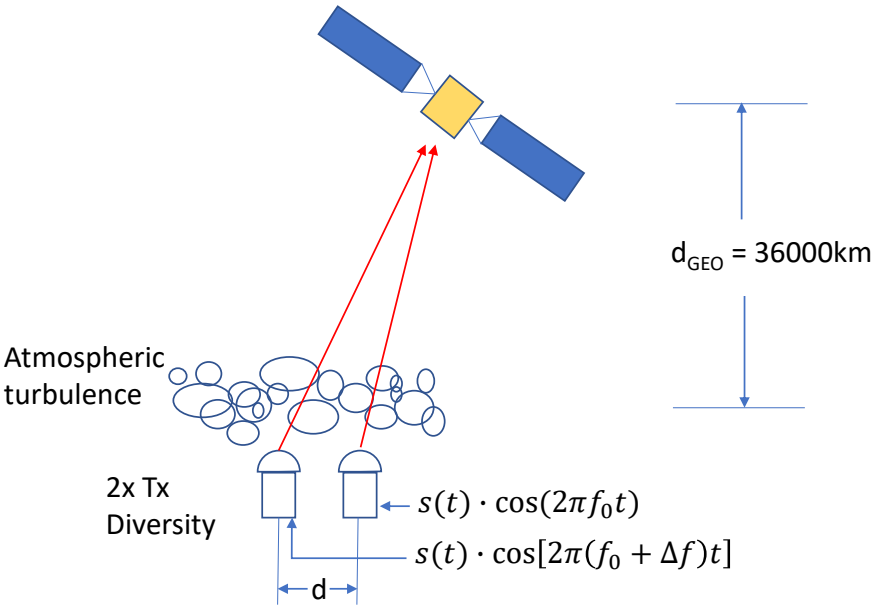

Figure 2.20.: Spatial diversity scheme with two transmitters on the ground from which the data propagates through the turbulent channels towards the GEO satellite

The benefit of transmitter diversity is demonstrated in the lab in DLR [61] using fading vectors generated using a FTB described in [62].

2.5. Optical communications system

2.5.1. Modulation

The transmission scheme used in this work is the intensity modulation and direct detection IM/DD. A Mach-Zehnder modulator (MZM) is used in an interferometric configuration to modulate the intensity of the carrier wave according to the modulating signal. The principle behind this type of modulation makes use of the linear electro-optic effect, which is the change of the refractive index of material with length L when an external electric field is applied across it. Due to the refractive index change, the phase of the carrier wave is changed according to

$$\varphi = \frac{2\pi n L}{\lambda}.$$

This variation of the phase change is used in the phase modulation schemes. However, when two phase modulators are used in an interferometer setup and appropriate bias voltage V_π is applied in one of the arms, then the result is the intensity modulation. The operating principle of an MZM modulator is shown in Fig. 2.21a where the input signal $E_{\text{in}} = A(t)\, e^{j\theta_{\text{in}}}$ is split into two equal parts. The two arms contain the nonlinear crystal, which is usually Lithium

Niobate ($LiNbO_3$), and a DC voltage is applied in one of the arms for biasing purposes. The voltages representing the data signal are applied to the two arms of the modulator in a push-pull manner meaning the complementary modulating signals are used here. This way, phase shifts of opposite signs are created in each arm. The voltage needed to induce a phase shift of π is known as the half-wave voltage V_π which is usually equal to 4 $V_{\text{p-p}}$ (Volts peak-to-peak) for the $(LiNbO_3)$ crystal. Applying a voltage V to the electrode of an electro-optic crystal will result in a voltage-induced phase shift of π. The voltage-induced phase shift $\varphi(t)$ can therefore be related to the applied voltage $V(t)$ according to

$$\varphi(t) = \pi \frac{V(t)}{V_\pi}.$$

The electrical field E_{out} at the ouput is written as a function of an input signal E_{in} as

$$E_{\text{out}}(t) = \begin{bmatrix} \frac{1}{\sqrt{2}} & \frac{1}{\sqrt{2}} \end{bmatrix} \cdot \begin{bmatrix} \exp(j(\varphi(t) + \varphi_{\text{bias}})) & 0 \\ 0 & \exp(j\varphi(t)) \end{bmatrix} \cdot \begin{bmatrix} \frac{1}{\sqrt{2}} \\ \frac{1}{\sqrt{2}} \end{bmatrix} \cdot E_{\text{in}}(t). \quad (2.29)$$

In Eq. (2.29), each of the terms from right to left has the following meaning: $E_{\text{in}}(t)$ is the input signal, the next term is the 1:2 combiner, the following term represents the phase shift induced onto the two signals on the arms, the last term is the 2:1 splitter. From Eq. (2.29), the amplitude transfer function T of the modulator is written as

$$T = \frac{E_{\text{out}}}{E_{\text{in}}}$$

$$T(t) = \frac{1}{2}\left[\exp(j(\varphi_1(t) + \varphi_{\text{bias}})) + \exp j\varphi_2(t)\right].$$

Rearranging the terms gives

$$T = \exp\left(j\frac{\varphi_1(t) + \varphi_2(t)}{2} + j\frac{\varphi_{\text{bias}}}{2}\right) \cdot \cos\left(\frac{\varphi_1(t) - \varphi_2(t)}{2} + \frac{\varphi_{\text{bias}}}{2}\right). \quad (2.30)$$

Eq. (2.30) shows that there is usually both phase modulation (from the first term) and amplitude modulation (from the second term) passed on to a signal when going through a Lithium Niobate modulator. In a push-pull operation mode, $\varphi_1(t) = -\varphi_2(t)$ which results in a pure amplitude modulation. If the MZM is operated around the quadrature point, then the transfer function in Eq. (2.30) is linear in the intensity for small $\Delta\varphi$ which results in

$$|T|^2 = A^2\frac{1}{2}\cos^2\left(\frac{\Delta\varphi}{2}\right) = A^2\frac{1}{2}(1 + \cos(\Delta\varphi)).$$

The transfer function of the modulator is shown in Fig. 2.21b where the push-pull operation mode is shown.

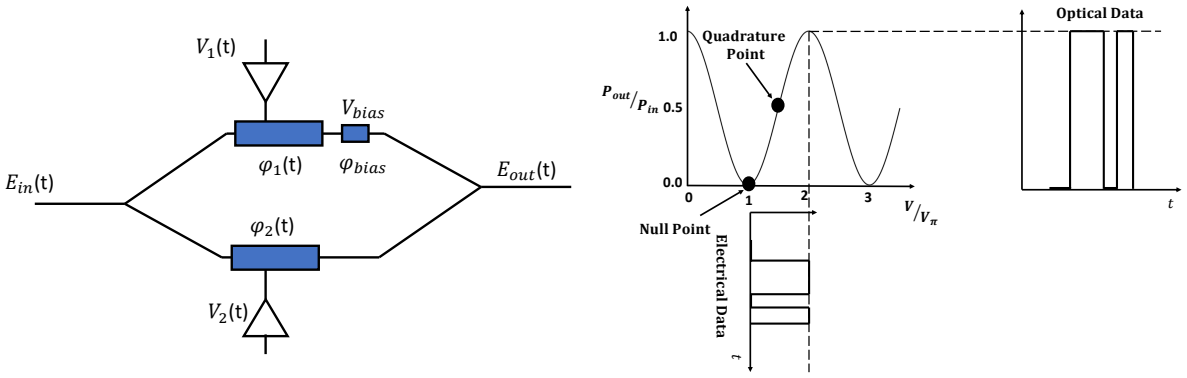

(a) Operation principle of a $LiNbO_3$ modulator

(b) Intensity transfer function of an MZM when operated in push-pull mode

Figure 2.21.: Operation principle and intensity transfer function of an MZI [5]

2.5.2. Demodulation

For the demodulation of the received signal, a direct detection scheme is used, which is based on the detection of the received signal intensity. The choice of the type of photodetector depends on whether the receiver has an optical preamplifier before the optical-to-electrical conversion process. As shown in Fig. 2.22, a PIN type receiver is used for a preamplified system, while an APD is suitable if no preamplifier is present. After the received signal with electrical field $E_s(t)$ is converted into current $I(t)$, the transimpedance amplifier TIA converts this current into voltage for the analog-to-digital converter (ADC) which samples the continuous signal $V(t)$ into discrete signal $V(n)$ according to the sample rate. Lastly, digital signal processing (DSP) is performed to recover the clock from the received signal, equalization is applied to improve the signal-to-noise ratio (SNR) and finally BER calculation is done by comparing the decoded signal with the known transmitted pseudo-random binary sequence (PRBS) sequence.

Figure 2.22.: Block diagram of the direct detection receiver chain

A common performance parameter for the quality of digital communications system is the BER, which is the ratio of erroneous bits to the total received bits. Usually, a BER of 10^{-9} can be considered error-free which indicates the presence of one error bit in one billion received bits. It is difficult to measure an even lower BER due to the long integration times, during

which the received signal may not be reliably detected because the temperature-dependent variations may alter system characteristics [34]. In this thesis, a direct detection scheme called non-return-to-zero on-off keying (NRZ-OOK) is considered, which means the photodetector will detect the optical power in the given bit period when the digital one is received. No power will be detected when the digital zero is received due to the absence of light. Fig. 2.23 shows the corresponding PDFs of received ones and zeros, assuming receiver noise follows additive white Gaussian noise (AWGN) distribution. The threshold V_t defines the boundary between the detected one and zero. All the sampled values above V_t are declared as received ones and the samples below V_t are declared as zeros. The mean values of the ones and zeros are represented as V_1 and V_0, respectively.

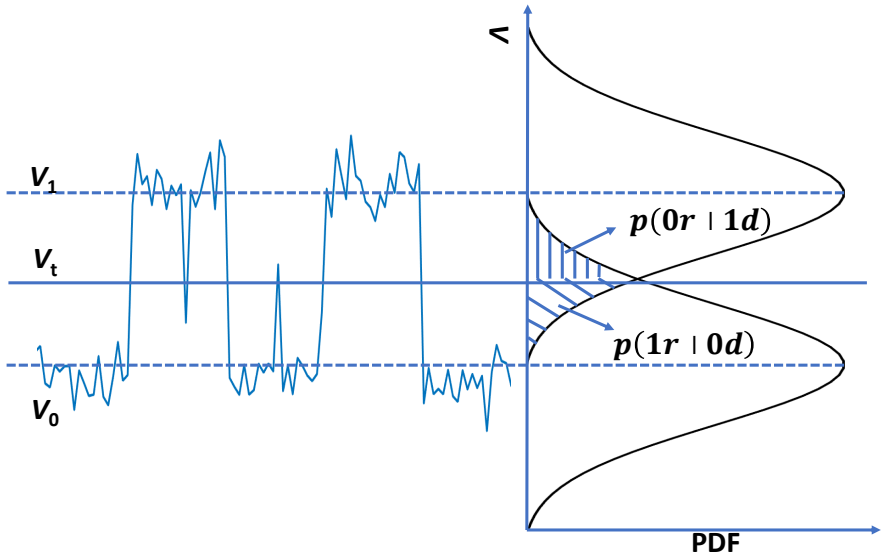

Figure 2.23.: Time domain electrical signal after the receiver and the probability distribution functions corresponding to the detected ones and zeros assuming AWGN distribution in electric domain [5]

The probabilities of received ones and zeros are given as $p(1\mathrm{r})$ and $p(0\mathrm{r})$, respectively whereas $p(1\mathrm{r} \mid 0\mathrm{d})$ is the probability of deciding 0 when 1 is received, also called missed detection and $p(0\mathrm{r} \mid 1\mathrm{d})$ is the probability of deciding 1 when 0 is received, also called false alarm. The BER can be written as [5]

$$\mathrm{BER} = p(1\mathrm{r})\, p(1\mathrm{r} \mid 0\mathrm{d}) + p(0\mathrm{r})\, p(0\mathrm{r} \mid 1\mathrm{d}). \tag{2.31}$$

The assumption of equal probability of occurrence of ones and zeros leads to $p(1\mathrm{r}) = p(0\mathrm{r}) = 1/2$ which gives

$$\mathrm{BER} = \frac{1}{2}\left[p(1\mathrm{r} \mid 0\mathrm{d}) + p(0\mathrm{r} \mid 1\mathrm{d})\right].$$

The conditional probabilities of missed detection and false alarm with variances σ_1^2 and σ_0^2 are defined as

$$p\left(1\mathrm{r} \mid 0\mathrm{d}\right) = \frac{1}{\sigma_1\sqrt{2\pi}} \int_{-\infty}^{V_\mathrm{t}} \exp\left(-\frac{\left(V-V_1\right)^2}{2\sigma_1^2}\right) dV = \frac{1}{2}\mathrm{erfc}\left(\frac{V_1-V_\mathrm{t}}{\sigma_1\sqrt{2}}\right)$$

$$p\left(0\mathrm{r} \mid 1\mathrm{d}\right) = \frac{1}{\sigma_0\sqrt{2\pi}} \int_{V_\mathrm{t}}^{\infty} \exp\left(-\frac{\left(V-V_0\right)^2}{2\sigma_0^2}\right) dV = \frac{1}{2}\mathrm{erfc}\left(\frac{V_\mathrm{t}-V_0}{\sigma_0\sqrt{2}}\right)$$

where $\mathrm{erfc}(x)$ stands for complementary error function and is mathematically given as [63]

$$\mathrm{erfc}\left(x\right) = \frac{2}{\sqrt{\pi}} \int_x^{\infty} \exp\left(-y^2\right) dy.$$

Eq. (2.31) can now be parameterized as

$$\mathrm{BER} = \frac{1}{4}\left[\mathrm{erfc}\left(\frac{V_1-V_\mathrm{t}}{\sigma_1\sqrt{2}}\right) + \mathrm{erfc}\left(\frac{V_\mathrm{t}-V_0}{\sigma_0\sqrt{2}}\right)\right]. \tag{2.32}$$

Eq. (2.32) shows that the BER is dependent on the decision threshold V_t. To get the best performance i.e., minimum BER, V_t is optimized as

$$\frac{\left(V_\mathrm{t}-V_0\right)^2}{2\sigma_0^2} = \frac{\left(V_1-V_\mathrm{t}\right)^2}{2\sigma_1^2} + \ln\left(\frac{\sigma_1}{\sigma_0}\right).$$

The last term is usually negligible so V_t can be obtained from

$$\frac{\left(V_\mathrm{t}-V_0\right)}{\sigma_0} = \frac{V_1-V_\mathrm{t}}{\sigma_1} \equiv Q. \tag{2.33}$$

The exact expression of V_t is given as

$$V_\mathrm{t} = \frac{\sigma_0 V_1 + \sigma_1 V_0}{\sigma_0 + \sigma_1}. \tag{2.34}$$

In the case of $\sigma_0 = \sigma_1$, V_t= $\left(V_1+V_0\right)/2$ which means setting the decision threshold in the middle of the bit. This is applicable to PIN receivers where the dominant noise is thermal noise instead of shot noise, and it is independent of the average current obtained during the photodetection process. Additionally, shot noise is greater for bit one because it varies linearly with the average current compared to bit zero. For avalanche photodiode (APD) type receivers, V_t should be selected according to Eq. (2.34). In the experiment described in Chapter 5, a PIN receiver is used, allowing the use of setting the threshold in the middle of the bit for the BER calculation.

Nevertheless, for the sake of generalization, the BER for the optimum V_t can be obtained using Eq. (2.32) and Eq. (2.33) leaving Eq. (2.31) as a function of Q only

$$\text{BER} = \frac{1}{2}\text{erfc}\left(\frac{Q}{\sqrt{2}}\right). \tag{2.35}$$

The parameter Q is derived from Eq. (2.33) and Eq. (2.34) and is given as

$$Q = \frac{V_1 - V_0}{\sigma_1 + \sigma_0}.$$

Fig. 2.24 shows a Q value of 6 is required to get BER of 10^{-9} as an error-free reception.

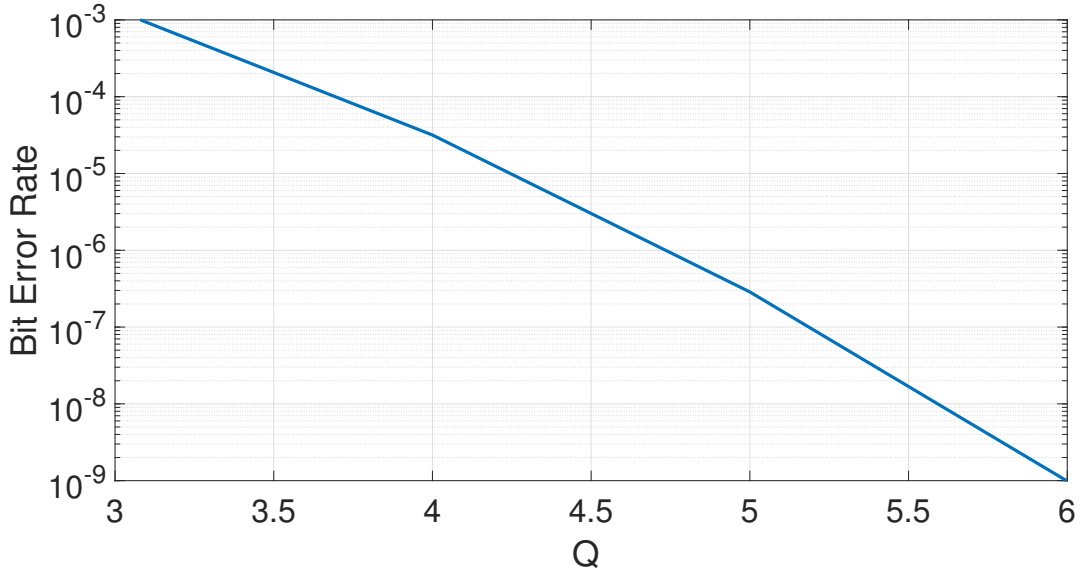

Figure 2.24.: Bit error rate vs. Q parameter for the NRZ-OOK system with direct detection

Sometimes, the performance of the communications system is measured in SNR for practical reasons. For thermal-noise limited receiver using PIN, $Q = \sqrt{\text{SNR}}/2$ which requires SNR = 21.6dB for BER = 10^{-9}. Eq. (2.35) can be written in terms of SNR as

$$\text{BER}_{\text{thr}} = \frac{1}{2}\text{erfc}\left(\frac{1}{2}\sqrt{\frac{\text{SNR}}{2}}\right).$$

For the case of a shot-noise limited receiver like an APD, $Q = \sqrt{\text{SNR}}$ which translates Eq. (2.35) to

$$\text{BER}_{\text{sn}} = \frac{1}{2}\text{erfc}\left(\sqrt{\frac{\text{SNR}}{2}}\right). \tag{2.36}$$

A shot-noise limited receiver requires an SNR of 15.6dB for BER = 10^{-9} .

2.5.3. Measurement of the receiver sensitivity

Receiver sensitivity is another measure to evaluate the performance of the digital communications system. It is defined as the minimum power required by the receiver to achieve the desired BER for the error correction scheme to work. A most common method of calculating BER is to count error bits N_e in the total number of received bits N_{Rx} which can be written as

$$\mathrm{BER} = \frac{N_e}{N_{Rx}}.$$

The Shannon-Hartley theorem states that the channel capacity limit R_b in b/s with a specified bandwidth B in Hz and in the presence of noise N is given as [64]

$$R_b = B\log_2(1+\mathrm{SNR})$$

where SNR denotes signal-to-noise ratio in dB.

The average energy per bit E_b in the absence of an optical amplifier can be calculated from the mean signal power P_s as $E_b = \frac{P_s}{R_b}$. If an optical preamplifier such as an EDFA is used before the photodiode then E_b increases by a factor equal to the gain G of the amplifier and is given as [65]

$$E_b = \frac{GP_s}{R_b}. \tag{2.37}$$

Another performance parameter called energy per bit over the noise spectral density $\frac{E_b}{N_0}$ is used in the communication systems. According to [66, 67], the noise spectral density N_{ASE} of an optically preamplified receiver is given by

$$N_{ASE} = n_{sp}(G-1)\frac{hc}{\lambda} \tag{2.38}$$

where h is the Planck's constant, and n_{sp} is the inversion factor of the amplifier which is 1 for an ideal noiseless amplifier which results in a noise figure F value of 3dB due to the relation $F = 2n_{sp}$ [68]. Combining Eq. (2.37) and 2.38 results in

$$\frac{E_b}{N_0} = \frac{GP_s}{R_b n_{sp}(G-1)}\frac{\lambda}{hc} = \frac{GN_p hc/\lambda}{n_{sp}(G-1)hc/\lambda} \tag{2.39}$$

where N_p is the number of photons per bit and $N_{ASE} = N_0$. Considering shot-noise limit case, $n_{sp} = 1$ and a large amplifier gain G, $\frac{E_b}{N_0}$ in Eq. (2.39) becomes equal to N_p [66].

The performance of the optical communication systems can also be evaluated in terms of optical signal-to-noise ratio (OSNR). It can be measured by the optical spectrum analyzer before the photodetection process. The OSNR is defined as [65]

$$\mathrm{OSNR} = \frac{GP_\mathrm{s}}{2N_\mathrm{ASE}B_\mathrm{ref}} = \frac{R_\mathrm{b}}{2B_\mathrm{ref}}\frac{E_\mathrm{b}}{N_0} \tag{2.40}$$

where $B_\mathrm{ref} = {}^{c}/\lambda_\mathrm{c}^2 \cdot 0.1\mathrm{nm}$ is commonly defined as the reference bandwidth.

It can be seen from Eq. (2.40) that OSNR is dependent on the data rate. However, a figure of merit dependent on the data rate is not suitable for comparing receiver sensitivities because all systems have to operate at the same data rate to evaluate the best candidate. Therefore, SNR is a better figure of merit since both signal and noise power are measured in the same bandwidth. Replacing the average noise power $P_\mathrm{n} = N_\mathrm{ASE}B$, number of bits in a symbol n_s , and signal to noise ratio per symbol R_s in Eq. (2.39) results in

$$\frac{E_\mathrm{b}}{N_0} = \mathrm{SNR_b} = \frac{\mathrm{SNR_s}}{n_\mathrm{s}} = \frac{GP_\mathrm{s}B}{P_\mathrm{n}Bn_\mathrm{s}}. \tag{2.41}$$

For the NRZ-OOK system, $n_\mathrm{s} = n_\mathrm{b}$ since one bit is encoded in a symbol. Eq. (2.41) is applicable to an ideal amplifier with high gain and $n_\mathrm{sp} = 1$ as explained above. In the case of shot-noise limit, N_p required to achieve the desired BER is given as

$$N_\mathrm{p} = \frac{1}{N_0}\frac{GP_\mathrm{s}}{R_\mathrm{b}} = \frac{\lambda}{hc}\frac{P_\mathrm{s}}{R_b n_\mathrm{b}}. \tag{2.42}$$

Additionally, N_p can also be calculated from the measured OSNR as given in Eq. (2.40) provided the measurement bandwidth is set equal to the signal bandwidth i.e., $B_\mathrm{ref} = B$ which results in

$$N_\mathrm{p} = \frac{2B}{R_\mathrm{b}n_\mathrm{b}}\mathrm{OSNR}.$$

2.5.4. Signal-to-Noise ratio in a photoreceiver

Signal-to-noise ratio is affected by several noise sources associated with the photodetection process those inherent to the receiver itself. The SNR is given as [69]

$$\mathrm{SNR} = \frac{I_\mathrm{s}^2}{\sigma_\mathrm{s}^2 + \sigma_\mathrm{B}^2 + \sigma_\mathrm{D}^2 + \sigma_\mathrm{T}^2} \tag{2.43}$$

where I_s is the DC current obtained from the receiver optical power, σ_s^2 is the shot noise associated with the received optical signal, which follows Poisson distribution and behaves more like Gaussian for a high number of received photons, σ_B^2 is the background optical noise, σ_D^2 is the dark current noise which is present even if there is no optical signal incident on the active area of the diode, and σ_T^2 is the thermal noise associated with the receiver section which converts current to voltage. It is enhanced by the post electronic amplifier, which is also called

TIA whose job is to raise the voltage to the suitable levels for the subsequent system, e.g., ADC. The photocurrent for an APD is given as

$$I_{\mathrm{s}} = \eta q M P_{\mathrm{s}} \frac{\lambda}{h\mathrm{c}}$$

where η is the quantum efficiency, q is the elementary charge of an electron, and M is the multiplication factor or the intrinsic gain obtained due to the impact ionization process in the APD. The photocurrent can also be represented as

$$I_{\mathrm{s}} = R P_{\mathrm{s}}$$

where R is the responsivity given in A/W quantifying the number of photons that are converted into electronic current and is represented as

$$R = \eta q M \frac{\lambda}{h\mathrm{c}}.$$

The optical to electrical conversion by the photodiode is a nonlinear process and mathematically given by $I = R \mid E^2 \mid$, where E is the electric field of the optical wave.

2.5.5. Noise sources

The shot noise σ_{s}^2 in an APD is given by

$$\sigma_{\mathrm{s}}^2 = 2qI_{\mathrm{s}}M^2F_{\mathrm{A}}B_e = 2qRP_{\mathrm{s}}M^2F_{\mathrm{A}}B_e \tag{2.44}$$

where B_{e} is the bandwidth over which the noise is measured, and F_{A} is the excess noise factor given by

$$F_{\mathrm{A}} = k_{\mathrm{c}}M + (1 - k_{\mathrm{c}})\left(2 - \frac{1}{M}\right)$$

where k_{c} is the carrier ionization ratio. The background noise σ_{B}^2 is given by

$$\sigma_{\mathrm{B}}^2 = 2qI_{\mathrm{B}}M^2F_{\mathrm{A}}B = 2qRP_{\mathrm{B}}M^2F_{\mathrm{A}}B_e.$$

The dark current σ_{D}^2 in the absence of light is given as

$$\sigma_{\mathrm{D}}^2 = 2qI_{\mathrm{D}}M^2F_{\mathrm{A}}B_e.$$

The thermal noise σ_{T}^2 associated with every photoreceiver is given as

$$\sigma_{\mathrm{T}}^2 = \frac{4k_{\mathrm{B}}TB}{R_{\mathrm{L}}} \tag{2.45}$$

where k_{B} is the Boltzmann constant $\left(1.38 \cdot 10^{-23}\mathrm{Joules/K}\right)$, T is the absolute temperature in Kelvin, and R_{L} is the resistor value of the photoreceiver's circuit. As presented in Section 2.5, the noise variance in the absence of light when digital zero is transmitted is given as

$$\sigma_0^2 = \sigma_{\mathrm{T}}^2 + \sigma_{\mathrm{D}}^2 + \sigma_{\mathrm{B}}^2$$

and the total noise variance associated with digital one σ_{I}^2 in the presence of light is given as

$$\sigma_{\mathrm{I}}^2 = \sigma_s^2 + \sigma_0^2.$$

Usually, in the datasheets, the noise equivalent power (NEP) value is given, which is a characteristic noise figure of a photoreceiver. It is defined as the minimum optical power that a photoreceiver can detect to give SNR=1. The NEP is influenced mainly by the dark current noise and thermal noise and is represented for a 1 Hz bandwidth. It is normalized with respect to the bandwidth B, which varies according to the speed of the receiver. The NEP of a photoreceiver in $\mathrm{W}/\sqrt{\mathrm{Hz}}$ is given by

$$\mathrm{NEP} = \frac{P_{\mathrm{s}}}{\sqrt{B}} = \frac{1}{R}\sqrt{\frac{1}{B}\left(\sigma_{\mathrm{D}}^2 + \sigma_{\mathrm{T}}^2\right)}.$$

Since NEP includes the contribution from all noise sources inherent to a receiver, Eq. (2.43) can be written in terms of signal and background noise powers as

$$\mathrm{SNR} = \frac{I_{\mathrm{s}}^2}{\sigma_{\mathrm{s}}^2 + \sigma_{\mathrm{B}}^2 + R^2\mathrm{NEP}^2B}.$$

For the case of a thermal-noise limited receiver which is usually the case with direct detection, Eq. (2.43) reduces to

$$\mathrm{SNR}_{\mathrm{T}} = \frac{R_{\mathrm{L}}\left(MRP_{\mathrm{s}}\right)^2}{4k_{\mathrm{B}}TF_{\mathrm{A}}B}.$$

For the case of shot noise-noise limited receiver, $\sigma_{\mathrm{s}}^2 \gg \sigma_{\mathrm{T}}^2$ which occurs for an optically preamplified receiver or a coherent system, SNR can be written as

$$\mathrm{SNR}_{\mathrm{s}} = \frac{RP_{\mathrm{s}}}{2qB} = \frac{\eta P_{\mathrm{s}}}{2F_{\mathrm{A}}B}\frac{\lambda}{hc}.$$

Note, for a PIN receiver, F_{A} and M are equal to 1, which simplify all the above equations accordingly.

2.5.6. Symbol timing recovery

In real communication systems, there is a mismatch between the oscillator generating the signal and the freely running oscillator of an ADC on the receiver side. This results in variations in the symbol timing, making it difficult to decode the signal properly. These variations arise due to the thermal drift and the noise present in the oscillators, which are seen as the timing jitter and slowly varying timing drift in the received signal. The result is that sampling is not done at the optimum points in the signal, i.e., the downsampled samples are not taken from the center of the symbol, which severely degrades the decoding process and results in poor BER performance. The symbol timing recovery algorithm determines and corrects the timing offset. The offset is described as a slowly-varying phase term present in the received signal. In this thesis work, a feedforward timing error method is used to estimate the timing error section-by-section from the received signal. Using this method, the signal is downsampled at the center of the bit resulting in an enhanced BER performance. In this work, a feedforward algorithm by Oerder and Meyr is used [6], which is graphically represented in Fig. 2.25.

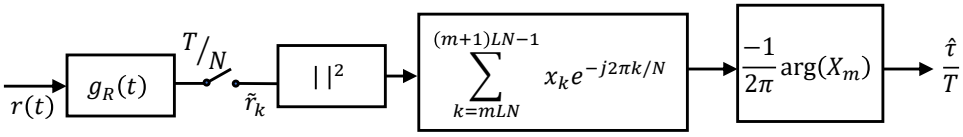

Figure 2.25.: Block diagram of the square estimator using feedforward timing recovery method [6]

The analog received signal $r(t)$ is filtered by a lowpass filter with an impulse response $g_R(t)$. After that, the signal is sampled at a rate of T/N to obtain the digital signal $\tilde{r}_k$. The digitized signal is divided into block length of LN samples where L is the number of symbols and N is the number of samples per symbol given by the oversampling factor. Each block length is squared, and then the complex Fourier coefficients of the resultant signal are computed at the symbol rate $1/T$. The estimated symbol timing error $\hat{\tau}$ is given as

$$\frac{\hat{\tau}}{T} = -\frac{1}{2\pi}\arg\left(\sum_{k=mLN}^{(m+1)LN-1}\left|r\left(\frac{kT}{N}\right)\right|^2 e^{-j2k\pi/N}\right) \tag{2.46}$$

where $\frac{\hat{\tau}}{T}$ is the constant timing error in a frame which is L symbols long. A variant of Oerder and Meyr algorithm is proposed by Lee [70], which requires only 2 samples per symbol instead of 4 required by Oerder and Meyr algorithm, the later can limit the user data rate or require more memory if the data rate cannot be reduced. The modified form to calculate the timing error is given as

$$\frac{\hat{\tau}}{T} = -\frac{1}{2\pi}\arg\left(\sum_{k=1}^{LN-1}\left(\left|r\left(\frac{kT}{N}\right)\right|^2 e^{-2jk\pi/N} + \mathrm{Re}\left\{r\left(\frac{kT}{N}\right)r^*\frac{(k-1)T}{N}\right\}e^{-j2(k-0.5)\pi/N}\right)\right). \tag{2.47}$$

In this thesis work both Eq. (2.46) and Eq. (2.47) are implemented for clock recovery, and both are found to give similar results in terms of BER performance.

2.5.7. Equalization

Distortions can become significant for a high-speed signal propagating through long traces of a circuit board. The result is the attenuation of the high-frequency components leading to the loss of information. Equalization is a technique to compensate for the degrading effects of the transmission paths. The equalization technique implemented in this thesis is called the linear feedforward equalizer (LFE) because it is linear and it only uses information from previously received bits, i.e., it feeds forward information from previous to next bits. A graphical representation of the working principle of this type of equalizer is shown in Fig. 2.26 where $r(n)$ is the voltage level of the center of the bit under consideration, $r(n-1)$ is the voltage level of the last bit, $r(n-2)$ is the voltage level of the bit before the last bit, and so on.

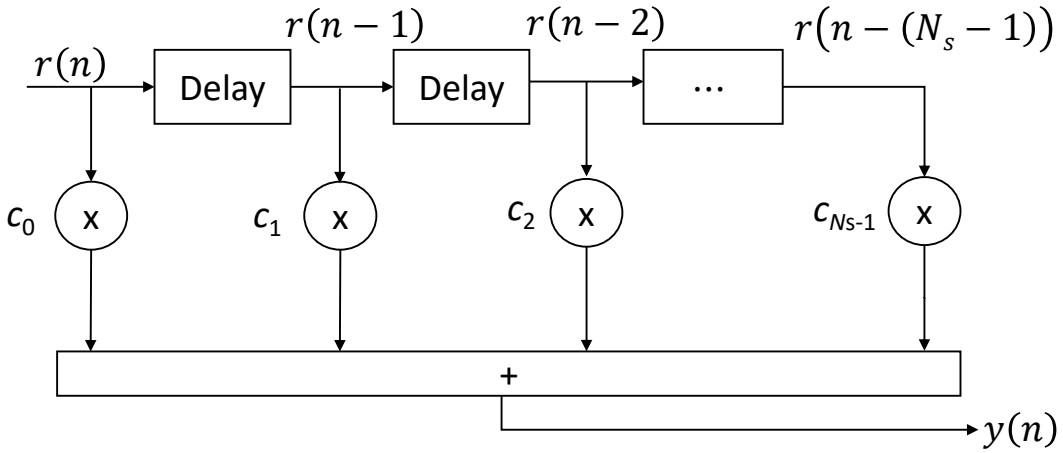

Figure 2.26.: Block diagram of a shift register description of an LFE [7]

The voltage level of each bit is multiplied by a "tap" which is unique to each bit. The sum of the products of the voltages and taps gives the equalized voltage level $y(n)$, which is mathematically shown in Eq. (2.48).

$$y(n) = \sum_{k=0}^{N_s-1} c_k r(n-k) \tag{2.48}$$

where N_s is the number of taps and c_k are the taps that need to be optimized to interpret the bits accurately. A method to optimize the taps is called least mean square (LMS) algorithm, which is given by

$$c_{\text{new}} = c_{\text{current}} + \mu \cdot r \cdot e^*$$

where μ is the step size to converge the algorithm and e is the error signal given by $e = d - y$ taking d as the reference signal. Equalization was performed on the 32Gb/s back-to-back measured signal, which can be seen in Fig. 5.3. The curve matches quite closely with the unequalized case. It can be concluded that the distortion effects due to long traces of the circuit were negligible in the experimental setup. Therefore, equalization was not performed for the processing of the other signals to save computational time.

3. Laboratory implementation of a 10Gb/s per channel optical transmitter diversity scheme

In this Chapter, a lab experiment performed at the German Aerospace Center's Institute of Communications and Navigation to demonstrate the benefit of the transmitter diversity as a fading mitigation scheme is presented. In this experiment, the implementation of transmitter diversity using one digital data signal with data rate R_b= 10Gb/s and a wavelength division scheme with two distinct wavelengths in an OGEOFL channel are presented. Here, the transmitter diversity scheme is demonstrated with a channel separation according to the ITU-T DWDM frequency grid [71]. The channel spacing between the two optical signals is set to 50 GHz because of the optical transmitters used in the experiment. The allowed channel frequencies in THz according to the ITU-T standard are defined by

$$f_c(n) = 193.1\,\text{THz} + n \cdot 0.05\,\text{THz} \tag{3.1}$$

where n is a positive or negative integer including 0. Other fixed channel spacings with a step size of 200 GHz, 100 GHz, 25 GHz, and 12.5 GHz are possible too. Using these grids and according to Eq. (3.1), a total optical bandwidth of around 11 THz is achieved which covers the complete C- and L- band ranging from 1529 nm to 1610 nm. This coincides with the operating wavelength range of the standard off-the-shelf optical amplifiers, i.e., EDFA which are commonly used in the fiber optical communication systems. This available technology is used to achieve the goal of reaching Tb/s throughput in the OGEOFL scenario.

A minimum frequency separation between the channels is required to avoid spectral interference between the two signals. This is achieved by keeping the optical spectra separated enough in frequency to prevent overlapping. In an ideal case, constructive interference occurs when the carrier frequency and phase between the two optical signals are exactly the same. However, in reality, there is always a slight mismatch between the carriers, called frequency offset, even when they are set at the same frequency. It is mainly due to the production tolerances and carrier frequency instabilities due to temperature drifts. This leads to interference shown in Fig. 3.1a where the two spectra are set at the same frequency but looking at the time domain signal on the right side, it is clear that the constructive interference does not happen, resulting in the loss of the signal quality. To avoid this interference problem, a frequency separation of 50 GHz between the two carriers is set as shown in Fig. 3.1b, which is sufficient for a 10Gb/s signal. It can also be seen in the plot on the right-hand side that the time domain signal exhibits constructive interference between the two signals, which is seen as a good representa-

tion of a PRBS7 signal as compared to the signal in Fig. 3.1a. It is to be noted that the carrier separation must be adjusted according to the data rate as the signal bandwidth increases.

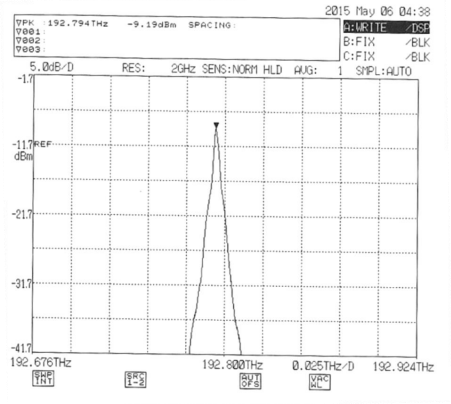

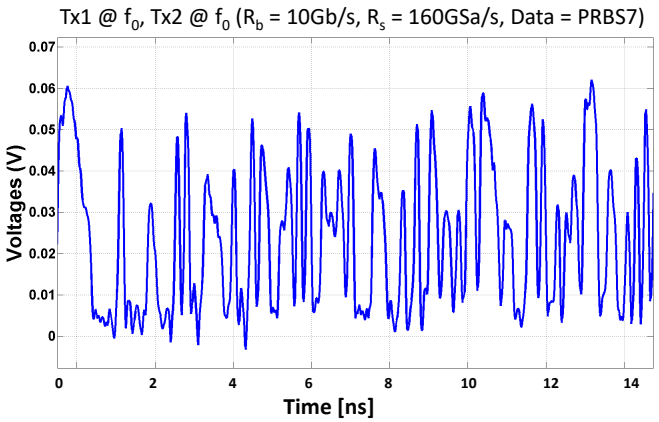

(a) Carrier separation between the signals is set to zero. Left plot shows the overlapping spectra between the two signals, and on the right, the resulting distorted signal due to the interference is shown

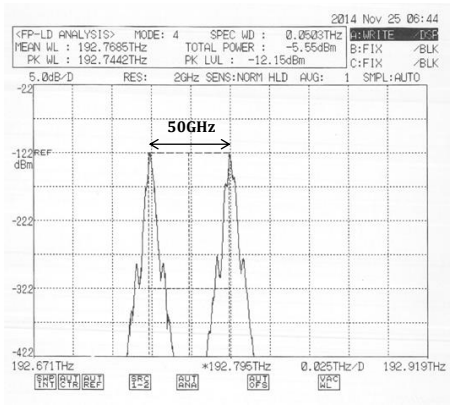

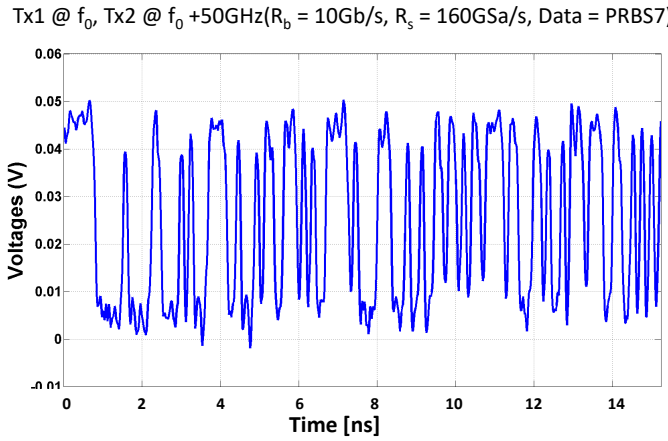

(b) Carrier separation between the signals is set to 50 GHz. Left plot shows the distinct spectra between the two signals, and on the right, the resulting undistorted signal is shown

Figure 3.1.: Influence of frequency separation between the neighbouring signals on the signal quality

3.1. Experimental setup

Fig. 3.2 describes the setup of a typical transmitter diversity scheme. The same 10Gb/s modulating data signal feeds the two optical transmitters. These two signals separately go through the uncorrelated fading testbeds FTBs, which emulate the effect of atmospheric turbulence on the optical signal. Finally, the two signals are combined at the 10Gb/s direct detection receiver, where a more stable signal is achieved. Moreover, it reduces the depth and outage

probability of the fades as verified by the transmission diversity experiment ArtemEx on the ARTEMIS GEO satellite [4]. To demonstrate the concept, an IM/DD scheme is deployed in this experiment due to its simplicity and ease of implementation.

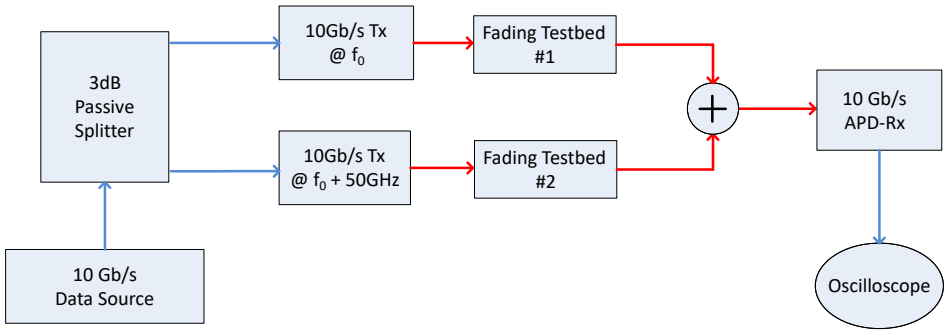

Figure 3.2.: Block diagram of the transmitter diversity scheme using one 10Gb/s data channel and two wavelengths with 50 GHz frequency separation

A 10Gb/s pattern generator with PRBS7 test sequence is used as the data source. A 3 dB power splitter splits the 10Gb/s data signal into two to drive the two optical transmitters. The optical transmitters in use are the commercially available tunable XFP transceivers, which can be tuned on ITU-T 50 GHz grid. The minimum frequency separation of 50 GHz between the two transmitters is limited by the tunable XFP transceiver modules. The 10Gb/s modulated optical signals with 1 mW power each are fed into the two FTBs. The FTBs are in-house built statistically independent fading emulators that can emulate the scintillation effects of the turbulent atmosphere [62]. Fig. 3.3 shows the block diagram representing the working principle of the FTB. The testbed uses an input file having a normalized vector which can be either taken from measured satellite uplink fading vector or any other additional user-defined realistic fading behavior. The output is the regenerated fading vector with a user-defined mean power which follows the power statistics of the loaded fading vector. Fading vectors used in this experiment are obtained from the ArtemEx measurement campaign which was carried out for the uplink GEO feeder link. The sampling rate of the fading vector is 8kSa/s. Both FTBs are loaded with the same fading vector as shown in Fig. 2.10 but with a random non-zero time delay to make the output from the two testbeds completely uncorrelated as it is in the outdoor environment. The two optical signals experience the scintillation effects in the testbed. Direct detection of the optical signals is done by the photoreceiver, which converts the optical signals into the baseband 10Gb/s signal. As an example, a commercial APD with a -3 dB bandwidth of 8 GHz [72] can be used as an energy detector where the two optical signals separated by 50 GHz are implicitly combined. The responsivity of this APD is $0.85\,\mathrm{A/W}$ at 1550 nm.

Fig. 3.4 shows the picture of the experimental setup of the two-fold transmitter diversity setup in the optical communications lab of DLR. The 10Gb/s PRBS7 data signal is generated with the pulse pattern generator, and the laser carrier is modulated with the off-the-shelf tunable XFP transceivers whose frequencies are set apart by 50 GHz to avoid interference. For high-speed communications, i.e., 10 Gb/s and beyond, it becomes difficult to modulate the laser

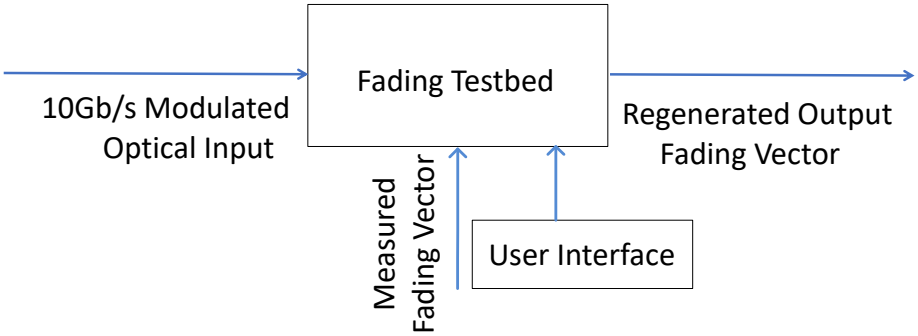

Figure 3.3.: Block diagram of the Fading Testbed

directly. Additionally frequency chirping leads to inter-symbol interference, eventually resulting in a higher frequency BER. To reduce frequency chirping, the XFP transceiver uses an inbuilt intensity modulator employing external modulation that includes a distributed feedback (DFB) laser integrated with an electro-absorption modulator. This type of configuration is also called external modulation, which can provide an extinction ratio of around 9 dB. First, the two signals are fiber-coupled into the two FTBs which emulate the uncorrelated fading. After that, the faded signals are separately coupled to their respective collimators, and then these two beams are propagated in free-space, combined with a beam combiner, and eventually coupled into the receiver. The received power statistics are used to plot the PDF and the BER curves, as will be shown in the following sections. It is to be mentioned that the receiver used to measure power statistics is not shown in this picture. It is a low bandwidth receiver that captures only the power fluctuations instead of the high-speed signal.

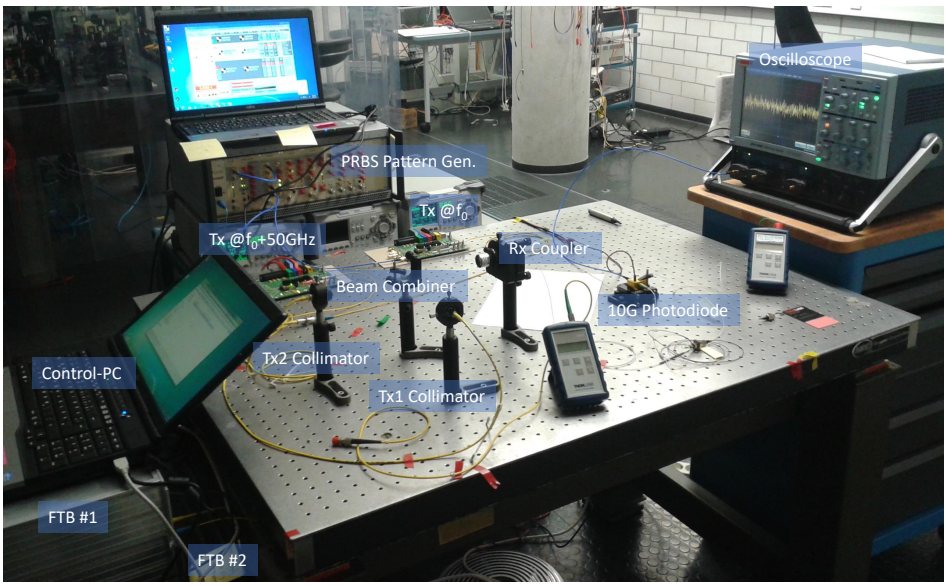

Figure 3.4.: Picture of the experimental setup to demonstrate the two-fold transmitter diversity in the presence of fading emulated by the fading testbeds

3.2. Measurement results

The measurements are repeated by switching on only one transmitter and then switching on both to verify the improvement in signal stability due to diversity. Mean received power in all three cases is kept the same to show that the improvement is due to reduced outage probability and not because of higher SNR when using two beams. Performance parameters to verify the effectiveness of this setup are given in the following subsections.

3.2.1. Probability density function

Fig. 3.5 shows the PDF curves of the distributions of the received optical powers for the three cases. The distribution of these signals are captured on a picoscope using a low bandwidth optical power sampling sensor. The results show that the sum of the two beams reduces the probability of deep fades compared to the case when only one transmitter is used to send the data signal in the uplink direction. The PDF curve is expected to move further away from 0 on the x-axis as the number of transmitters increases which shows a more stable signal.

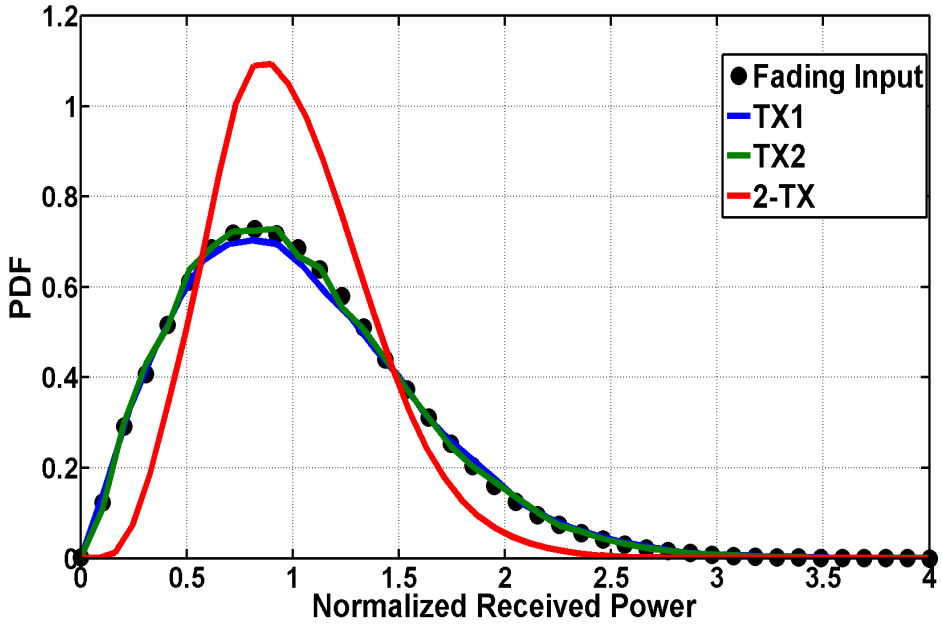

Figure 3.5.: Probability density curves of the received power distribution for the three cases at the same mean power

3.2.2. Scintillation index

Scintillation indices are calculated for the three cases and compared with the scintillation index of the used fading signal, which is 0.27. Scintillation is defined as the ratio of the

variance of the received power to the square of the mean received power [3]. The values of scintillation indices for the single beam and with transmitter diversity are included in Table 3.1. The scintillation indices for the measured signals match closely with the expected 0.27 value when only one beam is transmitted. However, it can be noted that it is reduced by half when transmitting both beams simultaneously showing the improvement in signal stability with less fluctuations using the transmitter diversity scheme.

Case	Tx1 only	Tx2 only	Both Tx
Scintillation Index	0.26	0.25	0.13
Relative Error	3.7%	7.4%	3.7%

Table 3.1.: Comparison of the scintillation indices between the measured fading vector from the ArtemEx campaign and the regenerated signals in the lab experiment using FTBs

3.2.3. Bit error rate

Mean BER values for the three cases in the transmitter diversity scheme are obtained from the power statistics of the received signal using a typical commercial APD receiver's sensitivity characteristics using the receiver model for binary modulation scheme [34]. The receiver sensitivity curves for these three cases are shown in Fig. 3.6 where a diversity gain of 2.3 dB can be noticed at BER=10^{-6} showing the benefit of transmitter diversity for data communications.

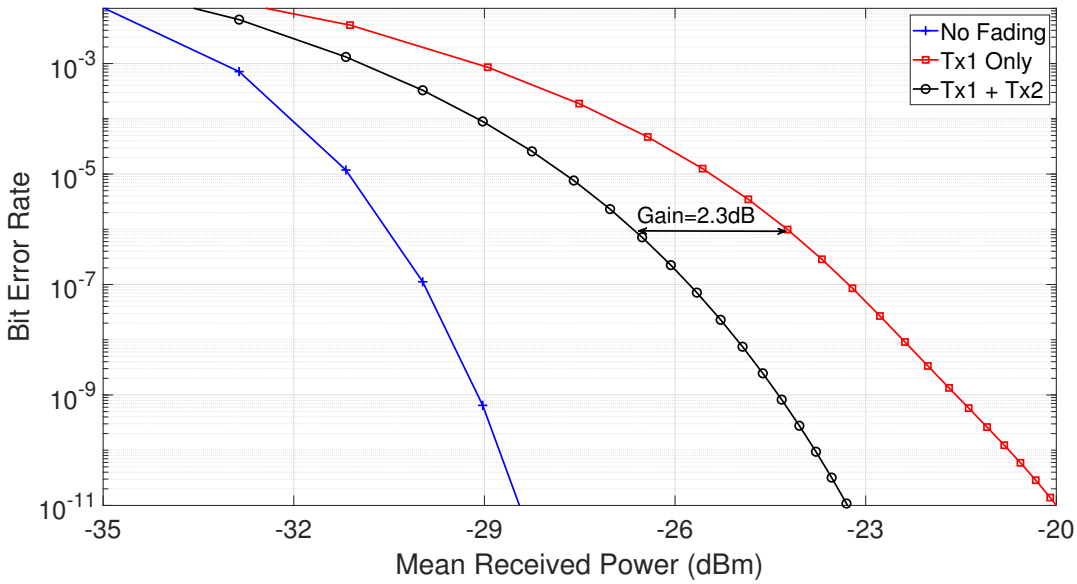

Figure 3.6.: Receiver sensitivity curves plotted from the measured received power statistics and using receiver model of a commercial 10Gb/s APD receiver

4. Investigation of the optical transmitter diversity scheme

This Chapter is subdivided into two parts. The first part deals with the analysis of the transmitter diversity scheme with pointing errors only. The second part describes the optimization of an M-fold transmitter diversity scheme with beam wander and scintillation.

4.1. Analysis of the transmitter diversity scheme with pointing errors only

In this Chapter, an analytical expression is derived for the reduction of the overall scintillation index for a given number of transmitted beams in a MISO system considering solely the effect of atmospherically induced beam wander. The analysis is carried out by combining the beta PDF of the multiple optical signals at the receiver in the presence of atmospherically-induced beam wander. The PDF for a single input single output (SISO) system is taken from [31, 73, 74, 75]. In this analysis, the beam divergence, beam wander, and transmitted power of each beam are set as free parameters. The analytical results are simulated using realistic parameters for the GEO uplink. This analysis helps to choose the values of these free parameters to obtain the desired gain and minimize the overall power scintillation index (PSI). Here, it is assumed that the carrier frequencies of the laser beams are kept wide apart from each other such that no spectral interference occurs between the neighboring signals when they are combined in the receiving photodiode. The interference between the neighboring signals due to spectral overlapping is investigated in Chapter 6.

4.1.1. Derivation of power scintillation index due to pointing errors in multiple beams

In the absence of pointing jitter and assuming a Gaussian beam, the irradiance I_{r} seen by the satellite receiver after the optical wave propagates through the turbulent atmosphere in an FSO link at a propagation distance Z in the far-field and in the direction α from the optical axis (OA), can be expressed as [76]

$$I_{\mathrm{r}}(\alpha, Z) = \frac{2P_{\mathrm{t}}}{\pi(\omega_0 Z)^2} \exp\left(-2\frac{\alpha^2}{\omega_0^2}\right) \tag{4.1}$$

where ω_0 is the $1/e^2$ beam divergence half-angle and P_t is the transmitted power. The first term in Eq. (4.1) is the axial intensity, and the exponential term is the Gaussian function with its peak at $\alpha = 0$ (on-axis) and it drops monotonically with increasing α.

In the presence of pointing errors, the pointing PDF with angular random jitter of σ_j due to the turbulence is the Nakagami-Rice distribution and is given in [77, 74]

$$p_j(\alpha,\varphi) = \frac{\alpha}{\sigma_j^2}\exp\left(-\frac{\alpha^2+\varphi^2}{2\sigma_j^2}\right) I_0\left(\frac{\alpha\varphi}{\sigma_j^2}\right) \tag{4.2}$$

where φ is the bias beam-pointing error angle from the OA and $I_0(\cdot)$ is a modified Bessel function of the first kind and order zero. We assume that the bias error angle can be regarded as zero here and now the pointing PDF in Eq. (4.2) reduces to Rayleigh distribution as

$$P_j(\alpha,0) = \frac{\alpha}{\sigma_j^2}\exp\left(-\frac{\alpha^2}{2\sigma_j^2}\right).$$

It is assumed that the intensity I is normalized to the axial intensity. This I is given by the exponential term in Eq. (4.1). Therefore, the PDF of I becomes the beta distribution and is given according to [78, 77]

$$p(I) = \beta \cdot I^{\beta-1}, \qquad 0 \le I \le 1. \tag{4.3}$$

where $\beta = \frac{\omega_0^2}{4\sigma_j^2}$

$$\bar{I} = \frac{\beta}{\beta+1}$$

$$\mathrm{var}(I) = \frac{\beta}{(\beta+2)(\beta+1)^2}$$

where $\bar{I}$ and $\mathrm{var}(I)$ are the mean and the variance of the received intensity, respectively.

The scintillation index analysis presented in this Chapter takes the beta PDF in Eq. (4.3) into account to come up with an overall scintillation index for the combination of N transmitted beams in a MISO system considering pointing errors only. Here, PSI is defined as the power variance normalized by the square of the mean value. A power scaling factor p is included for the transmitted power of each beam, and now it can be considered that $I_m = p_m I$ where p_m is the power scale factor of the mth beam. The PSI for a SISO system with pointing errors is:

$$\mathrm{PSI}_{\mathrm{SISO}} = \frac{\mathrm{var}(I_m)}{\mathrm{mean}(I_m)^2} \tag{4.4}$$

$$= \frac{\mathrm{E}\left[I_m^2\right] - \mathrm{E}\left[I_m\right]^2}{\mathrm{E}\left[I_m\right]^2}.$$

where $\mathrm{E}[\cdot]$ is the expected value of the random intensity I when it follows the beta distribution. Using the definition of $\mathrm{E}[\cdot]$, Eq. (4.4) can be written as

$$\mathrm{PSI}_{\mathrm{SISO}} = \frac{\int_0^1 I_m^2 p(I)dI - \left(\int_0^1 I_m p(I)dI\right)^2}{\left(\int_0^1 I_m p(I)dI\right)^2}.$$

The integration limits vary from 0 to 1 because of the normalization of the received beam irradiance. The mean and variance of the beam are given as $\overline{I_m} = p_m \overline{I_m}$ and $\mathrm{var}(I_m) = p_m^2 \mathrm{var}(I)$, respectively. After solving Eq. (4.4), the final PSI of a SISO system with pointing errors comes out to be

$$\mathrm{PSI}_{\mathrm{SISO}} = \frac{1}{\beta(\beta+2)}. \tag{4.5}$$

Eq. (4.5) can be extended to include the effect of multiple incoherent beams with pointing errors. It can be written as [79]

$$\mathrm{PSI}_{\mathrm{MISO}} = \frac{\sum_{m=1}^{N} \mathrm{var}(I_m)}{\left(\sum_{m=1}^{N} \bar{I_m}\right)^2}$$

which yields

$$\mathrm{PSI}_{\mathrm{MISO}} = \frac{\sum_{m=1}^{N} \frac{p_m^2 \beta_m}{(\beta_m+1)^2(\beta_m+2)}}{\left(\sum_{m=1}^{N} \frac{p_m \beta_m}{\beta_m+1}\right)^2} \tag{4.6}$$

where p_m and β_m are the power scaling factor and beta parameter of the mth beam, respectively.

4.1.2. Simulation procedure for evaluating transmitter diversity

To verify the scintillation indices of the SISO and the MISO system as given by the expressions in Eq. (4.5) and Eq. (4.6), respectively, numerical simulations are performed for an optical signal with pointing errors in the uplink of a ground-GEO satellite channel. We assume symmetric Gaussian functions along the x and y direction from the OA. The radial angle α in Eq. (4.1) becomes a random variable in the presence of pointing errors with angular jitters $\sigma_{\mathrm{j},x}$ and $\sigma_{\mathrm{j},y}$ in the x and the y directions, respectively. The $\sigma_{\mathrm{j},x}$ and $\sigma_{\mathrm{j},y}$ are used in Eq. (4.1) to generate the irradiance seen at the satellite. The ω_0 and σ_{j} define the β value of the beam with the received irradiance I_m. The ω_0 for all the beams is kept the same, assuming the collimator and beam size is fixed at the ground station. The performance parameters to evaluate

the benefit of transmitter diversity in mitigating fades due to the pointing errors are taken as PSI and PDF as explained below. The results are presented and discussed in Section 4.1.3.

A. Power scintillation index

The PSI for the beta distributed intensity vector is found by numerically calculating the variance and mean using the definition of PSI in Eq. (4.4). The PSI for this beam is also calculated using Eq. (4.5), which depends on the value of β only. To observe the benefit of the transmitter diversity scheme and to verify Eq. (4.6), four uplink beams are simulated as in the SILEX setup at the OGS at Tenerife in Spain [80]. The beams are simulated with both equal and unequal values of β as in the actual case. Also, the simulations are done taking the unequal transmitted powers, and when the powers are reduced equally by the factor N. In the latter case, the overall scintillation index is expected to descrease by N when all beams have the same values of β [81].

B. Probability density function

Besides that, the PDF of a 4x1 MISO system is compared with that of a SISO system in the same plot. The PDFs are obtained from the histogram of the received intensities.

C. Influence of unequal transmitted powers

Simulations are done to find the optimum transmitted power for each beam to get the minimum PSI using Eq. (4.6) for given values of β. Currently, this optimization is done for 2-Tx diversity, as an example. Two cases are simulated, and in each case, a unique β value of the first beam, i.e., β_1 is fixed, and the β value of the second beam, i.e., β_2 is varied along with the transmit powers to find the combined PSI values. In the simulations, the total transmitted power is normalized to one.

4.1.3. Results and discussion

The results presented and discussed in this section show the benefits of using multiple beams in reducing the fades caused by the pointing errors only. For this purpose, four cases are presented in Table 4.1.

In case I, the transmitted power of each beam is equally reduced by N, and equal pointing jitter is assumed. This case is taken as the benchmark. The sum of powers of the transmitted beams in all cases is same as the individual beam without transmitter diversity for a fair comparison. The value of β is 2.93 as an example which is calculated using $\omega_0 = 6.4\mu$rad and $\sigma_j = 1.87\mu$rad from [82].

In case II, the transmitted power of each beam is kept unchanged while σ_j is varied to see the effect of jitter on the individual and combination of beams.

In case III, jitter for individual beams is kept the same, and the transmitted powers are changed.

Finally, in case IV, both the transmitted powers and jitters are varied to find the combined effect on the overall PSI. The impact of the transmit optical power and jitter values on the selected performance parameters is presented next:

A. Power scintillation index

In the first case, the PSI of a MISO system reduces by a factor equal to the number of transmitters because of the combination of equal irradiance from all the beams at the receiver. This is in accordance with the known theory [81]. The PSI of a SISO and MISO system varies according to Eq. (4.5) and Eq. (4.6), respectively. It is seen that PSI for the SISO system is independent of the beam intensities of the individual beam. However, the PSI for a MISO system changes due to the change in irradiance statistics when multiple incoherent beams are combined in one receiver. As shown later, the overall scintillation index can be controlled by selecting appropriate transmitted power according to the pointing jitter associated with each beam.

Table 4.1.: Comparison between theoretical and simulated PSI values for the SISO and the MISO systems. The value of ω_0 is set to 6.4μrad for all the cases

Beam #	p_m (%)	σ_j (μrad)	β	PSI_{SISO}	PSI_{MISO} from Simulations	PSI_{MISO} from Eq. (4.6)
Case I						
1	25	1.87	2.93	0.069	0.017	0.017
2	25	1.87	2.93	0.069		
3	25	1.87	2.93	0.069		
4	25	1.87	2.93	0.069		
Case II						
1	25	1.87	2.93	0.070	0.018	0.018
2	25	2.01	2.53	0.087		
3	25	2.37	1.82	0.144		
4	25	1.27	6.35	0.019		
Case III						
1	25	1.87	2.93	0.069	0.020	0.012
2	30	1.87	2.93	0.069		
3	35	1.87	2.93	0.070		
4	10	1.87	2.93	0.070		
Case IV						
1	25	1.87	2.93	0.069	0.027	0.027
2	30	2.01	2.53	0.087		
3	35	2.37	1.82	0.142		
4	10	1.27	6.35	0.019		

B. Probability density function

The PDFs for the SISO and MISO system with the four cases in Table 4.1 are presented in Fig. 4.1 - 4.4. The received intensity for the SISO system from Eq. (4.1) is normalized to the maximum transmitted power of one transmitter from the case I while the received intensity

for MISO system is normalized to the total transmitted power of all four transmitters. The improvement in the PDF of a MISO system depends on the pointing jitter values and the transmitted power associated with each beam. The strength of the intensity fluctuations is reduced if the PDF-tail has lower values near the zero on the x-axis. As an example, beam #3 for the case-II as shown in Table (4.1), has the highest jitter and hence, the highest PSI among the four beams, i.e., 0.144. This effect can be seen in Fig. (4.2), where the yellow curve representing the PDF of beam #3 has the highest values near the zero of the x-axis which means that the probability of fades seen by this beam is high. Comparing it with the PDF of the MISO scheme, it can be seen that the tail near zero has lower values which indicates mitigation of the intensity fluctuations. This improvement is quantitatively represented by the reduction in the PSI, i.e., 0.018 as given in Table (4.1).

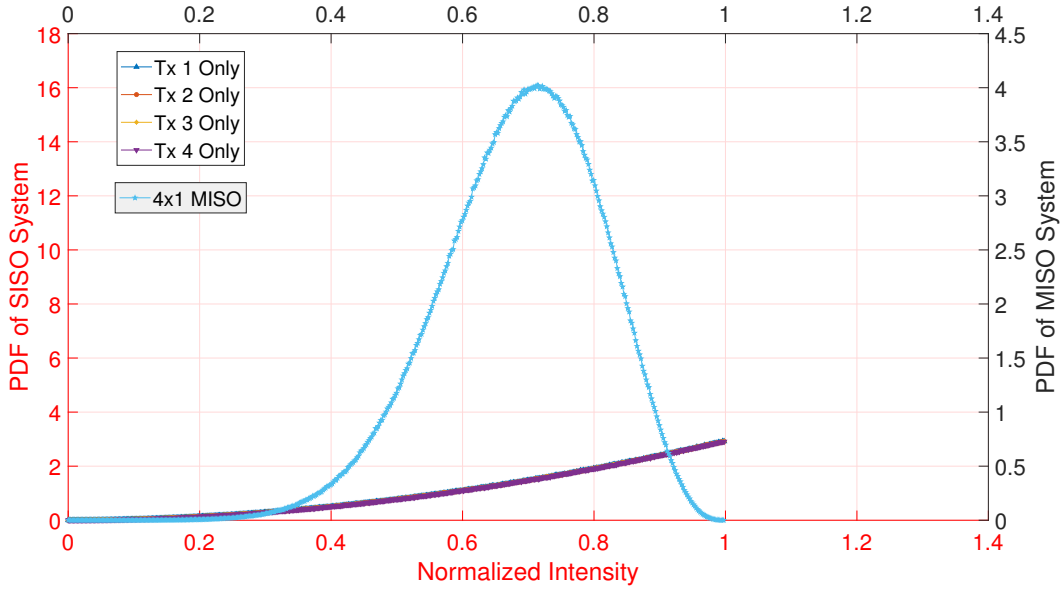

Figure 4.1.: Case-I – Equal transmit powers and equal β values. The curves for the four beams in the SISO case overlap since they are all the same

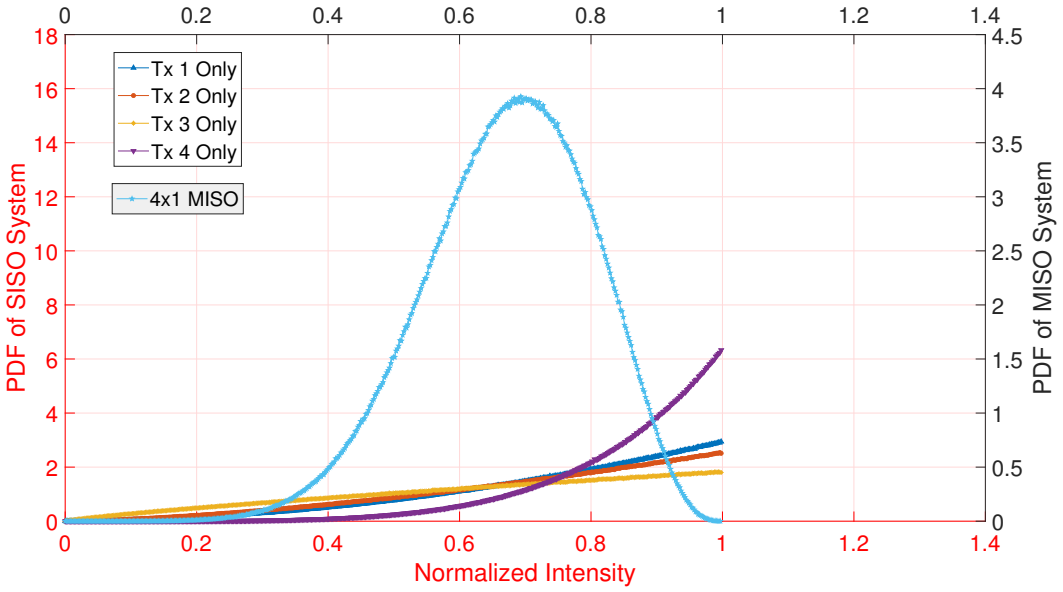

Figure 4.2.: Case-II – Equal transmit powers and unequal β values

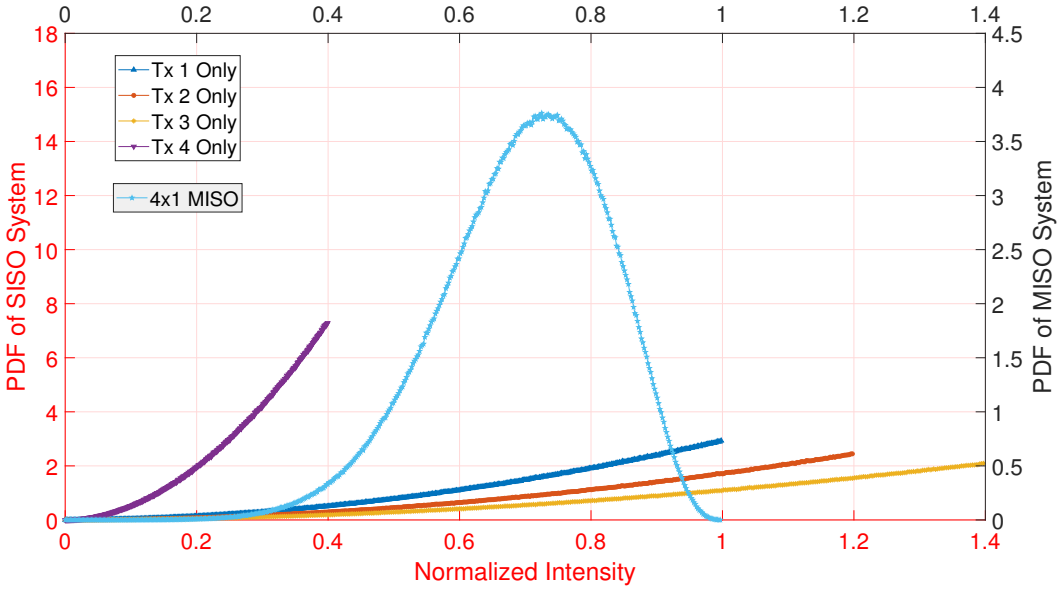

Figure 4.3.: Case-III – Unequal transmit powers and equal β values

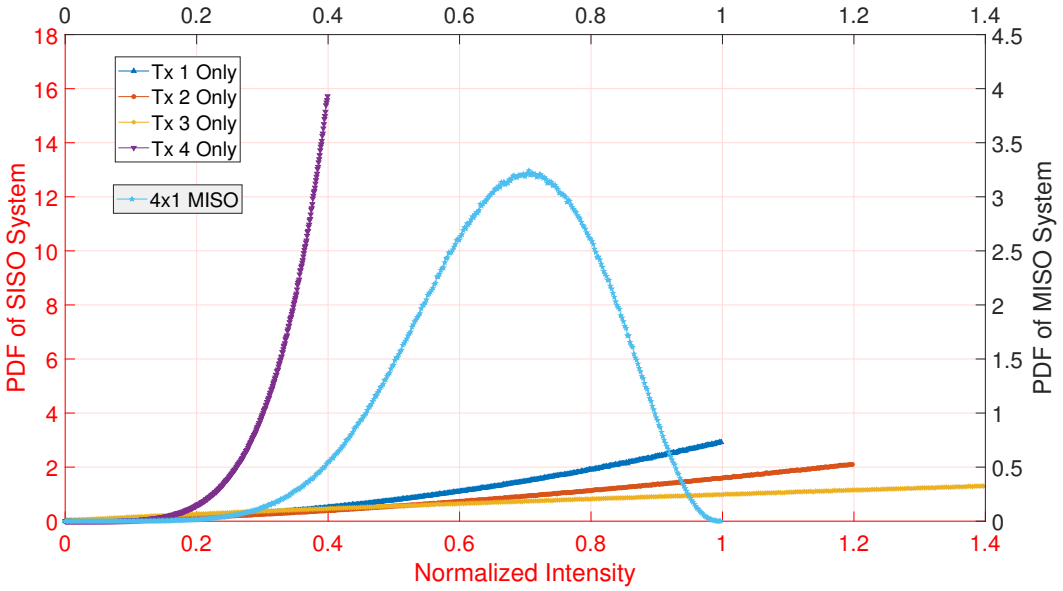

Figure 4.4.: Case-IV – Unequal transmit powers and unequal β values

C. Influence of Unequal Transmitted Powers

The influence of transmitted powers on the combined PSI can be seen in the contour plots in Fig. 4.5 and Fig. 4.6 where values of β_1 are fixed to 2.93 and 5, respectively. These contour plots give a visual representation of the optimization of the transmit powers of the two beams to obtain the minimum PSI for the given β_1 and β_2 values. For each case and a β_2 value, there are optimum transmit powers which result in minimum PSI calculated using Eq. (4.6) and as shown by the red curve in the contour plots. From the plots, we deduce that the beam with the higher β value should have more transmit power to get the minimum combined PSI. The color bar represents PSI values in the logarithmic scale. As an example, referring to Fig. 4.5, if $\beta_1 = 2.93$ and $\beta_2 = 7$, then minimum PSI value of 0.013 can be achieved by setting ratio of P_{Tx1} to P_{Tx2} as 21:79. The contour plot also shows the required value of β_2 and the ratio of P_{Tx1} to P_{Tx2} to get the desired value of PSI by following the corresponding isoline.

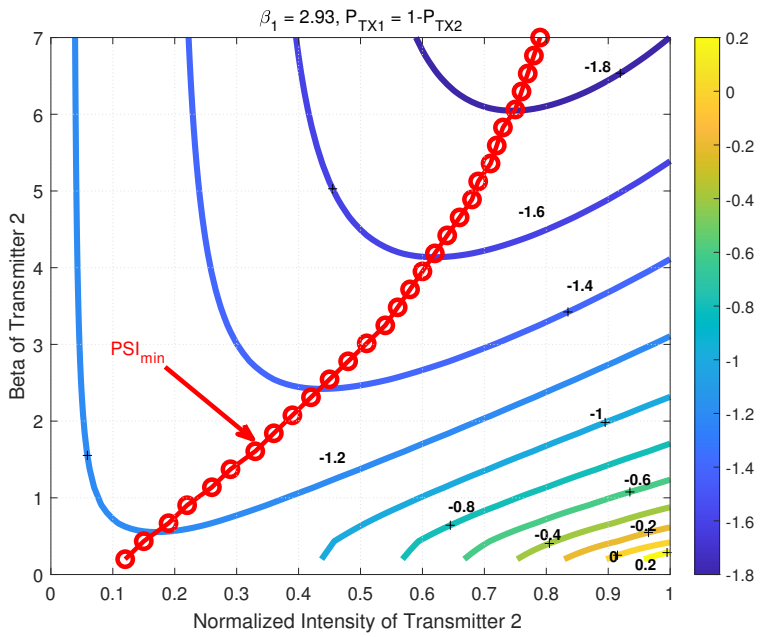

Figure 4.5.: Contour plot displaying the isolines of PSI variations in logarithmic scale

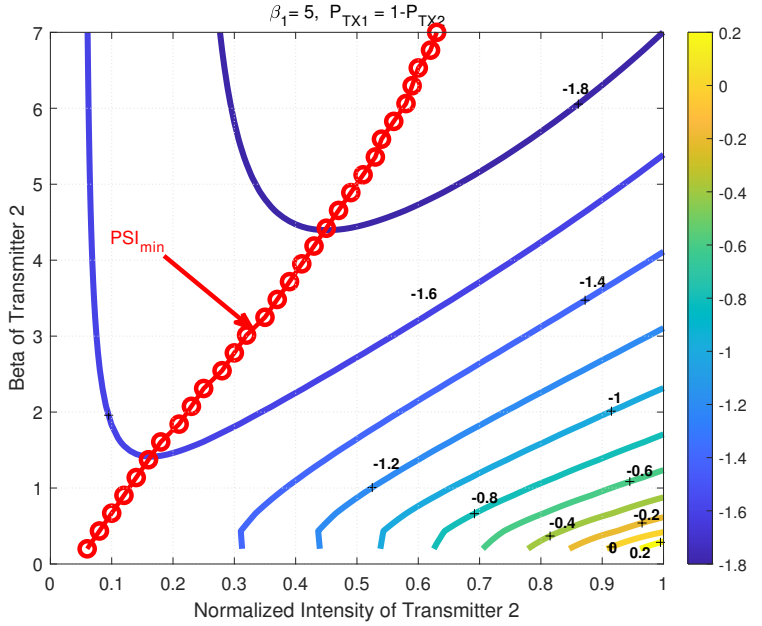

Figure 4.6.: Contour plot displaying the isolines of PSI variations in logarithmic scale

Also, we see the effect of increasing the β_1 value on the combined PSI as shown in Fig. 4.6. When comparing it with the case I in Fig. 4.5, it is seen that the PSI values can be further reduced for the same β_2 if β_1 is increased. However, in this case, the transmit powers for each

of the two beams are changed. As an example, for each case of β_1, three different values of β_2 along with the associated transmit powers to obtain minimum PSI are given in Table 4.3. It can be seen in the first row of the table that when β_1 value in Case II is increased from 2.93 to 5, then a lower PSI value is achieved when P_{Tx1} value is increased from 88% to 94%. This is due to the fact that a higher value of β represents a channel with good atmospheric conditions, i.e., less pointing jitter. Therefore it is sensible to feed this channel with a higher transmit power.

Table 4.3.: Required transmit powers for minimum PSI in a 2×1 MISO system

Nr.	β_1	β_2	P_{Tx1}	P_{Tx2}	PSI_{min}
Case I					
1	2.93	0.20	88	12	0.067
2	2.93	2.93	50	50	0.035
3	2.93	7	21	79	0.013
Case II					
1	5	0.20	94	6	0.028
2	5	5	50	50	0.014
3	5	7	37	63	0.010

4.2. Optimization of an M-fold transmitter diversity scheme with beam wander and scintillation

In this chapter, the performance of the transmitter diversity scheme is quantified over a slow fading channel where the atmospheric turbulence causes scintillation and wandering of the optical beam resulting in deep fades at the satellite receiver. For the given atmospheric conditions and residual beam pointing jitter, each beam's transmit powers are optimized to obtain the minimum overall power scintillation index and maximize the BER gain considering intensity modulation and direct detection.

4.2.1. Channel model

In the weak turbulence regime, the PDF of intensity variation I_{LN} at the satellite receiver is modeled as a log-normal distribution $p(I_{\text{LN}})$ which is given as [74]

$$p(I_{\text{LN}}) = \frac{1}{\sqrt{2\pi}\sigma_{\text{lnI}} I_{\text{LN}}} \exp\left(-\frac{\left[\ln(I_{\text{LN}}/I_0) + 1/2\sigma_{\text{lnI}}^2\right]^2}{2\sigma_{\text{lnI}}^2} \right), \qquad I_{\text{LN}} \geq 0$$

where I_0 is the signal light intensity without turbulence and σ_{lnI}^2 is the log-irradiance variance. The σ_{lnI}^2 is related to the atmospheric scintillation index σ_{I}^2 due to weak turbulence and is given in [3] as

$$\sigma_{\mathrm{lnI}}^2 = \ln(\sigma_{\mathrm{I}}^2 + 1).$$

The PDF of the received intensity I_{PE} in the presence of only residual beam pointing jitter is modeled as a beta distribution $p(I_{\mathrm{PE}})$ which is given in Eq. (4.3). The combined effect of weak atmospheric turbulence and residual beam pointing jitter in the atmospheric channel for a SISO scheme is modeled as the joint PDF given in [74] as

$$p(I) = \frac{\beta}{2I_0}\mathrm{erfc}\left\{\frac{\ln(I/I_0) + \sigma_{\mathrm{lnI}}^2\left(\beta + \frac{1}{2}\right)}{\sqrt{2}\sigma_{\mathrm{lnI}}}\right\} \cdot \exp\left(\frac{\sigma_{\mathrm{lnI}}^2}{2}\beta(\beta+1)\right)\left(\frac{I}{I_0}\right)^{\beta-1}.$$

4.2.2. Numerical simulations

The normalized random intensity due to the weak turbulence is $I_{\mathrm{LN}} = \exp(\mu + \sigma_{\mathrm{lnI}} X_{\mathrm{LN}})$, where $\mu = -\frac{\sigma_{\mathrm{lnI}}^2}{2}$ and X_{LN} represents normally distributed random numbers. The normalized intensity due to the pointing errors assuming circularly symmetric normally distributed jitter is $I_{\mathrm{PE}} = \exp\left(-2\frac{\sigma_j^2\left(X_{\mathrm{PE}}^2 + Y_{\mathrm{PE}}^2\right)}{\omega_0^2}\right)$, where X_{PE} and Y_{PE} are zero mean Gaussian random variables in the x and y direction of the circular aperture, respectively. The normalized received irradiance I_{r} of the Gaussian beam after the optical wave has propagated through the turbulent atmosphere in an FSO link can be expressed as [83]

$$I_{\mathrm{r}} = P_{\mathrm{t}} \cdot \exp\left(-2\frac{\sigma_j^2\left(X_{\mathrm{PE}}^2 + Y_{\mathrm{PE}}^2\right)}{\omega_0^2}\right) \cdot \exp(\mu + \sigma_{\mathrm{lnI}} X_{\mathrm{LN}}). \tag{4.7}$$

To find the optimized transmit power of each beam, numerical iterations of the individual transmit power of each of the beam is performed to obtain the overall minimum σ_{tot}^2 of the combination of all the beams. As an example, four uplink beams are simulated here.

4.2.3. Results and discussions

The value of σ_{I}^2 due to log-normal fading distribution is taken as 0.065 for all the atmospheric paths as it was measured in the experiment for the uplink signal between OGS in Tenerife and Optical Payload Laser Experiment (OPALE) terminal onboard the GEO satellite ARTEMIS and ω_0 for all beams is fixed to 6.4μrad as in [82]. For the comparison, three cases are presented in Table 4.4.

In case I, the transmitted power of each beam is equally reduced by the number of transmitted beams M and an equal residual beam pointing jitter value of 2.17μrad is assumed. This case is taken as the benchmark. The sum of powers of the transmitted beams in all cases is the same as the individual beam without transmitter diversity for a fair comparison. In case II, the residual beam pointing jitter values are varied, keeping the transmit powers of all the beams the same

as in case I to find the combined effect on σ_{tot}^2. This is the case of the unoptimized transmit powers. In case III, transmit powers are optimized as described in Section III to minimize the σ_{tot}^2 value when all the beams have propagated through unequal atmospheric channels. The effect of the power and residual beam pointing jitter values on the selected performance parameters is presented next:

A. Total Scintillation Index

In the first case, σ_{tot}^2 of a multi-beam system reduces by a factor equal to the number of transmitters because of the combination of equal irradiance from all beams at the receiver. The σ_{tot}^2 value for a MISO system changes due to the difference in the irradiance statistics when multiple incoherent beams are combined. As shown in case III, the overall scintillation index can be minimized by selecting optimum transmitted power according to the residual beam pointing jitter associated with each beam.

Table 4.4.: Comparison between σ_{tot}^2 for the SISO and the MISO system. The value of ω_0 is set to 6.4μrad for all the cases

Beam #	P_t (%)	σ_j (μrad)	β	σ_{tot}^2 SISO	σ_{tot}^2 MISO
Case I					
1	25	2.17	2.17	0.1823	0.0455
2	25	2.17	2.17	0.1821	
3	25	2.17	2.17	0.1821	
4	25	2.17	2.17	0.1823	
Case II					
1	25	2.17	2.17	0.1822	0.0877
2	25	3.01	1.13	0.3655	
3	25	2.87	1.24	0.3293	
4	25	4.57	0.49	0.9369	
Case III					
1	36	2.17	2.17	0.1822	0.0812
2	24	3.01	1.13	0.3655	
3	36	2.87	1.24	0.3293	
4	14	4.57	0.49	0.9369	

B. Bit error rate

The BER is calculated using a commercially available 10Gb/s APD and the receiver model from [34]. The BER for the SISO and MISO systems in the presence of log-normal scintillation and residual beam pointing jitter is obtained using the fading statistics given in Eq. (4.7). The BER curves for the three cases from Table 4.4 are plotted in Fig. 4.7-4.9. An improvement by 0.46 dB at the BER value of 10^{-3} is obtained when the transmit powers of the individual beams are optimized as compared to the unoptimized transmit powers.

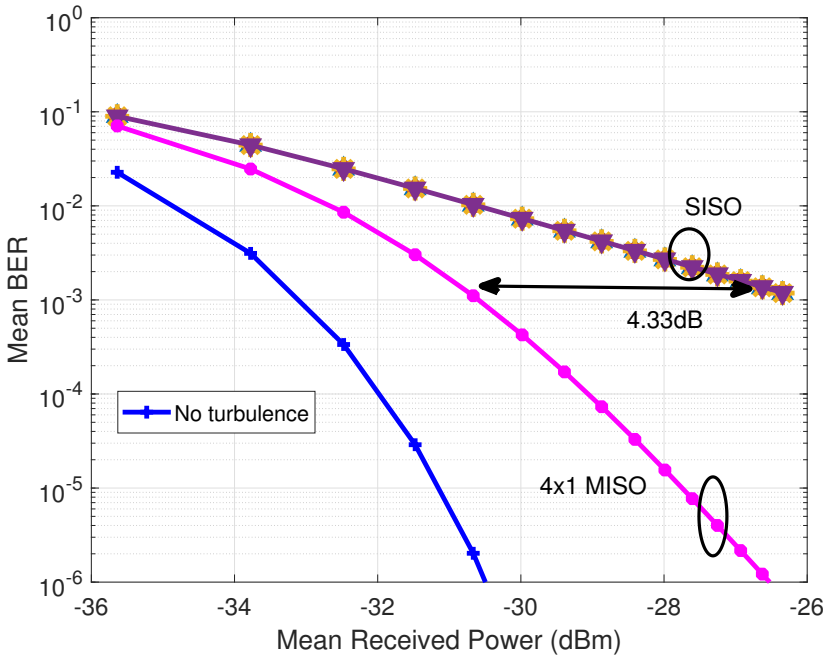

Figure 4.7.: Case I – Equal transmit powers and equal β values. The curves for the four beams in the SISO case overlap since they are all the same

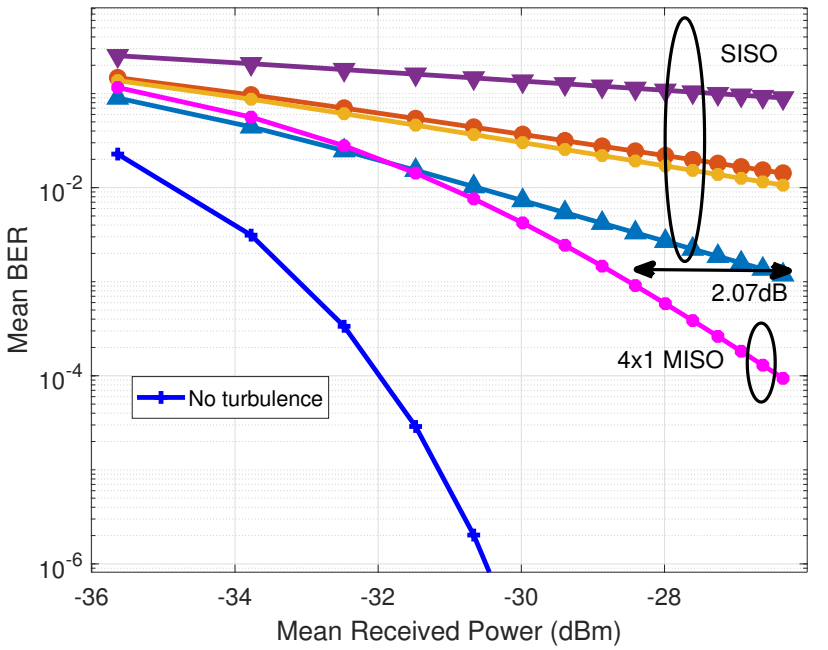

Figure 4.8.: Case II – Unoptimized transmit powers and unequal β values

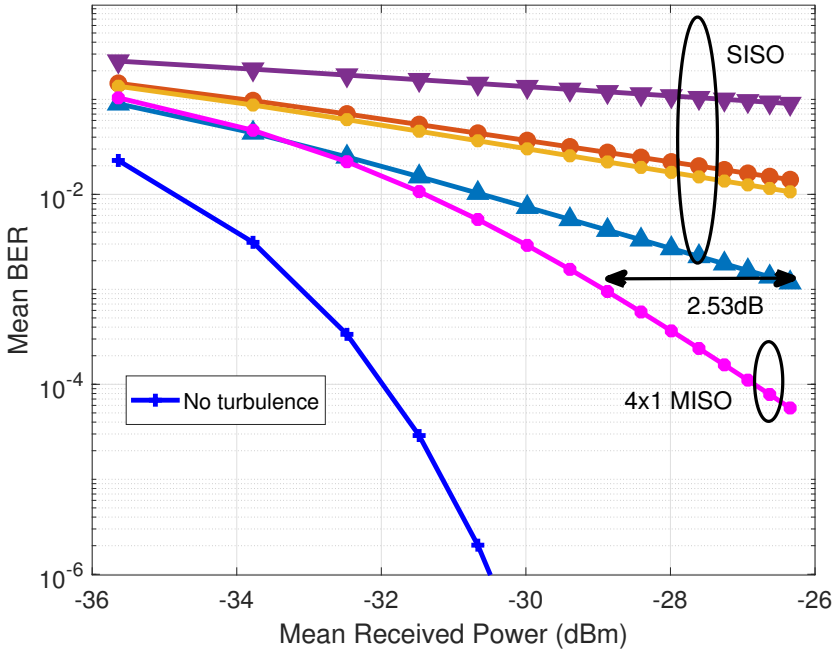

Figure 4.9.: Case III – Optimized transmit powers and unequal β values

4.2.4. Conclusion

In this Chapter, the benefit of transmit diversity in reducing the overall σ^2_{tot} by 7.41% and increasing the BER gain by 0.46 dB as compared to the SISO system is shown. Moreover, optimization of the transmit power per beam according to the channel conditions is shown to maximize the performance of the FSO communications link. The total σ^2_{tot} and BER gain for the optimized transmit power can be improved further as the number of beams is increased. The presented investigations are helpful for the free-space optical communications designers to quantify the performance of MISO schemes for fading mitigation in the turbulent atmospheric channels with the varying residual beam pointing jitter at the satellite.

5. Laboratory demonstration of optimizing an optical single sideband scheme

In this Chapter, a lab experiment is presented to demonstrate a scheme where an OSSB signal is produced to increase the spectral efficiency of the system using a commercially available optical filter with a tunable passband and center frequency. For a 32Gb/s data signal modulated using NRZ-OOK, the required minimum bandwidths of the filter at 6 dB and 20 dB points are measured. Also, the offset of the filter from the carrier is optimized to produce an error-free lower and upper OSSB signal, respectively. Finally, SE of the OSSB signal is calculated. Moreover, the stability of the optical filters and carrier ensures reliable signal generation making the OSSB technique a potential candidate to be used in future free-space optical links.

5.1. Measurement setup

The block diagram of the concept of OSSB scheme to increase the SE of the communications system of a two-fold transmitter diversity scheme is shown in Fig. 5.1. The active components are briefly explained. Furthermore, a back-to-back system test for the generation of one OSSB signal was carried out to demonstrate the system aspects [84].

Optical source: The optical sources consist of two continuous wave (CW) lasers equipped in a chassis with polarization maintaining fiber at the output. The lasers are fully tunable over the C-band and have linewidths down to <25 kHz. This module also supports standard commands for programmable instruments (SCPI) style instructions for remote control access. This enables the lasers adjust to the required power based on the feedback from the detector, as it will be explained later.

External modulator: The two MZMs are used for the external modulation of the corresponding CW lasers. The modulators come with an automatic bias control feature to ensure proper biasing at all times. Here we use the standard intensity modulation scheme.

Bit pattern generator: The bits pattern generator (BPG) provides the data to be transmitted, which is a PRBS of length $2^7 - 1$. The two output channels of the BPG carry the same modulating data for the two MZMs as required by the transmitter diversity scheme. Moreover, it comes with an electrical bit delay feature which is helpful in synchronizing the output of the two channels as this is absolutely necessary for the transmitter diversity scheme.

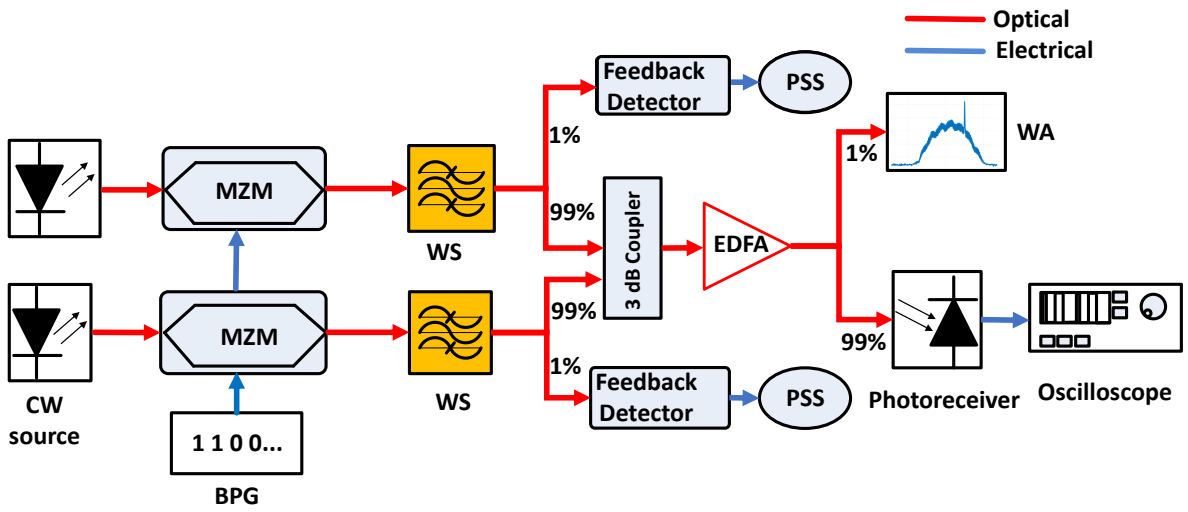

Figure 5.1.: Block diagram of the concept of the OSSB scheme as a 2-fold transmit diversity scheme

Optical filter: The optical filters are integrated into Finisar's waveshaper device. The waveshaper is based on a high-resolution liquid crystal on silicon (LCoS) technology described in [35] and provides complete control over the filter's bandwidth and center frequency. The bandwidth can be tuned from 10 GHz to 5 THz and the device covers the whole C-band. The functionality of remotely controlling the device using SCPI commands provides the flexibility to optimize the SSB signal for a given data rate. The channel shape generated by the waveshaper programmable optical processor is given in Eq. (5.1), which is taken from [35]

$$S(f) = \sigma\sqrt{2\pi}\left[\text{erf}\left(\frac{B/2-(f-f_o)}{\sqrt{2}\sigma}\right) - \text{erf}\left(\frac{-B/2-(f-f_o)}{\sqrt{2}\sigma}\right)\right] \tag{5.1}$$

where B is the 6 dB bandwidth of the filter, f_0 is the center frequency of the filter, and σ is the standard deviation of the optical transfer function that is composed of a relatively narrow Gaussian spectrum given by Eq. (5.2)

$$\sigma = \frac{\text{BW}_{3\text{dB}}}{2\sqrt{2\ln 2}}. \tag{5.2}$$

The 3 dB bandwidth of the optical transfer function is roughly 10 GHz, which suggests that the standard deviation is equal to 4.2466 GHz. The optical spectrum of flat-top bandpass filters created by the waveshaper is shown in Fig. 5.2. It can be seen as the bandwidth B increases, the filter shape becomes more flat at the top. It is also seen for larger B values, that the difference between 6 dB and 20 dB bandwidths of the corresponding filter reduces. For example, the 20 dB bandwidth for an optical filter with B value of 12 GHz and 100 GHz is 24 GHz and

111 GHz, respectively.

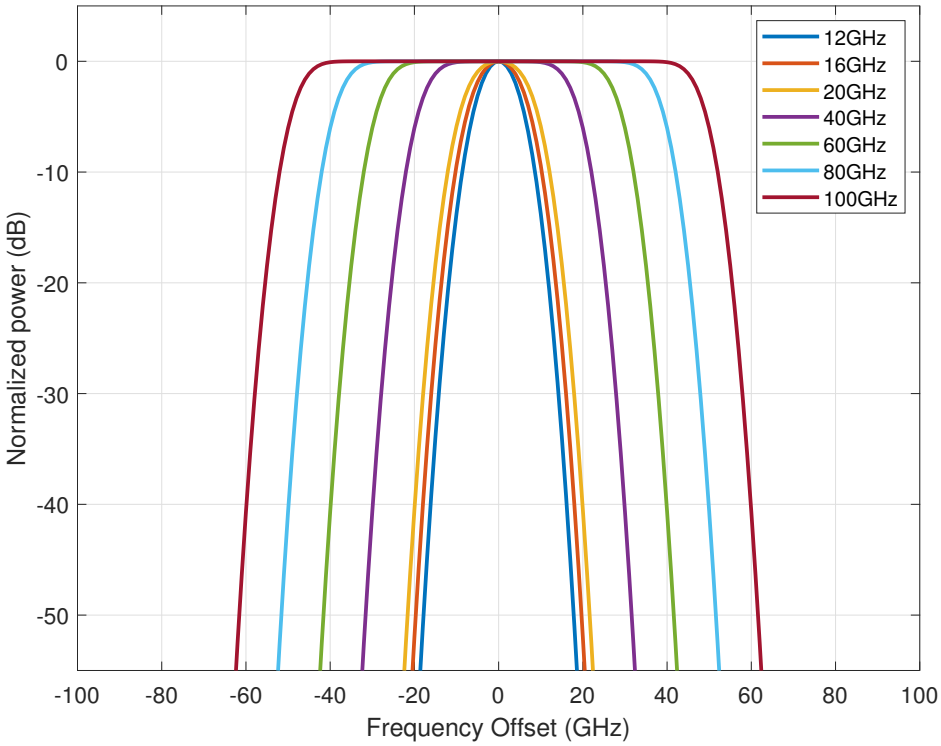

Figure 5.2.: The filter shape, $S(f)$, calculated for different filter bandwidths, B

Optical splitter: One of the outputs of the 20 dB splitter is sent to the feedback detector, and the second output goes to the 3 dB coupler where the signal from the second transmission branch is coupled into.

Feedback detector: The output of the feedback detector is fed to the power sampling sensor, where the DC voltage is used to calculate back the input optical power. This feedback is given to the laser, which adjusts its power accordingly. This is done to keep the signal power of both filtered signals the same at all times.

Preamplifier: An EDFA is used for the preamplification of the incoming combined signal. The preamplifier is necessary as the receiver is not sensitive enough to detect a low-powered signal when the optical filtering significantly cuts down the signal spectrum and carrier.

Photoreceiver: The linear photoreceiver has a 32 GHz bandwidth and is used in the automatic gain control mode with a differential conversion gain of 500 V/W. The photoreceiver is used to make differential measurements to reduce the impact of noise. The sensitivity curves of the receiver with and without equalization are shown in Fig. 5.3. The clock data recovery algorithm is implemented using digital filtering and square timing recovery method described in Section 2.5.6.

Wave analyzer: The wave analyzer (WA) from Finisar is used to record the optical spectrum of the SSB signal. The high spectral resolution of 180MHz (1.25 pm) with a fast update rate

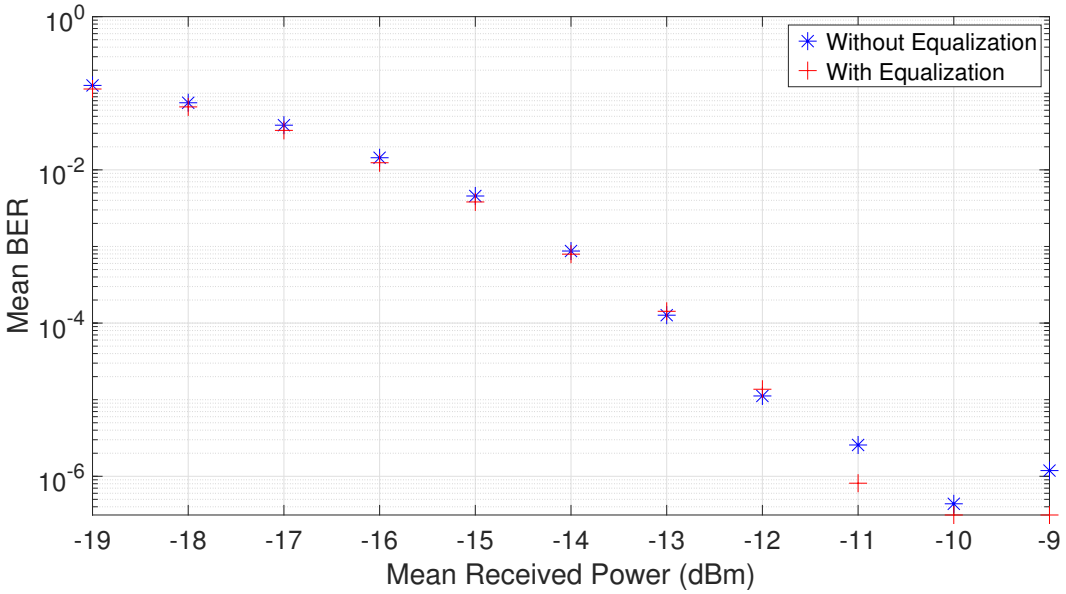

Figure 5.3.: Receiver sensitivity curve of the photoreceiver for a 32Gb/s NRZ-OOK system based on the measurement results

of 4 measurements per second across the entire C-band allows it to be used for modulation analysis on optical signals.

Oscilloscope: An 8-bit real-time oscilloscope with 63 GHz analog bandwidth and sample rate of 160GSa/s is used to record the signal. The captured waveform is used to perform offline digital signal processing to obtain the BER performance as shown in Fig. 5.3.

Fig. 5.4a shows the photo of the experimental setup where the two single-mode waveshapers are used for optical filtering. The feedback detectors are the standard Thorlabs receivers for power monitoring and are used to provide feedback to the source lasers for power adjustments. The high-speed photoreceiver can be seen as well, which feeds the differential RF signal to the oscilloscope for the offline digital signal processing to calculate BER. The two optical transmitters and the PRBS pattern generator source can be seen in Fig. 5.4b.

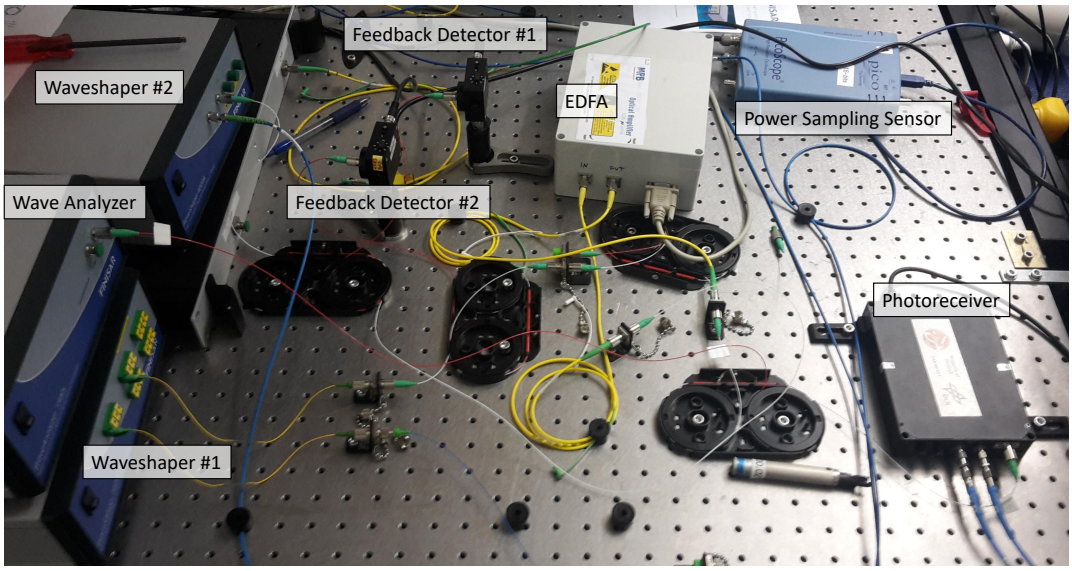

(a) Photo of the experimental setup to generate the OSSB signals and to demonstrate it as a spectral efficient scheme

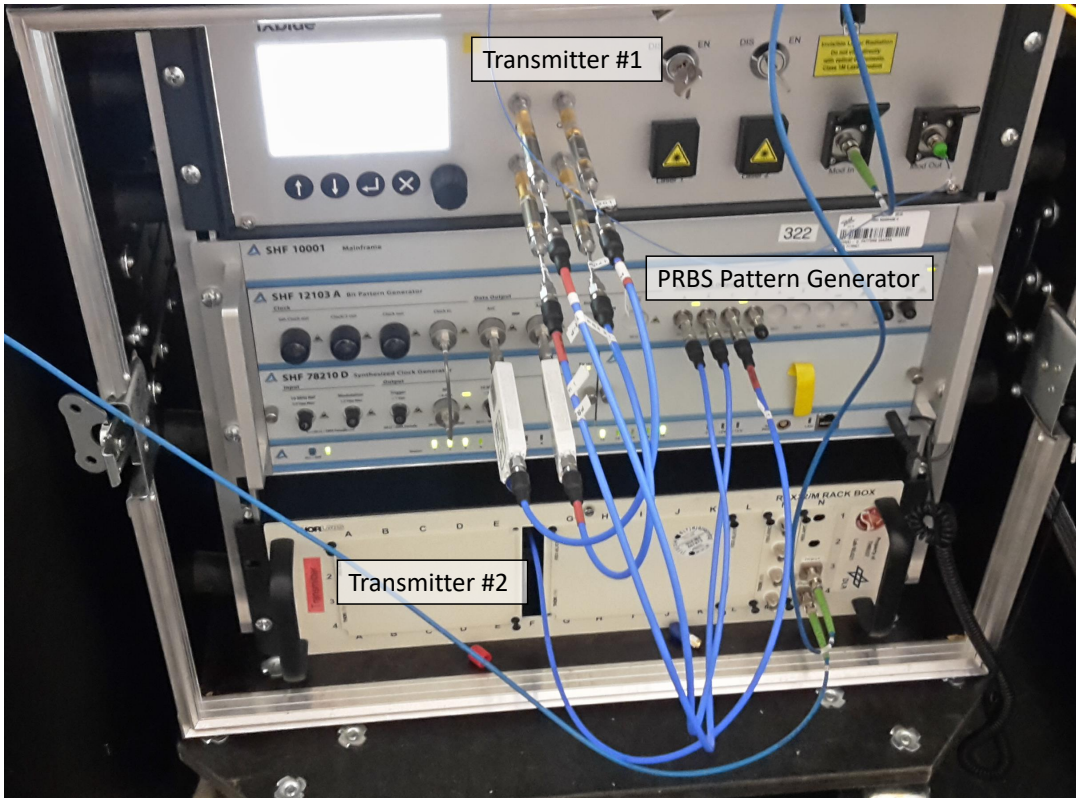

(b) The externally modulated transmitters using MZM modulation and the PRBS pattern generator used as the data source

Figure 5.4.: Experimental setup for the optimization of the OSSB scheme using narrow band steep optical filters and the IM/DD communications system to generate 32Gb/s datarate

Measurement method for the optimization of one OSSB signal

The optimization is performed on two parameters (i) minimum bandwidth required at a given data rate and (ii) maximum frequency offset between the filter and the carrier to obtain the LSB or the USB signals. The mean BER is chosen as the performance parameter. The laser source output optical power is set to its minimum value, which is +6dBm. The carrier is modulated by the PRBS7 data signal at a data rate of 32Gb/s. The modulated signal is fed to the waveshaper, where initially no optical filtering is applied. The signal is only affected by the insertion loss of the waveshaper. The output power is taken as a benchmark, and this benchmark power is kept the same for the filtered signals as well. Upon filtering the signal, the power reduces, which is increased up to the benchmark power by increasing the CW laser's power. This is achieved by taking the feedback from the feedback detector, which measures the change in power between unfiltered and filtered signals using a power sampling sensor. The preamplifier then amplifies the signal to 0 dBm ensuring that the photoreceiver gets enough power to detect the signal. The aim is only to see the effect of optical filtering on the BER. The optical spectrum of the filtered signal is recorded with the high resolution optical WA. After the photoreceiver, the signal is captured on a real-time oscilloscope with analog bandwidth set to 25 GHz and a sample rate of 160GSa/s.

5.2. Measurement results

Mean BER vs. frequency offset between filter and carrier

The optical filters with varying 6 dB bandwidths are swept from the negative to the positive side of the double sideband spectrum to obtain the minimum required bandwidth and optimum filter offset from the carrier at a given data rate. In Fig. 5.5, it can be seen that for an optical filter with 6dB bandwidth of 12 GHz and frequency offset values of -11 GHz and $+10$ GHz, a minimum BER is obtained. These two offset values give the LSB and USB signals, respectively. Beyond these values, the frequency contents of the signals are so much filtered out that the signal degrades, which is shown as an increase in the BER values below -11 GHz and above $+10$ GHz for the case of an optical filter with 6 dB bandwidth of 12 GHz. This filter has a 20 dB bandwidth of 24 GHz which is considered as the minimum bandwidth required for an error-free transmission of a 32Gb/s NRZ-OOK signal. This results in a SE of $1.34\,\mathrm{b/s/Hz}$.

Also, when the optical filter's center frequency is tuned to the carrier frequency, then the BER degrades as well because of insufficient high frequency contents to reconstruct the signal. The frequency contents on both sides of the carrier are the same therefore the useful part of the spectrum with the information content is taken as either side across the carrier. This can be seen from Fig. 5.6 to Fig. 5.11, along with respective eye diagrams and optical spectra of various filters offset settings for optical filter with 6 dB bandwidth of 12 GHz.

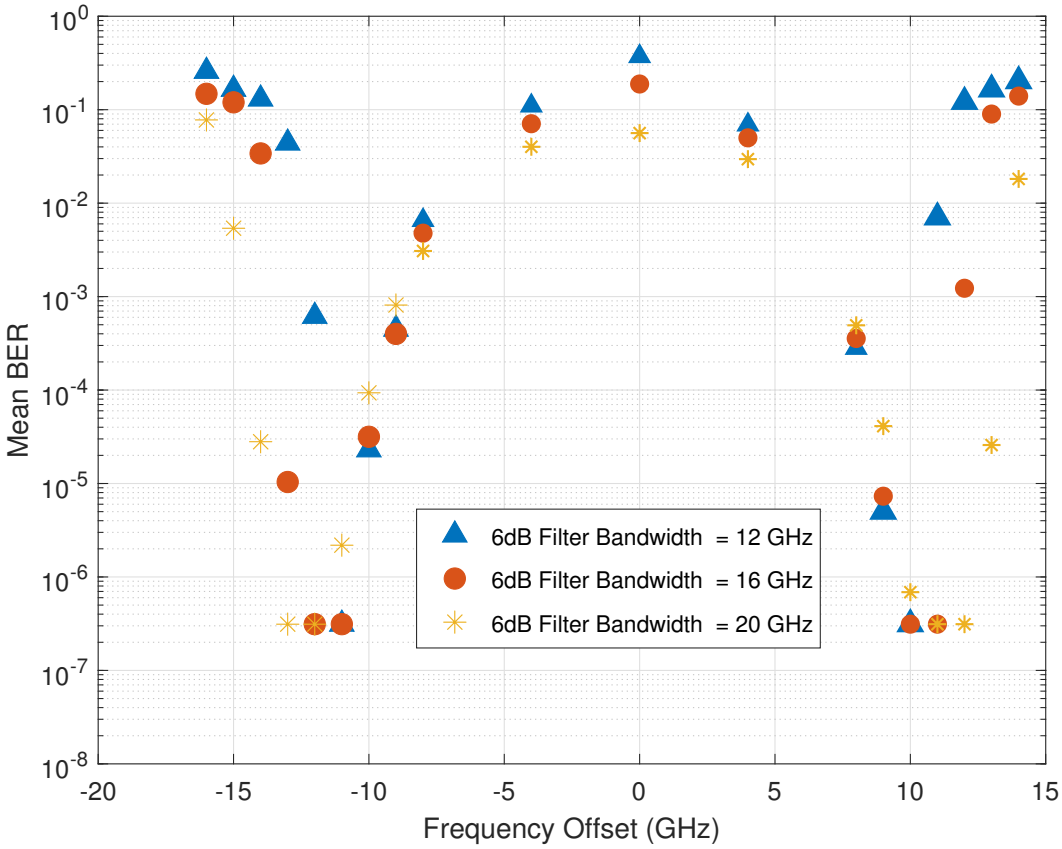

Figure 5.5.: Mean measured BER vs. frequency offset between filter center frequency and carrier

Optical spectra and corresponding eye diagrams

The spectrum of the unfiltered double-sideband signal is shown in Fig. 5.6 where it can be seen that a 32Gb/s NRZ-OOK signal occupies 64 GHz of bandwidth. This results in the SE value of 0.5 b/s/Hz. As the filter is moved from the left to the right side across the spectrum, we observe a point on the left side of the carrier where the filtered signal is error-free. This is the optimum point to generate an LSB signal. Fig. 5.8 shows the spectrum and the eye diagram of the LSB signal. We can see that the filter offset from the carrier is -11 GHz. Similarly, on the right side of the carrier, we can see the optimum frequency offset point at $+10$ GHz to obtain an USB signal. The spectrum and the eye diagram of the USB signal are shown in Fig. 5.10.

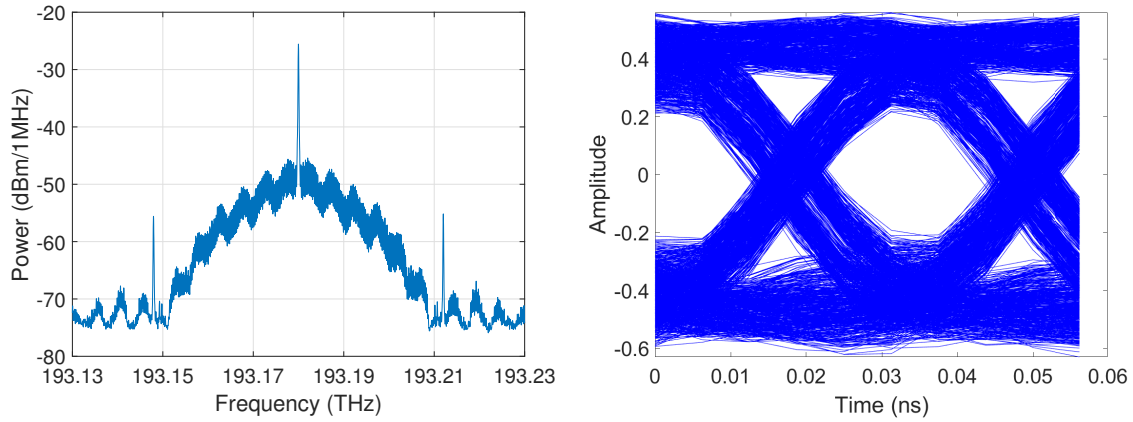

Figure 5.6.: Unfiltered double sideband ASK signal (BER = 0)

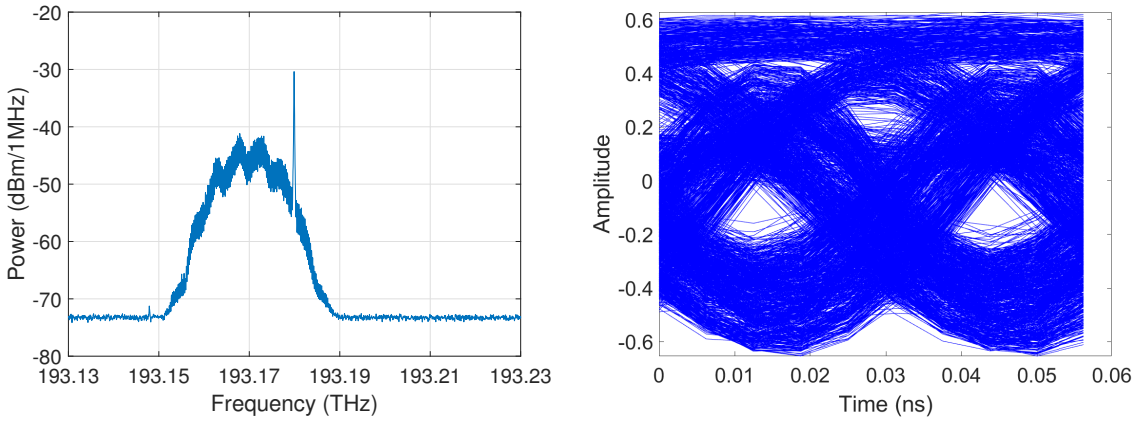

Figure 5.7.: LSB (i.e., half-bandwidth) signal, BW = 12 GHz, Offset = −14 GHz (BER = 0.1)

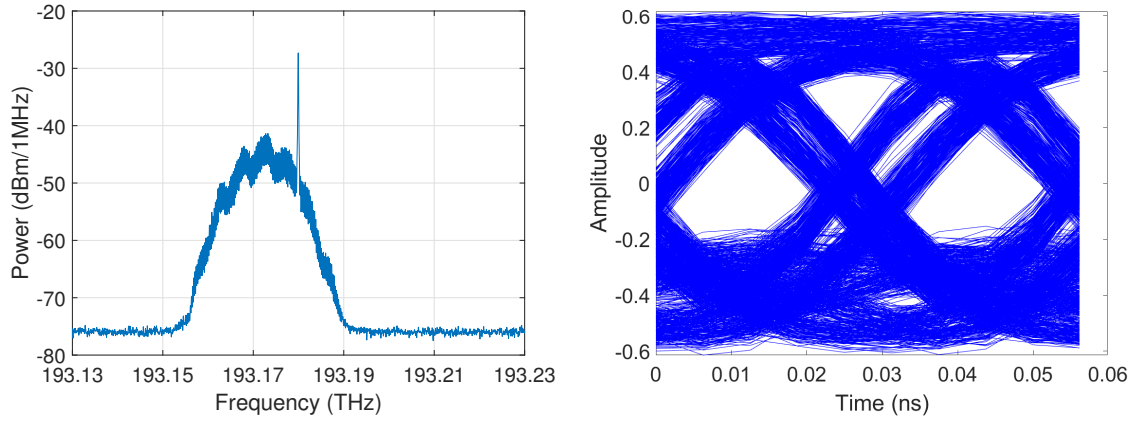

Figure 5.8.: LSB (i.e., half-bandwidth) signal, BW = 12 GHz, Offset = −11 GHz (BER = 0)

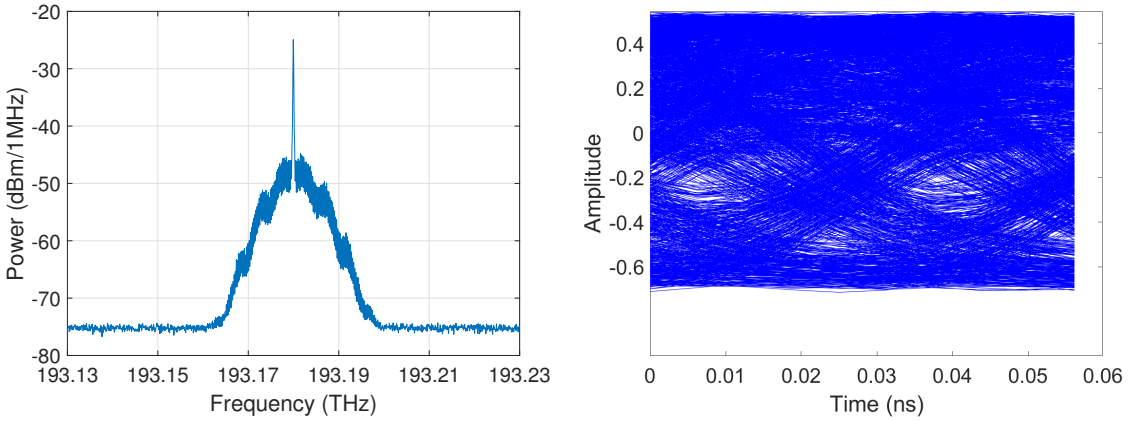

Figure 5.9.: Half-bandwidth filtered signal at carrier frequency, BW = 12 GHz, Offset = 0 GHz (BER = 0.5)

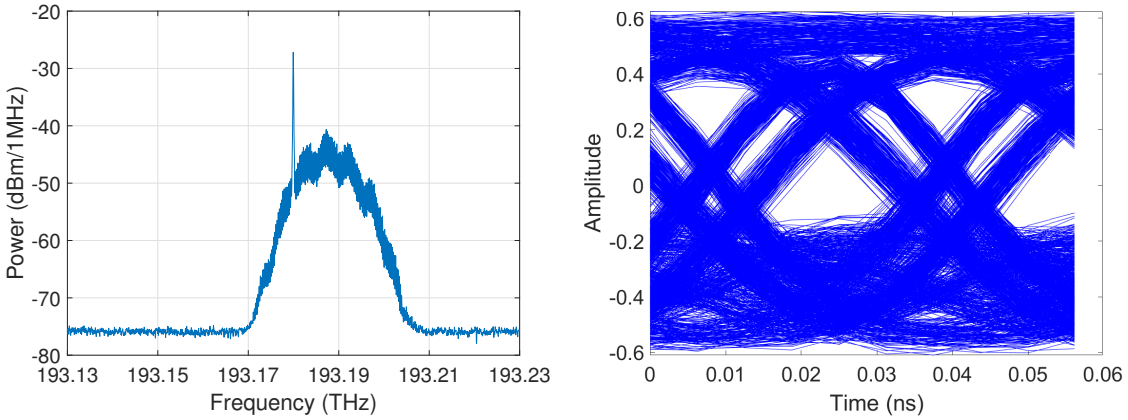

Figure 5.10.: USB (i.e., half-bandwidth) signal, BW = 12 GHz, Offset = +10 GHz (BER = 0)

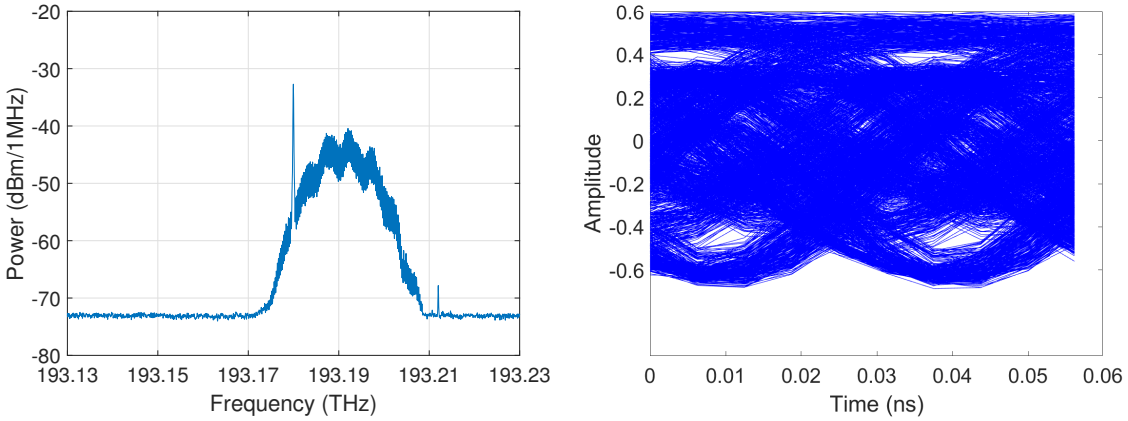

Figure 5.11.: USB (i.e., half-bandwidth) signal, BW = 12 GHz, Offset = +14 GHz (BER = 0.3)

5.2.1. Summary and outlook

An NRZ-OOK scheme for increasing the SE is shown to be a promising technique due to commercially available narrow and steep optical filters. This is a more straightforward approach to producing a single-sideband than complicated techniques like Hilbert Transform and Hartley method. In the Hilbert Transform technique, an OSSB signal is generated using a mathematical approach combined with digital signal processing. The Hartley method uses phasing and a Mach-Zehnder Interferometer to suppress the unwanted sideband. We have presented optimization of one OSSB signal considering an NRZ-OOK amplitude-shift keying (ASK) signal at a data rate of 32Gb/s. The minimum required 6 dB and 20 dB bandwidths of the optical filter are found to be 12 GHz and 24 GHz, respectively. The frequency offsets of the filter from the carrier are measured as -11 GHz and $+10$ GHz to give error-free LSB and USB signals, respectively. The SE of the OSSB signal is found to be $1.34\,\mathrm{b/s/Hz}$ which is 2.68 times more than the SE of the unfiltered signal. As the next step, to obtain the overall SE using a two-fold transmitter diversity scheme, one needs to generate the individual LSB and USB as presented here and optimize the carrier separation between them to a point where interference between the two signals is tolerable to achieve the desired BER performance as is presented in Chapter 6. In the current experiment, the data rate was limited due to the bandwidth of the photoreceiver otherwise, this filtering method can be applied to even higher data rate signals.

6. Simulation of diversity gains after free-space propagation through the atmosphere

In this Chapter, the simulation procedure is presented to obtain the 2×1 diversity gain in the presence of log-normal scintillation and phase piston when the laser beam propagates towards the GEO satellite.

6.1. Simulation of the optical communications system

To simulate the diversity gain in a 2×1 transmitter diversity scheme, a MATLAB-based pass-band simulation platform has been developed as presented in [85] and shown in Fig. 6.1. In these simulations, the data rate R_{b}, optical carrier frequencies f_0 and f_1, optical filter bandwidths, and electrical filter bandwidth are shifted down to Gb/s, and GHz range. The simulation of the optical carrier in the order of THz is avoided to save computation memory requirements and run time. The two carriers are modulated with the same data source and then split into two halves to be fed to their respective optical filters, which are detuned from the carrier to produce USB and LSB. The turbulent atmospheric channel includes the IRT fading and phase piston, which are representative of a GEO uplink channel. On the receiver side, both signals are combined with a 2×1 coupler, and finally, they are detected by a photoreceiver followed by a BER processor. Further details of the individual blocks are presented next.

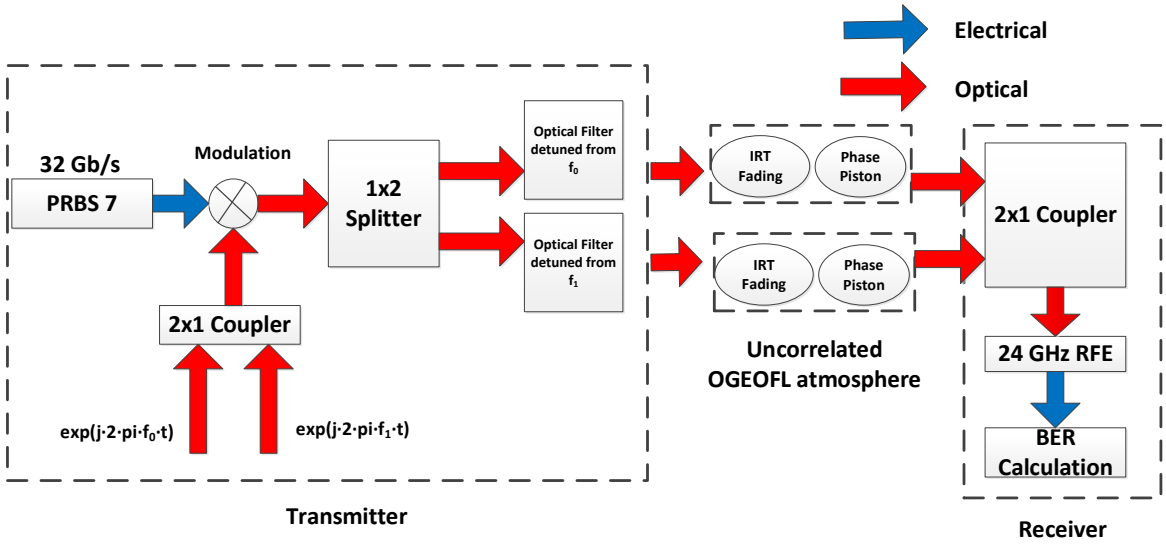

Figure 6.1.: Block diagram of the simulation setup of the optical communications system showing the 2×1 transmitter diversity scheme including the IRT fading and phase piston effects in a GEO uplink scenario. The carriers in this passband simulation are shifted down from THz to the GHz range.

The data rate simulated here is 32Gb/s. This is to compare the results with the experiments as given in Chapter 5. Furthermore, the goal is to simulate the signal spectra and observe the effect of carrier separation on the BER performance in the presence of atmospheric turbulence, as it will be shown in the later sections.

6.1.1. Pseudo random bit sequence

A PRBS is a reproducible pattern that is used to simulate real data traffic to the closest. Such a PRBS sequence can be produced by a linear feedback shift register (LFSR) whose input bit is a linear function of its previous state. A generic block diagram of the LFSR is shown in Fig. 6.2 where the feedback logic is composed of modulo-2 adders. The coefficients $f_i\,(i) = (i = 1, 2, ..., m-1)$ have the value 1 or 0, depending whether the corresponding switch is closed or open. The switches f_0 and f_m are always closed as shown by $f_0 = f_m = 1$. Assuming the initial content of the shift register $s_m s_{m-1} ... s_2 s_1$ is different from all-zero word, the i-th feedback output symbol can be determined by [8]

$$s_i = f_1 s_{i-1} \oplus f_2 s_{i-2} \oplus ... \oplus f_m s_{i-m} = \sum \oplus_{j=1}^{m} f_j s_{i-j}$$

After certain number of clocks, the initial content of register will repeat with maximum possible length of $2^m - 1$. In this thesis, PRBS7 is used for simulations and experiments whose

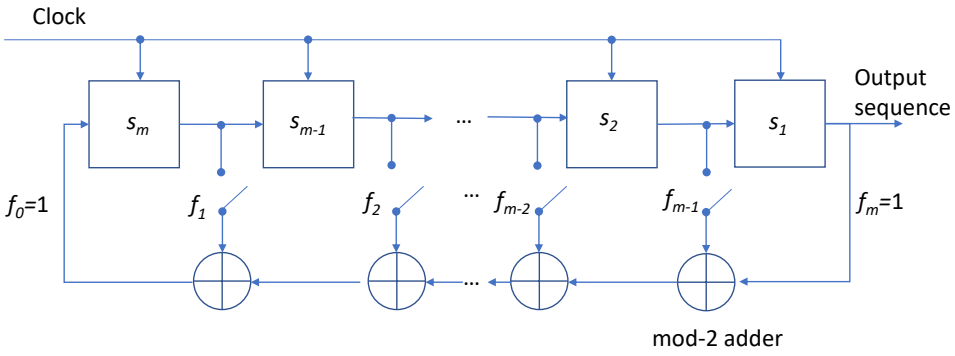

Figure 6.2.: Generic block diagram of the LFSR taken from [8]

generator polynomial is $X^7 + X^6 + 1$ with a sequence length of $2^7 - 1$.

6.1.2. Discrete Fourier transform

Fourier transform is a mathematical formula that relates a signal sampled in time or space to the same signal sampled in frequency. It is a tool to reveal the spectral contents in a time-domain signal. In this thesis, the spectral contents of the spectrum are filtered to obtain USB and LSB. Eq. (6.1) computes the discrete fourier transform (DFT) of a complex signal x_n

$$X_k = \sum_{n=0}^{N-1} x_n e^{-\mathrm{j}2\pi kn/N}, \qquad k = 0, \ldots, N-1 \tag{6.1}$$

where $e^{-\mathrm{j}2\pi kn/N}$ is a primitive N^{th} root of unity. Fig. 6.3 shows the spectrum of a 32Gb/s NRZ-OOK signal. The carrier exists at 150GHz which is shown by a peak, and the two sidebands are spread over 32 GHz on either side of the carrier. Because of redundant information in both sidebands, one of them is filtered out using filters given in Eq. (5.1)

6.1.3. Noise sources

In these simulations, two types of noise sources are considered, namely, the thermal noise and the shot noise, given in Eq. (2.45) and Eq. (2.44), respectively. These noises are added to the electrical signal after the photodetection process. The contribution from other types of noises is considered negligible in this analysis.

6.1.4. Electric filter

A 3rd order lowpass analog Bessel filter is simulated with the cut-off frequency, which is equal to 80% of the data rate. To do the analog-to-digital conversion, the impulse invariance method is used in MATLAB. The impulse invariance method converts analog filter transfer function

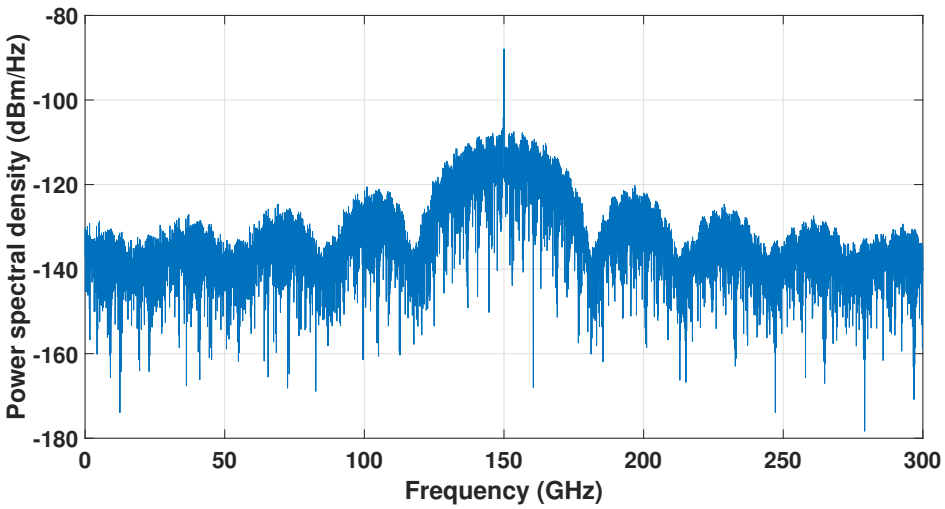

Figure 6.3.: Frequency spectrum of a 32Gb/s NRZ-OOK signal using PRBS7 sequence

to digital filter transfer function in such a way that the impulse response is the same (invariant) at the sampling instants. Moreover, the order of the filter is preserved. It is noticed that the filtering process introduces a delay that is equal to half of the samples per symbol. This delay is compensated by shifting the filtered data by these many number of samples.

6.1.5. Bit error rate

To calculate the number of errors, the demodulated bitstream is compared to the known input bitstream using an XOR operation. The result of such an operation is true if and only if both operands are different. The truth table of the binary XOR operator is shown in Table 6.1 where the bits are compared.

A	B	A⊗B
T	T	F
T	F	T
F	T	T
F	F	F

Table 6.1.: Truth table of a binary XOR used to calculate BER

6.1.6. Receiver sensitivity in a back-to-back setup

The sensitivity curves in Fig. 6.4 compare the simulation sensitivity of a 32Gb/s IM/DD transmission system and the experimental one as shown in Fig. 5.3 in a back-to-back simulation setup. It can be seen that the two curves match within 0.5 dB accuracy showing that the trans-

mission system is simulated correctly and that it can be further used to simulate the optical filtering and eventually the diversity gain under fading and phase piston effects.

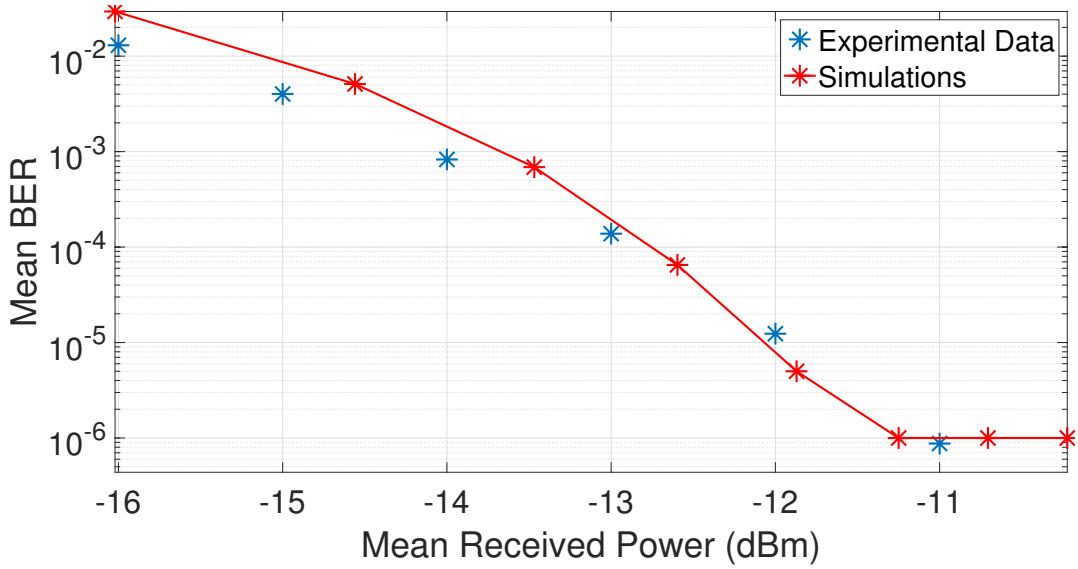

Figure 6.4.: Back-to-back sensitivity curve of a commercially available 32Gb/s receiver. The error floor at BER = 10^{-6} is due to the fact that the simulation was limited to 10^6 bits

6.1.7. Optimization of filter offset and bandwidth

Since an NRZ-OOK signal has redundant sidebands around the carrier frequency, one of them can be suppressed to save bandwidth that eventually increases the spectral efficiency given in b/s/Hz. Spectral efficiency is vital when the required throughput in the OGEOFL is in the order of Tb/s. To achieve this, DWDM technology has to be used utilizing ITU-T channels in the C- and L- bands. When diversity is used for the fading mitigation, the throughput reduces even more, depending on the diversity order. This is due to the reason that multiple DWDM channels carry the same data whose number is equal to the diversity order. If a sideband can be completely suppressed, then that part of the spectrum can accommodate another sideband that doubles the spectral efficiency. However, completely filtering or suppressing the sideband is practically not possible because brickwall filters with infinite slopes do not exist in reality. The state-of-the-art filter like the one given in Eq. (5.1) has a sharp slope that can filter most of the spectral components from the unwanted redundant sideband, but still, some part of it stays. In some literature, this type of sideband is called vestigial sideband (VSB) [86] [87]. For the sake of consistency, single sideband term is used throughout this thesis instead.

To suppress the unwanted sideband as much as possible, optimization between the signal carrier and filter's center frequency is performed. Further, simulations are extended to include various filter bandwidths to find the minimum bandwidth to get the USB and LSB. The filter shapes are simulated using Eq. (5.1). The carrier frequency is kept constant, and the filter

with the given 6dB bandwidth is swept from left to the right of the carrier to get the curves as shown in Fig. 6.5. The plot shows the error floor at 10^{-6} since 1 million bits were simulated. The number of simulated bits is limited to 1 million since the forward error correction (FEC) threshold is around 10^{-3} for the Reed-Solomon code and simulating more bits than that increases the computation time tremendously. The error-free LSB is obtained when the frequency offset between carrier and filter is between -10GHz and -7GHz and the minimum filter bandwidth is 13GHz.

Similarly, the USB is obtained when the offset between filter and carrier frequencies is between +7GHz and +10GHz. If the offset is more than +10GHz, then a significant part of the carrier and low-frequency components are filtered out so that the eye starts to close and BER starts increasing, as it can be seen in the plot. The same reason applies on the left side of the plot for the LSB. Also, it can be seen that if the filter is very narrow, i.e., 12GHz in this case, then a lot of useful high frequency components of the signal are filtered out resulting in a distorted received signal, hence higher BER.

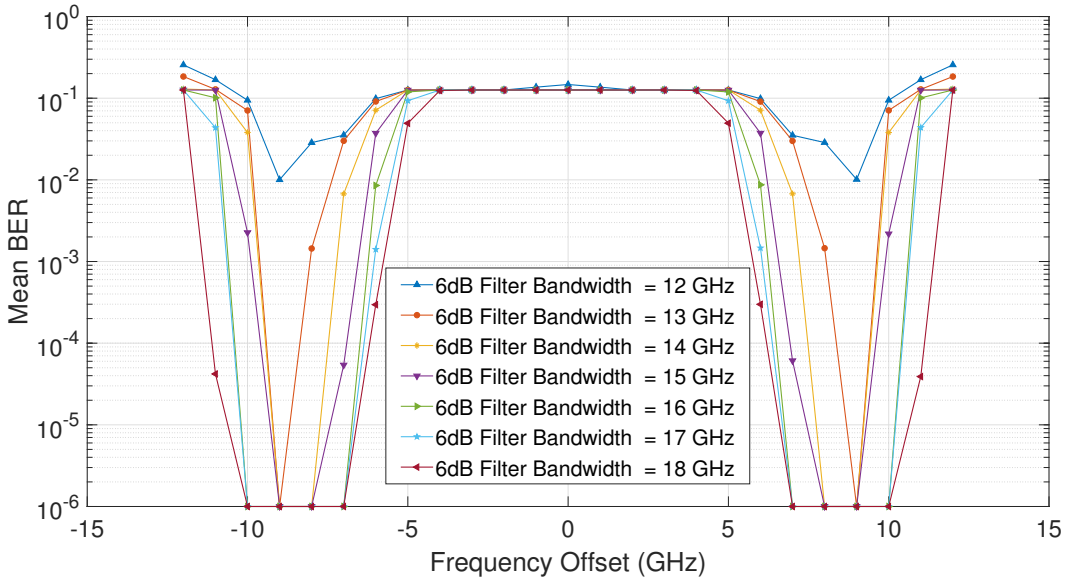

Figure 6.5.: Optimization of the frequency offset between filter center and carrier at a given filter bandwidth

In the real systems, both the filter and carrier drift with temperature. Therefore, choosing the frequency offset value with some margin is sensible. In the following simulations, a frequency offset of 8GHz is chosen. Further, the bandwidth of the filter is taken as 15GHz.

6.1.8. Carrier separation between signals

From Fig. 6.5 optimum LSB and USB signals are selected, and a carrier separation of 66 GHz is chosen for the spectra overlap and to have the effect of the phase piston. The red spectrum in Fig. 6.6 is the LSB and the blue spectrum is USB.

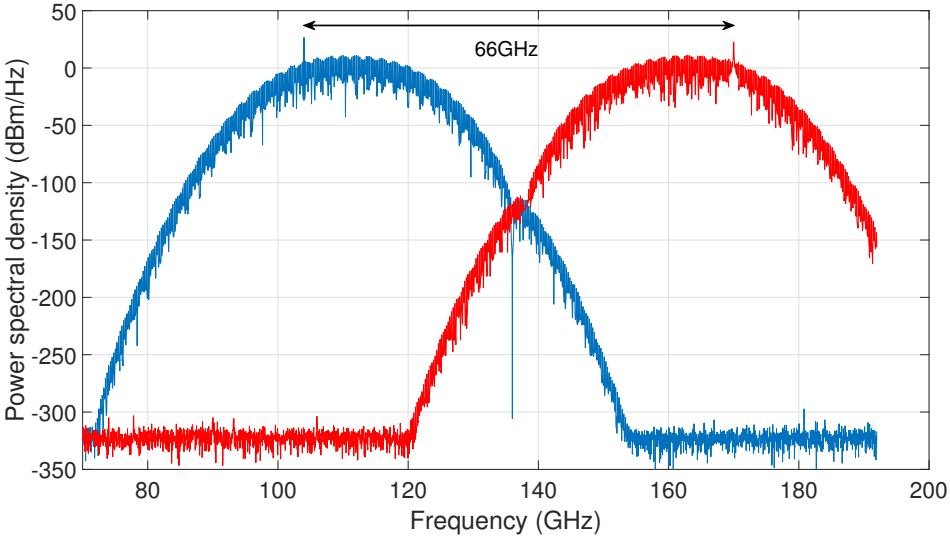

Figure 6.6.: Carrier separation of the USB and LSB signals

6.1.9. Diversity gain in the presence of turbulent atmosphere

The two individual spectra from Fig. 6.6 are propagated through a power vector as shown in Fig. 2.10 having log-normal scintillation and phase piston from Fig. 2.18 is used to vary the phase of the signals. The condition of an uncorrelated atmosphere is simulated by introducing a delay between the two power vectors. It is seen in Fig. 6.7 that a diversity gain of 2.3 dB can be achieved for a two-fold transmitter diversity scheme.

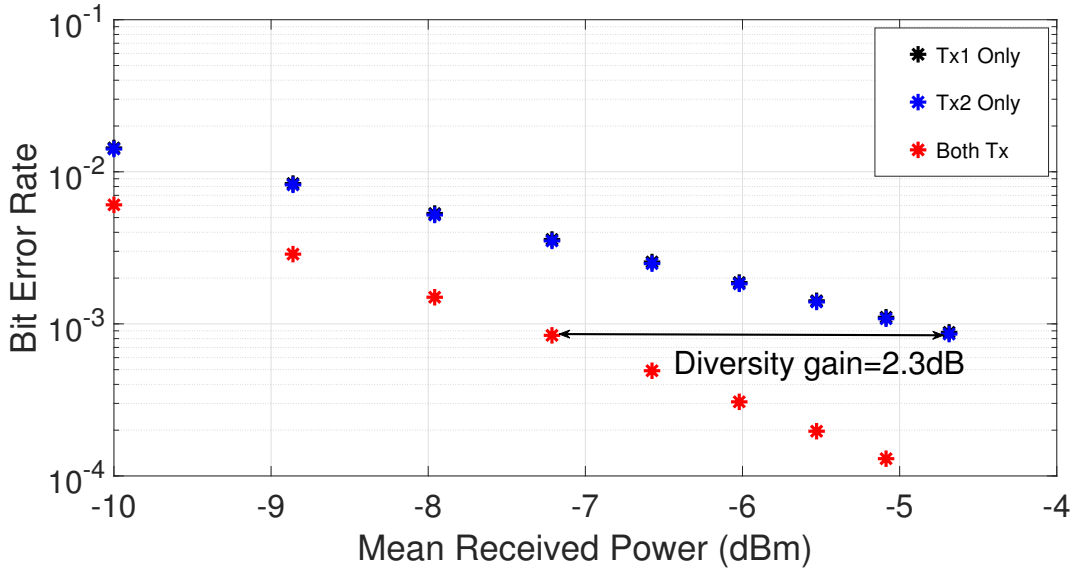

Figure 6.7.: BER vs. carrier separation of the two spectra from Fig. 6.6 and including IRT fading and phase piston effects

6.2. Link budget

A link budget takes into account all the gains and losses that an optical communications signal faces from a transmitter through a free-space channel to the receiver. The expression for the mean received power P_r at the satellite, after having propagated a distance L is given by

$$P_r = P_t G_t L_{Tx} L_{FS} L_{SR} L_{sci} L_{BW} L_j G_r L_{Rx} L_c \tag{6.2}$$

where P_t is the mean power transmitted by the booster amplifier at the OGS, L_{Tx} and L_{Rx} are the optics losses at the transmitter and receiver, respectively . The far-field on-axis gain G_t provided by the telescope with aperture D_T at the OGS assuming no central obscuration and including truncation losses is given by [88]

$$G_t = \left(\frac{\pi D_T}{\lambda}\right)^2 \cdot 2/\alpha^2 \left[\exp\left(-\alpha^2\right)\text{-}1\right]^2, \qquad \alpha \approx 1.12. \tag{6.3}$$

The gain G_r provided by the telescope with aperture D_r at the GEO satellite assuming no central obscuration is given by [89]

$$G_r = \left(\frac{\pi D_R}{\lambda}\right)^2. \tag{6.4}$$

The free-space loss is given by

$$L_{\mathrm{FS}} = \left(\frac{\lambda}{4\pi L}\right)^2. \tag{6.5}$$

The additional beam spread loss L_{SR} beyond that of pure diffraction is given in terms of Strehl ratio as [3]

$$L_{\mathrm{SR}} = \left[1 + \left(\frac{D_{\mathrm{t}}}{r_0}\right)^{5/3}\right]^{-6/5}. \tag{6.6}$$

In the case of uplink, the beam wander loss L_{BW} due to angular beam wander θ_{BW} is given by [90]

$$L_{\mathrm{BW}} = \exp\left(-G_{\mathrm{t}}\theta_{\mathrm{BW}}^2\right). \tag{6.7}$$

The power penalty L_{j} for the required mean BER that results from the variation of the received optical signal power in the presence of jitter is given by [91]

$$L_{\mathrm{j}} = \left(\frac{Q\,|_{\mathrm{BER(Q)=a_{BER}}}}{Q_{\mathrm{r}}\,|_{\overline{\mathrm{BER}}(\mathrm{Q_r})=\mathrm{a_{BER}}}}\right). \tag{6.8}$$

The numerator represents the average BER in the absence of jitter as given in Eq. (2.35) and the average BER in the presence of jitter is given as

$$\overline{\mathrm{BER}} = \int_0^1 p\,(I)\,\mathrm{BER}\left(IQ_{\mathrm{r}}\frac{\beta+1}{\beta}\right)dI$$

$$\overline{\mathrm{BER}} = \frac{Q_{\mathrm{r}}\,(\beta+1)}{2}\int_0^1 I^{\beta+1}\mathrm{erfc}\left(\frac{IQ_{\mathrm{r}}}{\sqrt{2}}\frac{\beta+1}{\beta}\right) \tag{6.9}$$

where $p\,(I)$ is the PDF of the received optical intensity I and follows beta distribution as given in Eq. (4.3). The parameter Q_{r} in Eq. (6.9) is related to the required SNR value that is needed to achieve the desired PDF value of a_{BER}. The penalty L_{j} depends on the desired BER and the ratio w_0/σ_{j} whereas these parameters are explained in Section 4.1.1. The dependence of power penalty on w_0/σ_{j} for the desired BER is obtained using Eq. (6.8) and is shown in Fig. 6.8 where it can be seen that a careful selection of the beam divergence according to the random pointing jitter is to be made to reduce the power penalty. For the link budget presented in this section $w_0/\sigma_{\mathrm{j}} = 10$ is selected for the to achieve BER = 10^{-3}.

The scintillation loss L_{sci} is given by Eq. (2.17) where p_{thr} is taken as 10^{-3} for the link budget calculation. For this analysis, the fiber coupling loss L_{c} corresponds to the theoretical maximum coupling efficiency of 81% [92].

Finally, the receiver sensitivity is obtained by calculating BER from OSNR in a 0.1 nm reference bandwidth B_{ref} using the formula in Eq. (2.36)

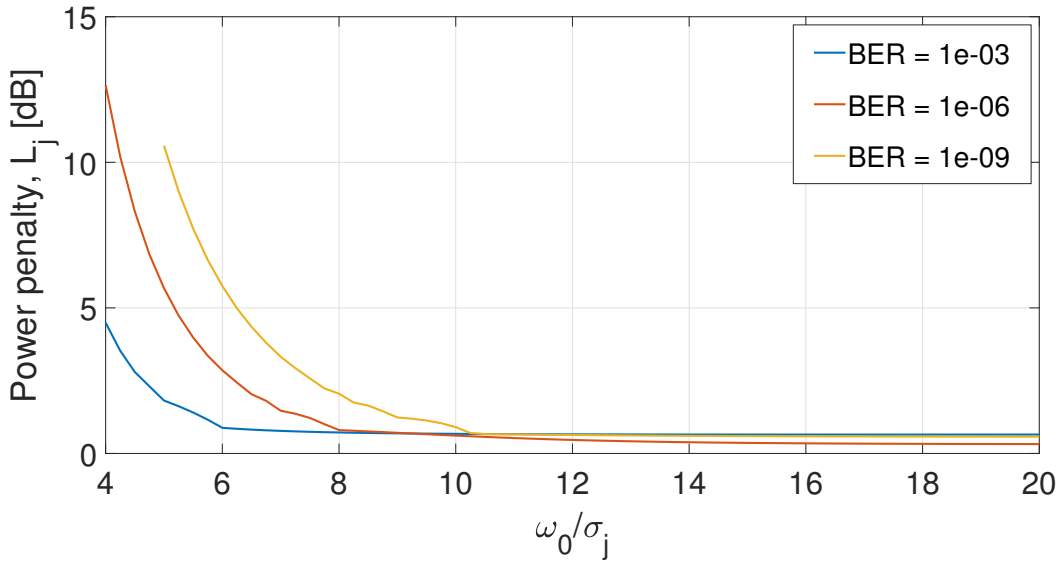

Figure 6.8.: Power penalty for the required BER as a function of the ratio of $1/e^2$ half-angle beam divergence to the random pointing jitter

$$\mathrm{BER}=\frac{1}{2}\mathrm{erfc}\sqrt{\frac{\mathrm{OSNR}\cdot B_{\mathrm{ref}}}{R_{\mathrm{b}}}}. \tag{6.10}$$

A simplistic form of mean received power P_{in} at the EDFA preamplifier can be obtained from Eq. (2.40), which results in

$$P_{\mathrm{in}}\,(\mathrm{dBm}) = \mathrm{OSNR}(\mathrm{dB}) + F\,(\mathrm{dB}) - 58\,(\mathrm{dBm})\,. \tag{6.11}$$

The two forms of sensitivity curves for an ideal noiseless preamplifier with $F = 3\,\mathrm{dB}$ using Eq. (6.11) and Eq. (2.42) are plotted in Fig. 6.9a and Fig. 6.9b, respectively.

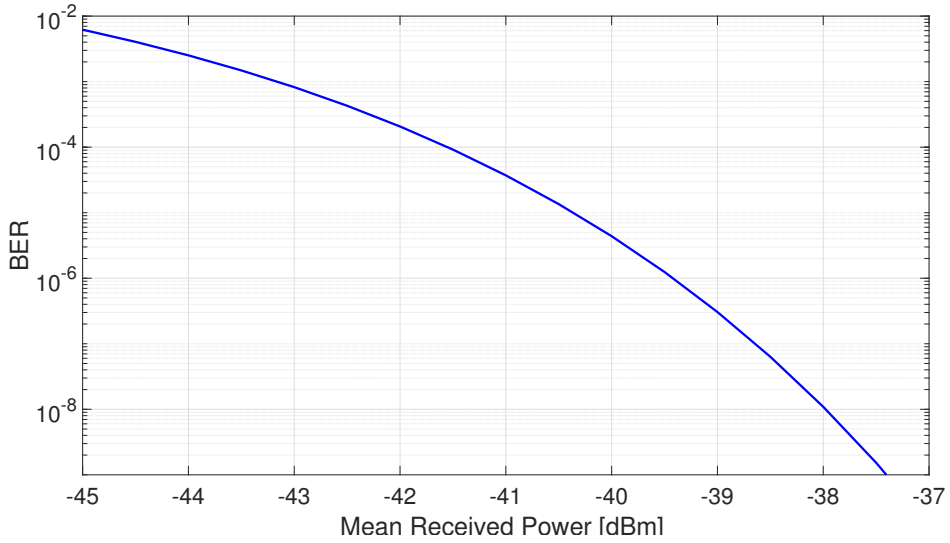

(a) Sensitivity curve showing BER vs. mean received power in dBm

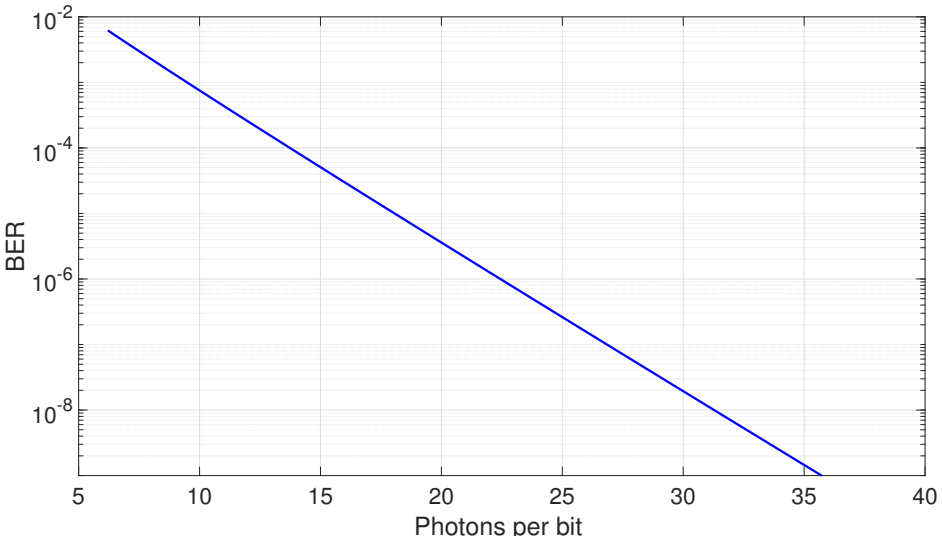

(b) Sensitivity curve showing BER vs. photons per bit

Figure 6.9.: Receiver sensitivity curves for 40Gb/s data signal using NRZ-OOK modulation format

An example link budget in the uplink to GEO satellite as calculated using Eq. (6.2) is shown in Table 6.2. Here the mean required power P_{req} at the receiver is defined for BER=10^{-3}, which is taken as an FEC threshold, whereas the diversity gain is taken from Section 6.1.9.

Parameter	Symbol	Value	Unit
Wavelength	λ	1550	nm
Tx power	P_{t}	+47	dBm
Transmitter aperture	D_{T}	80	mm
Transmitter half-angle divergence	ω_0	17.44	μrad
Transmitter gain	G_{t}	103.31	dB
Transmitter optics loss	L_{Tx}	-2	dB
Scintillation index	σ^2	0.07	-
Scintillation loss	L_{sci}	-3.63	dB
Angular beam wander	θ_{BW}	7.70	μrad
Beam wander loss	L_{BW}	-5.51	dB
Power penalty	L_{j}	-0.67	dB
Fried parameter	r_0	16	cm
Strehl ratio loss	L_{SR}	-1.43	dB
Elevation angle	θ	60	degrees
Link distance	L	44455.97	km
Free-space loss	L_{FS}	-291.14	dB
Receiver aperture	D_{R}	250	mm
Receiver gain	G_r	114.10	dB
Receiver optics loss	L_{Rx}	-2	dB
Fiber coupling loss	L_{c}	-0.89	dB
Diversity gain		2.3	dB
Mean received power	P_{r}	-41.9	dBm
Target BER		10^{-3}	-
Mean required power	P_{req}	-43	dBm
Link margin		+2.43	dB

Table 6.2.: Link budget from the OGS at sea level to the GEO satellite

6.3. Conclusion

In this Chapter, a self-developed Matlab-based passband simulation scheme is shown to give accurate receiver sensitivity results as compared with the experiments. Also, the optimization of the frequency offset between filter center and carrier at a given filter bandwidth optimization is presented using the passband simulation. Moreover, a diversity gain of 2.3 dB is obtained when the two carrier frequencies are separated by 66 GHz. Finally, an example link budget from the OGS at sea level to the GEO satellite is presented where it is shown that in the presence of diversity gain, a positive link margin can be achieved.

7. Conclusion

7.1. Summary

The aim of this thesis is to investigate a fading mitigation technique called transmitter diversity which is a promising candidate in optical uplinks to GEO satellites. Due to the index of refraction variations of the atmosphere caused by the turbulence, the received signal suffers from scintillation and residual pointing errors arising from beam wandering. Both result in deep and long fades, which adversely affect communication performance. These fades can be mitigated up to some extent if multiple beams carrying the same data are transmitted from the ground station where these transmitters are to be separated by more than Fried parameter to satisfy the condition of the beam propagation through the uncorrelated atmospheric paths. In this way, only one ground station is required to achieve terabit throughput using DWDM technology. In Chapter 4, it is quantitatively shown for the case with no spectral overlapping between neighboring signals that by only optimizing the transmit powers for the four beams, 0.46dB diversity gain is achieved when considering scintillation and residual pointing jitter at the satellite. Here, the transmitter experiencing bad channel conditions is fed with less transmit power while more power is allocated to the one with better channel conditions. After that, in Chapter 5, a laboratory experiment is presented to optimize the single-sideband scheme. It is experimentally shown that using commercially available narrow-band optical filters and transceivers; it is feasible to use passive filtering to increase the spectral efficiency.

Further, it is shown that for a given data rate and filter shape, an optimum filter offset point from the carrier exists, which should be used to obtain the USB and LSB signals. Finally, in Section 6.1.9, a diversity gain of 2.3dB is achieved for the two-fold diversity in which each of the transmitted signal's unwanted sideband is suppressed using optical filters. Furthermore, the free-space channel is simulated by considering the power vector with log-normal scintillation statistics and phase piston, which becomes crucial when the carrier separation is reduced to increase the diversity system's spectral efficiency.

To conclude, it is shown in this thesis by theoretical, numerical, and experimental means that transmitter diversity is a viable fading mitigation technique in an uplink channel. Further, passive filtering can remove the unwanted redundant sideband without affecting the signal quality, reducing the required bandwidth to transmit the signal. To do this, an optimum frequency offset between the filter center and the signal carrier has to be set. This optimum setting point depends on the data rate of the signal and the filter shape. Finally, the carrier separation between the two neighboring signals can be reduced to increase the spectral efficiency of the transmission system.

7.2. Future work

Some of the topics that may be further investigated to enhance the capability of the spectral efficient transmitter diversity scheme are listed below:

1. A more detailed investigation of the transmitter diversity scheme, including more than two transmitters, should be carried out in the simulations and measurements.
2. In this thesis, the lab measurements did not include the scintillation and phase piston. These atmospheric turbulence effects should be emulated in future work. Their impact on the communication performance should be evaluated, especially when the neighboring single sidebands have narrow frequency spacing to increase spectral efficiency.
3. The validity of the transmitter diversity scheme should be evaluated in the outdoor free-space tests. Such tests may include a ground-to-hilltop link representing the worst-case scenario of a GEO uplink or an actual ground-to-satellite link.

A. Appendix

1. A. Mustafa, D. Giggenbach, J. Poliak, A. Shrestha, R. Mata-Calvo, and C. Fuchs, "Lab implementation of 10 Gb/s per channel optical transmitter diversity scheme for geostationary satellite feeder links," in Photonic Networks; 16. ITG Symposium, 2015, pp. 1–3
2. A. Mustafa, D. Giggenbach, J. Poliak, and S. ten Brink, "Spectrally efficient transmitter diversity scheme for optical satellite feeder links employing multiple signal sidebands," in Photonic Networks; 18. ITG-Symposium, 2017, pp. 1–4
3. A. Mustafa, D. Giggenbach, J. Poliak, and S. ten Brink, "Quantifying the effect of atmospherically-induced pointing errors in optical geostationary satellite feeder links using transmitter diversity," in 2017 IEEE International Conference on Space Optical Systems and Applications (ICSOS), 2017, pp. 272–277
4. A. Mustafa, D. Giggenbach, J. Poliak, and S. ten Brink, "Laboratory demonstration of optimizing optical single sideband scheme to increase spectral efficiency in optical geostationary satellite feeder links," in Environmental Effects on Light Propagation and Adaptive Systems, K. U. Stein and S. Gladysz, Eds., vol. 10787, International Society for Optics and Photonics. SPIE, 2018, pp. 114 – 121
5. A. Mustafa, D. Giggenbach, J. Poliak, and S. ten Brink, "Quantifying the effect of the optimization of an M-fold transmitter diversity scheme with atmospherically induced beam wander and scintillation," in Photonic Networks; 20th ITG-Symposium, 2019, pp. 1–3
6. A. Shrestha, D. Giggenbach, A. Mustafa, J. Pacheco-Labrador, J. Ramirez, and F. Rein, "Fading testbed for free-space optical communications," in Advanced Free-Space Optical Communication Techniques and Applications II, L. Laycock and H. J. White, Eds., vol. 9991, International Society for Optics and Photonics. SPIE, 2016, pp. 16 – 25
7. R. Mata Calvo, D. Giggenbach, C. Fuchs, A. Mustafa, "Transmitter for an optical free-beam communication system", United States Patent Application 20180337729, Online: https://www.freepatentsonline.com/y2018/0337729.html

Bibliography

[1] E. Lutz, "Achieving a terabit/s geo satellite system," in *ka and Broadband communications, navigation and earth observations conference*, A. IEEE, Ed., Oktober 2013. [Online]. Available: https://elib.dlr.de/85339/ (p. xvi), (p. 1), (p. 2), (p. 3)

[2] A. Berk, P. Conforti, R. Kennett, T. Perkins, F. Hawes, and J. van den Bosch, "MODTRAN6: a major upgrade of the MODTRAN radiative transfer code," in *Algorithms and Technologies for Multispectral, Hyperspectral, and Ultraspectral Imagery XX*, M. Velez-Reyes and F. A. Kruse, Eds., vol. 9088, International Society for Optics and Photonics. SPIE, 2014, pp. 113 – 119. [Online]. Available: https://doi.org/10.1117/12.2050433 (p. xvi), (p. 8)

[3] L. Andrews and R. Phillips, *Laser Beam Propagation through Random Media*, 2nd ed. SPIE Press, 2005. (p. xvi), (p. xvii), (p. 1), (p. 5), (p. 10), (p. 11), (p. 19), (p. 23), (p. 25), (p. 27), (p. 49), (p. 59), (p. 82)

[4] R. M. Calvo, P. Becker, D. Giggenbach, F. Moll, M. Schwarzer, M. Hinz, and Z. Sodnik, "Transmitter diversity verification on ARTEMIS geostationary satellite," in *Free-Space Laser Communication and Atmospheric Propagation XXVI*, H. Hemmati and D. M. Boroson, Eds., vol. 8971, International Society for Optics and Photonics. SPIE, 2014, pp. 24 – 37. [Online]. Available: https://doi.org/10.1117/12.2036554 (p. xvi), (p. xvii), (p. 20), (p. 21), (p. 25), (p. 28), (p. 46)

[5] G. Agrawal, *Fiber-Optic Communication Systems*, ser. Wiley Series in Microwave and Optical Engineering. Wiley, 2012. [Online]. Available: https://books.google.de/books?id=yGQ4n1-r2eQC (p. xvii), (p. 33), (p. 34)

[6] M. Oerder and H. Meyr, "Digital filter and square timing recovery," *IEEE Transactions on Communications*, vol. 36, no. 5, pp. 605–612, 1988. (p. xvii), (p. 41)

[7] R. Stephens, *Equalization: The Correction and Analysis of DegradedSignals*, 1st ed., Aug. 2005. (p. xvii), (p. 42)

[8] I. B. Djordjevic, *Advanced Optical and Wireless Communications Systems*. Springer International Publishing AG, 2018. (p. xviii), (p. 75), (p. 76)

[9] M. A. Khalighi and M. Uysal, "Survey on free space optical communication: A communication theory perspective," *IEEE Communications Surveys Tutorials*, vol. 16, no. 4, pp. 2231–2258, Fourthquarter 2014. (p. 1)

[10] Z. Sodnik, B. Furch, and H. Lutz, "Free-space laser communication activities in europe: Silex and beyond," in *LEOS 2006 - 19th Annual Meeting of the IEEE Lasers and Electro-Optics Society*, 2006, pp. 78–79. (p. 1), (p. 9)

[11] B. V. Oaida, M. J. Abrahamson, R. J. Witoff, J. N. Bowles Martinez, and D. A. Zayas, "Opals: An optical communications technology demonstration from the international space station," in *2013 IEEE Aerospace Conference*, 2013, pp. 1–20. (p. 1)

[12] D. M. Boroson, "Free-space optical communications comes of age," Photonics Spectra, 2017. [Online]. Available: photonics.com/Articles/Free-Space_Optical_Communications_Comes_of_Age/a61909 (p. 1)

[13] H. Henniger and O. Wilfert, "An introduction to free-space optical communications," vol. 19, pp. 203–212, 06 2010. (p. 1)

[14] D. R. Kolev and M. Toyoshima, "Transmission analysis for ofdm signals over hybrid rf-optical high-throughput satellite," *Opt. Express*, no. 26, 2018. (p. 1)

[15] J. Poliak, R. M. Calvo, and F. Rein, "Demonstration of 1.72 tbit/s optical data transmission under worst-case turbulence conditions for ground-to-geostationary satellite communications," *IEEE Communications Letters*, pp. 1–1, 2018. (p. 1)

[16] R. Saathof, R. den Breeje, W. Klop, S. Kuiper, N. Doelman, F. Pettazzi, A. Vosteen, N. Truyens, W. Crowcombe, J. Human, I. Ferrario, R. M. Calvo, J. Poliak, R. Barrios, D. Giggenbach, C. Fuchs, and S. Scalise, "Optical technologies for terabit/s-throughput feeder link," in *2017 IEEE International Conference on Space Optical Systems and Applications (ICSOS)*, 2017, pp. 123–129. (p. 1)

[17] D. Giggenbach, E. Lutz, J. Poliak, R. Mata-Calvo, and C. Fuchs, "A high-throughput satellite system for serving whole europe with fast internet service, employing optical feeder links," in *Broadband Coverage in Germany. 9th ITG Symposium. Proceedings*, April 2015, pp. 1–7. (p. 1)

[18] S. Dimitrov, B. Matuz, G. Liva, R. Barrios, R. Mata-Calvo, and D. Giggenbach, "Digital modulation and coding for satellite optical feeder links," in *2014 7th Advanced Satellite Multimedia Systems Conference and the 13th Signal Processing for Space Communications Workshop (ASMS/SPSC)*, 2014, pp. 150–157. (p. 1)

[19] J. Poliak, R. M. Calvo, and F. Rein, "Demonstration of 1.72 tbit/s optical data transmission under worst-case turbulence conditions for ground-to-geostationary satellite communications," *IEEE Communications Letters*, vol. 22, no. 9, pp. 1818–1821, 2018. (p. 1)

[20] A. Dochhan, J. Poliak, J. Surof, M. Richerzhagen, H. F. Kelemu, and R. M. Calvo, "13.16 tbit/s free-space optical transmission over 10.45 km for geostationary satellite feeder-links," in *Photonic Networks; 20th ITG-Symposium*, 2019, pp. 1–3. (p. 1)

[21] B. Roy, S. Poulenard, S. Dimitrov, R. Barrios, D. Giggenbach, A. Le Kernec, and M. Sotom, "Optical feeder links for high throughput satellites," in *2015 IEEE International Conference on Space Optical Systems and Applications (ICSOS)*, 2015, pp. 1–6. (p. 1)

[22] D. Giggenbach, E. Lutz, J. Poliak, R. Mata-Calvo, and C. Fuchs, "A high-throughput satellite system for serving whole europe with fast internet service, employing optical feeder links," in *Broadband Coverage in Germany. 9th ITG Symposium. Proceedings*, 2015, pp. 1–7. (p. 1)

[23] M. Ijaz, Z. Ghassemlooy, J. Pesek, O. Fiser, H. Le Minh, and E. Bentley, "Modeling

of fog and smoke attenuation in free space optical communications link under controlled laboratory conditions," *Journal of Lightwave Technology*, vol. 31, no. 11, pp. 1720–1726, 2013. (p. 2)

[24] C. Fuchs and F. Moll, "Ground station network optimization for space-to-ground optical communication links," *J. Opt. Commun. Netw.*, vol. 7, no. 12, pp. 1148–1159, Dec 2015. [Online]. Available: http://jocn.osa.org/abstract.cfm?URI=jocn-7-12-1148 (p. 2)

[25] D. Giggenbach, "Optical satellite feeder links for terabps throughput," https://elib.dlr.de/83618/, 2013. [Online]. Available: https://elib.dlr.de/83618/ (p. 2)

[26] N. Perlot, T. Dreischer, C. M. Weinert, and J. Perdigues, "Optical geo feeder link design," in *2012 Future Network Mobile Summit (FutureNetw)*, 2012, pp. 1–8. (p. 2)

[27] S. Poulenard, M. Ruellan, B. Roy, J. Riédi, F. Parol, and A. Rissons, "High altitude clouds impacts on the design of optical feeder link and optical ground station network for future broadband satellite services," in *Free-Space Laser Communication and Atmospheric Propagation XXVI*, H. Hemmati and D. M. Boroson, Eds., vol. 8971, International Society for Optics and Photonics. SPIE, 2014, pp. 58 – 67. [Online]. Available: https://doi.org/10.1117/12.2038486 (p. 2)

[28] S. Poulenard, M. Crosnier, and A. Rissons, "Ground segment design for broadband geostationary satellite with optical feeder link," *IEEE/OSA Journal of Optical Communications and Networking*, vol. 7, no. 4, pp. 325–336, 2015. (p. 2)

[29] A. C. Casado and R. M. Calvo, *Springer Handbook of Optical Networks*, B. Mukherjee, I. Tomkos, M. Tornatore, P. Winzer, and Y. Zhao, Eds. Springer International Publishing, Sep. 2020. (p. 2)

[30] H. K. J. Kar, *Free Space Optical Communication*. Springer, 2017. (p. 5)

[31] D. L. Fried, "Statistics of laser beam fade induced by pointing jitter," *Appl. Opt.*, vol. 12, no. 2, pp. 422–423, Feb 1973. [Online]. Available: http://ao.osa.org/abstract.cfm?URI=ao-12-2-422 (p. 5), (p. 50)

[32] Xiaoming Zhu and J. M. Kahn, "Free-space optical communication through atmospheric turbulence channels," *IEEE Transactions on Communications*, vol. 50, no. 8, pp. 1293–1300, 2002. (p. 5)

[33] C. C. Davis and I. I. Smolyaninov, "Effect of atmospheric turbulence on bit-error rate in an on-off-keyed optical wireless system," in *Free-Space Laser Communication and Laser Imaging*, D. G. Voelz and J. C. Ricklin, Eds., vol. 4489, International Society for Optics and Photonics. SPIE, 2002, pp. 126 – 137. [Online]. Available: https://doi.org/10.1117/12.453236 (p. 5)

[34] D. Giggenbach and R. Mata-Calvo, "Sensitivity modeling of binary optical receivers," *Appl. Opt.*, vol. 54, no. 28, pp. 8254–8259, Oct 2015. [Online]. Available: http://ao.osa.org/abstract.cfm?URI=ao-54-28-8254 (p. 5), (p. 34), (p. 49), (p. 61)

[35] C. Pulikkaseril, L. A. Stewart, M. A. F. Roelens, G. W. Baxter, S. Poole, and S. Frisken, "Spectral modeling of channel band shapes in wavelength selective switches," *Opt. Express*, vol. 19, no. 9, pp. 8458–8470, Apr 2011. [Online]. Available:

http://www.opticsexpress.org/abstract.cfm?URI=oe-19-9-8458 (p. 5), (p. 65)

[36] J.-M. Conan, G. Rousset, and P.-Y. Madec, "Wave-front temporal spectra in high-resolution imaging through turbulence," *J. Opt. Soc. Am. A*, vol. 12, no. 7, pp. 1559–1570, Jul 1995. [Online]. Available: http://josaa.osa.org/abstract.cfm?URI=josaa-12-7-1559 (p. 5), (p. 28)

[37] J. Horwath, F. David, M. Knapek, and N. Perlot, "Coherent transmission feasibility analysis," in *Free-Space Laser Communication Technologies XVII*, G. S. Mecherle, Ed., vol. 5712, International Society for Optics and Photonics. SPIE, 2005, pp. 13 – 23. [Online]. Available: https://doi.org/10.1117/12.589196 (p. 5), (p. 28)

[38] A. L. Buck, "Effects of the atmosphere on laser beam propagation," *Appl. Opt.*, vol. 6, no. 4, pp. 703–708, Apr 1967. [Online]. Available: http://ao.osa.org/abstract.cfm?URI=ao-6-4-703 (p. 7)

[39] Z. Ghassemlooy, W. Popoola, and S. Rajbhandari, *Optical Wireless Communications: System and Channel Modelling with MATLAB®*. Taylor & Francis, 2012. [Online]. Available: https://books.google.de/books?id=jpXGCN1qVQ4C (p. 7)

[40] H. Henniger, D. Giggenbach, J. Horwath, and C. Rapp, "Evaluation of optical up- and downlinks from high altitude platforms using IM/DD," in *Free-Space Laser Communication Technologies XVII*, G. S. Mecherle, Ed., vol. 5712, International Society for Optics and Photonics. SPIE, 2005, pp. 24 – 36. [Online]. Available: https://doi.org/10.1117/12.600803 (p. 8)

[41] I. I. Kim, B. McArthur, and E. J. Korevaar, "Comparison of laser beam propagation at 785 nm and 1550 nm in fog and haze for optical wireless communications," in *Optical Wireless Communications III*, E. J. Korevaar, Ed., vol. 4214, International Society for Optics and Photonics. SPIE, 2001, pp. 26 – 37. [Online]. Available: https://doi.org/10.1117/12.417512 (p. 9)

[42] M. Toyoshima, K. Takizawa, T. Kuri, W. Klaus, M. Toyoda, H. Kunimori, T. Jono, Y. Takayama, N. Kura, K. Ohinata, K. Arai, and K. Shiratama, "Ground-to-OICETS laser communication experiments," in *Free-Space Laser Communications VI*, A. K. Majumdar and C. C. Davis, Eds., vol. 6304, International Society for Optics and Photonics. SPIE, 2006, pp. 79 – 86. [Online]. Available: https://doi.org/10.1117/12.693012 (p. 9)

[43] H. Zech, F. Heine, D. Troendle, P. M. Pimentel, K. Panzlaff, M. Motzigemba, R. Meyer, and S. Philipp-May, "LCTS on ALPHASAT and Sentinel 1a: in orbit status of the LEO to geo data relay system," in *International Conference on Space Optics — ICSO 2014*, Z. Sodnik, B. Cugny, and N. Karafolas, Eds., vol. 10563, International Society for Optics and Photonics. SPIE, 2017, pp. 249 – 254. [Online]. Available: https://doi.org/10.1117/12.2304149 (p. 9)

[44] F. Heine, P. M. Pimentel, C. Rochow, K. Saucke, D. Tröndle, M. Lutzer, R. Meyer, H. Bischl, and B. Matuz, "The European data relay system and Alphasat to T-AOGS space to ground links, status, and achievements in 2017," in *Free-Space Laser Communication and Atmospheric Propagation XXX*, H. Hemmati and D. M. Boroson,

Eds., vol. 10524, International Society for Optics and Photonics. SPIE, 2018, pp. 236 – 241. [Online]. Available: https://doi.org/10.1117/12.2290791 (p. 9)

[45] H. Hauschildt, S. Mezzasoma, H. L. Moeller, M. Witting, and J. Herrmann, "European data relay system goes global," in *2017 IEEE International Conference on Space Optical Systems and Applications (ICSOS)*, 2017, pp. 15–18. (p. 10)

[46] A. N. Kolmogorov, "A refinement of previous hypotheses concerning the local structure of turbulence in a viscous incompressible fluid at high reynolds number," *Journal of Fluid Mechanics*, vol. 13, no. 1, p. 82–85, 1962. (p. 11)

[47] J. Hardy, *Adaptive Optics for Astronomical Telescopes*, ser. Oxford series in optical and imaging sciences. Oxford University Press, 1998. (p. 12)

[48] R. Barrios, "Fading loss for Earth-to-space lasercom affected by scintillation and beam wander composite channel," *Optical Engineering*, vol. 59, no. 5, pp. 1 – 10, 2020. [Online]. Available: https://doi.org/10.1117/1.OE.59.5.056103 (p. 13), (p. 18)

[49] D. Giggenbach, "Optimierung der optischen freiraumkommunikation durch die turbulente atmosphäre - focal array receiver," 2005. (p. 14)

[50] A. Comeron, F. Dios, A. Rodriguez, J. A. Rubio, M. Reyes, and A. Alonso, "Modeling of power fluctuations induced by refractive turbulence in a multiple-beam ground-to-satellite optical uplink," in *Free-Space Laser Communications V*, D. G. Voelz and J. C. Ricklin, Eds., vol. 5892, International Society for Optics and Photonics. SPIE, 2005, pp. 196 – 205. [Online]. Available: https://doi.org/10.1117/12.617219 (p. 15)

[51] L. Andrews, "An analytical model for the refractive index power spectrum and its application to optical scintillations in the atmosphere," *Journal of Modern Optics*, vol. 39, no. 9, pp. 1849–1853, 1992. [Online]. Available: https://doi.org/10.1080/09500349214551931 (p. 17)

[52] D. Giggenbach and H. Henniger, "Fading-loss assessment in atmospheric free-space optical communication links with on-off keying," *Optical Engineering*, vol. 47, no. 4, pp. 1 – 6, 2008. [Online]. Available: https://doi.org/10.1117/1.2903095 (p. 20)

[53] F. Heine, P. Martin-Pimentel, H. Kaempfner, G. Muehlnikel, D. Troendle, H. Zech, C. Rochow, D. Dallmann, M. Reinhardt, M. Gregory, M. Lutzer, S. Philipp-May, R. Meyer, E. Benzi, P. Sivac, M. Krassenburg, I. Shurmer, and U. Sterr, "Alphasat and sentinel 1a, the first 100 links," in *2015 IEEE International Conference on Space Optical Systems and Applications (ICSOS)*, 2015, pp. 1–4. (p. 22)

[54] R. L. Fante, "Electromagnetic beam propagation in turbulent media," *Proceedings of the IEEE*, vol. 63, no. 12, pp. 1669–1692, 1975. (p. 23)

[55] V. W. S. Chan, "Free-space optical communications," *J. Lightwave Technol.*, vol. 24, no. 12, pp. 4750–4762, Dec 2006. (p. 25)

[56] I. I. Kim, H. Hakakha, P. Adhikari, E. J. Korevaar, and A. K. Majumdar, "Scintillation reduction using multiple transmitters," in *Free-Space Laser Communication Technologies IX*, G. S. Mecherle, Ed., vol. 2990, International Society for Optics and Photonics.

SPIE, 1997, pp. 102 – 113. [Online]. Available: https://doi.org/10.1117/12.273685 (p. 29)

[57] S. M. Navidpour, M. Uysal, and M. Kavehrad, "Ber performance of free-space optical transmission with spatial diversity," *IEEE Transactions on Wireless Communications*, vol. 6, no. 8, pp. 2813–2819, 2007. (p. 29)

[58] A. A. Farid and S. Hranilovic, "Diversity gain and outage probability for mimo free-space optical links with misalignment," *IEEE Transactions on Communications*, vol. 60, no. 2, pp. 479–487, 2012. (p. 29)

[59] A. Alonso, M. Reyes, and Z. Sodnik, "Performance of satellite-to-ground communications link between ARTEMIS and the Optical Ground Station," in *Optics in Atmospheric Propagation and Adaptive Systems VII*, J. D. Gonglewski and K. Stein, Eds., vol. 5572, International Society for Optics and Photonics. SPIE, 2004, pp. 372 – 383. [Online]. Available: https://doi.org/10.1117/12.565516 (p. 30)

[60] M. Toyoshima, T. Takahashi, K. Suzuki, S. Kimura, K. Takizawa, T. Kuri, W. Klaus, M. Toyoda, H. Kunimori, T. Jono, Y. Takayama, and K. Arai, "Laser beam propagation in ground-to-OICETS laser communication experiments," in *Atmospheric Propagation IV*, C. Y. Young and G. C. Gilbreath, Eds., vol. 6551, International Society for Optics and Photonics. SPIE, 2007, pp. 104 – 115. [Online]. Available: https://doi.org/10.1117/12.723116 (p. 30)

[61] A. Mustafa, D. Giggenbach, J. Poliak, A. Shrestha, R. Mata-Calvo, and C. Fuchs, "Lab implementation of 10 gbps/channel optical transmitter diversity scheme for geostationary satellite feeder links," in *Photonic Networks; 16. ITG Symposium*, 2015, pp. 1–3. (p. 31)

[62] A. Shrestha, D. Giggenbach, A. Mustafa, J. Pacheco-Labrador, J. Ramirez, and F. Rein, "Fading testbed for free-space optical communications," in *Advanced Free-Space Optical Communication Techniques and Applications II*, L. Laycock and H. J. White, Eds., vol. 9991, International Society for Optics and Photonics. SPIE, 2016, pp. 16 – 25. [Online]. Available: https://doi.org/10.1117/12.2239111 (p. 31), (p. 46)

[63] M. Abramowitz and I. Stegun, *Handbook of Mathematical Functions: With Formulas, Graphs, and Mathematical Tables*, ser. Applied mathematics series. Dover Publications, 1965. (p. 35)

[64] C. E. Shannon, "Communication in the presence of noise," *Proceedings of the IEEE*, vol. 72, no. 9, pp. 1192–1201, 1984. (p. 37)

[65] R. J. Essiambre, G. Kramer, P. J. Winzer, G. J. Foschini, and B. Goebel, "Capacity limits of optical fiber networks," *Journal of Lightwave Technology*, vol. 28, no. 4, pp. 662–701, 2010. (p. 37)

[66] B. S. Robinson, "Semiconductor-based all-optical switching for optical time-division multiplexed networks," Ph.D. dissertation, Massachusetts Institute of Technology. Dept. of Electrical Engineering and Computer Science, 2003. (p. 37)

[67] P. Massoud Salehi and J. Proakis, *Digital Communications*. McGraw-Hill Education, 2007. [Online]. Available: https://books.google.de/books?id=HroiQAAACAAJ (p. 37)

[68] H. A. Haus, "The noise figure of optical amplifiers," *IEEE Photonics Technology Letters*, vol. 10, no. 11, pp. 1602–1604, 1998. (p. 37)

[69] S. B. Alexander, *Optical Communication Receiver Design*. IET, 1997. (p. 38)

[70] Seung Joon Lee, "A new non-data-aided feedforward symbol timing estimator using two samples per symbol," *IEEE Communications Letters*, vol. 6, no. 5, pp. 205–207, 2002. (p. 41)

[71] *Spectral grids for WDM applications: DWDM frequency grid. .ITU-T Recommendation G.694.1*, International Telecommunications Union Std., 2020. (p. 44)

[72] Kyosemi, "Ingaas 10g apd-tia receiver - kpdxa10g-h34s - datasheet," 2022. (p. 46)

[73] P. J. Titterton, "Power reduction and fluctuations caused by narrow laser beam motion in the far field," *Appl. Opt.*, vol. 12, no. 2, pp. 423–425, Feb 1973. (p. 50)

[74] M. Toyoshima and K. Araki, "Effects of time averaging on optical scintillation in a ground-to-satellite atmospheric propagation," *Appl. Opt.*, vol. 39, no. 12, pp. 1911–1919, Apr 2000. [Online]. Available: http://ao.osa.org/abstract.cfm?URI=ao-39-12-1911 (p. 50), (p. 51), (p. 59), (p. 60)

[75] K. Kiesaleh and T. Y. Yan, "A statistical model for evaluating GOPEX uplink performance," in *The Telecommunications and Data Acquisition Report*, Nov. 1992, pp. 325–332. (p. 50)

[76] B. E. A. S. M. C. Teich, *Fundamentals of Photonics*, 1991. (p. 50)

[77] M. Toyoshima, T. Jono, K. Nakagawa, and A. Yamamoto, "Optimum intersatellite link design in the presence of random pointing jitter for free-space laser communication systems," in *Free-Space Laser Communication Technologies XIV*, G. S. Mecherle, Ed., vol. 4635, International Society for Optics and Photonics. SPIE, 2002, pp. 95 – 102. [Online]. Available: https://doi.org/10.1117/12.464097 (p. 51)

[78] K. Kiasaleh, "On the probability density function of signal intensity in free-space optical communications systems impaired by pointing jitter and turbulence," *Optical Engineering*, vol. 33, no. 11, pp. 3748 – 3757, 1994. (p. 51)

[79] A. Mustafa, D. Giggenbach, J. Poliak, and S. ten Brink, "Quantifying the effect of atmospherically-induced pointing errors in optical geostationary satellite feeder links using transmitter diversity," in *2017 IEEE International Conference on Space Optical Systems and Applications (ICSOS)*, 2017, pp. 272–277. (p. 52)

[80] T. Tolker-Nielsen and G. Oppenhauser, "In-orbit test result of an operational optical intersatellite link between ARTEMIS and SPOT4, SILEX," in *Free-Space Laser Communication Technologies XIV*, G. S. Mecherle, Ed., vol. 4635, International Society for Optics and Photonics. SPIE, 2002, pp. 1 – 15. [Online]. Available: https://doi.org/10.1117/12.464105 (p. 53)

[81] W. ming Wu, Y. Ning, P. fei Zhang, X. xing Feng, and C. hong Qiao, "Scintillation analysis for multiple uplink Gaussian beams in the presence of beam wander," in *Selected Papers from Conferences of the Photoelectronic Technology Committee of the Chinese*

Society of Astronautics: Optical Imaging, Remote Sensing, and Laser-Matter Interaction 2013, J. Ojeda-Castaneda, S. Han, P. Jia, J. Fang, D. Fan, L. Qian, Y. Gu, and X. Yan, Eds., vol. 9142, International Society for Optics and Photonics. SPIE, 2014, pp. 580 – 585. (p. 53), (p. 54)

[82] M. Toyoshima, S. Yamakawa, T. Yamawaki, K. Arai, M. R. Garcia-Talavera, A. Alonso, Z. Sodnik, and B. Demelenne, "Long-term statistics of laser beam propagation in an optical ground-to-geostationary satellite communications link," *IEEE Transactions on Antennas and Propagation*, vol. 53, no. 2, pp. 842–850, Feb 2005. (p. 53), (p. 60)

[83] A. Mustafa, D. Giggenbach, J. Poliak, and S. ten Brink, "Quantifying the effect of the optimization of an m-fold transmitter diversity scheme with atmospherically induced beam wander and scintillation," in *Photonic Networks; 20th ITG-Symposium*, 2019, pp. 1–3. (p. 60)

[84] A. Mustafa, D. Giggenbach, J. Poliak, and S. ten Brink, "Laboratory demonstration of optimizing optical single sideband scheme to increase spectral efficiency in optical geostationary satellite feeder links," in *Environmental Effects on Light Propagation and Adaptive Systems*, K. U. Stein and S. Gladysz, Eds., vol. 10787, International Society for Optics and Photonics. SPIE, 2018, pp. 114 – 121. [Online]. Available: https://doi.org/10.1117/12.2325737 (p. 64)

[85] A. Mustafa, D. Giggenbach, J. Poliak, and S. ten Brink, "Spectrally efficient transmitter diversity scheme for optical satellite feeder links employing multiple signal sidebands," in *Photonic Networks; 18. ITG-Symposium*, 2017, pp. 1–4. (p. 74)

[86] X. Wei and J. Leuthold, "Relation between vestigial-sideband filtering and $\pi/2$ progressive phase shift," *Opt. Lett.*, vol. 29, no. 14, pp. 1599–1601, Jul 2004. (p. 78)

[87] S. Bigo, "Multiterabit/s dwdm terrestrial transmission with bandwidth-limiting optical filtering," *IEEE Journal of Selected Topics in Quantum Electronics*, vol. 10, no. 2, pp. 329–340, 2004. (p. 78)

[88] B. J. Klein and J. J. Degnan, "Optical antenna gain. 1: Transmitting antennas," *Appl. Opt.*, vol. 13, no. 9, pp. 2134–2141, Sep 1974. (p. 81)

[89] J. J. Degnan and B. J. Klein, "Optical antenna gain. 2: Receiving antennas," *Appl. Opt.*, vol. 13, no. 10, pp. 2397–2401, Oct 1974. (p. 81)

[90] S. Arnon, N. Kopeika, D. Kedar, A. Zilberman, D. Arbel, A. Livne, M. Guelman, M. Orenstain, H. Michalik, and A. Ginati, "Performance limitation of laser satellite communication due to vibrations and atmospheric turbulence: down-link scenario," *Int. J. Satell. Commun. Netw.*, vol. 21, pp. 561–573, 2003. (p. 82)

[91] H. Hemmati, *Near-Earth Laser Communications, Second Edition*, ser. Optical Science and Engineering. CRC Press, 2020. (p. 82)

[92] M. Toyoshima, "Maximum fiber coupling efficiency and optimum beam size in the presence of random angular jitter for free-space laser systems and their applications," *J. Opt. Soc. Am. A*, vol. 23, no. 9, pp. 2246–2250, Sep 2006. (p. 82)